

AD-777 151

SEISMIC DISCRIMINATION

Michael A. Chinnery

Massachusetts Institute of Technology

Prepared for:

Electronic Systems Division  
Advanced Research Projects Agency

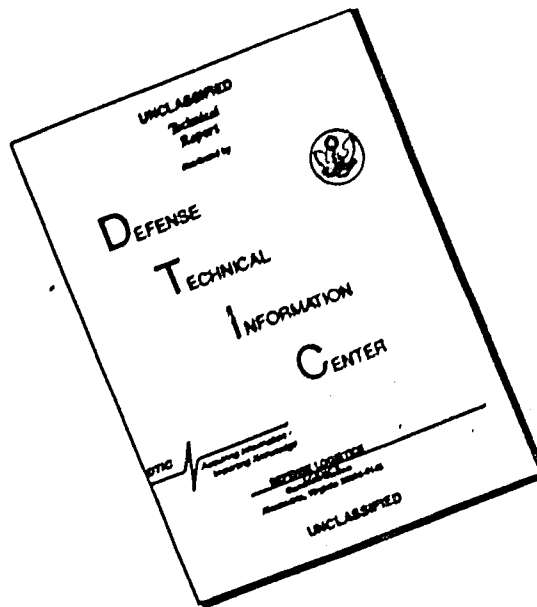
31 December 1973

DISTRIBUTED BY:

**NTIS**

National Technical Information Service  
U. S. DEPARTMENT OF COMMERCE  
5285 Port Royal Road, Springfield Va. 22151

# DISCLAIMER NOTICE



THIS DOCUMENT IS BEST QUALITY AVAILABLE. THE COPY FURNISHED TO DTIC CONTAINED A SIGNIFICANT NUMBER OF PAGES WHICH DO NOT REPRODUCE LEGIBLY.

AD-777151

DOCUMENT CONTROL DATA - R&D

(Security classification of title, body of abstract and indexing annotation must be entered when the overall report is classified)

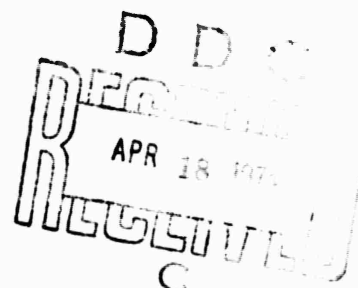
1. ORIGINATING ACTIVITY (Corporate author)  Lincoln Laboratory, M.I.T.		2a. REPORT SECURITY CLASSIFICATION Unclassified	
		2b. GROUP	
3. REPORT TITLE  Seismic Discrimination			
4. DESCRIPTIVE NOTES (Type of report and inclusive dates) Semiannual Technical Summary Report - 1 July through 31 December 1973			
5. AUTHOR(S) (Last name, first name, initial)  Chinnery, Michael A.			
6. REPORT DATE 31 December 1973		7a. TOTAL NO. OF PAGES	7b. NO. OF REFS 49
8a. CONTRACT OR GRANT NO. F19628-73-C-0002		9a. ORIGINATOR'S REPORT NUMBER(S) Semiannual Technical Summary, 31 December 1973	
b. PROJECT NO. ARPA Order 512		9b. OTHER REPORT NO(S) (Any other numbers that may be assigned this report) ESD-TR-73-348	
c.			
d.			
10. AVAILABILITY/LIMITATION NOTICES  Approved for public release; distribution unlimited.			
11. SUPPLEMENTARY NOTES  None		12. SPONSORING MILITARY ACTIVITY  Advanced Research Projects Agency, Department of Defense	
13. ABSTRACT  <p>The analysis of the data for the International Seismic Month is nearing completion. The effects of crust and upper-mantle structure on the short-period signals received at LASA and NORSAR are described. Further work on interfering Rayleigh waves and on the phase pP is included, together with several studies in global seismology. Our development of a seismic computer terminal system for the ARPA Network is progressing satisfactorily.</p> <p>Reproduced by NATIONAL TECHNICAL INFORMATION SERVICE U S Department of Commerce Springfield VA 22151</p>			
14. KEY WORDS  seismic discrimination seismic array  LASA NORSAR			

i

MASSACHUSETTS INSTITUTE OF TECHNOLOGY  
LINCOLN LABORATORY

SEISMIC DISCRIMINATION

SEMIANNUAL TECHNICAL SUMMARY REPORT  
TO THE  
ADVANCED RESEARCH PROJECTS AGENCY



1 JULY - 31 DECEMBER 1973

ISSUED 26 FEBRUARY 1974

Approved for public release; distribution unlimited.

LEXINGTON

MASSACHUSETTS

ia

The work reported in this document was performed at Lincoln Laboratory, a center for research operated by Massachusetts Institute of Technology. This research is a part of Project Vela Uniform, which is sponsored by the Advanced Research Projects Agency of the Department of Defense under Air Force Contract F19628-73-C-0002 (ARPA Order 512).

This report may be reproduced to satisfy needs of U.S. Government agencies.

Non-Lincoln Recipients

**PLEASE DO NOT RETURN**

Permission is given to destroy this document  
when it is no longer needed.

# ABSTRACT

The analysis of the data for the International Seismic Month is nearing completion. The effects of crust and upper-mantle structure on the short-period signals received at LASA and NORSAR are described. Further work on interfering Rayleigh waves and on the phase pP is included, together with several studies in global seismology. Our development of a seismic computer terminal system for the ARPA Network is progressing satisfactorily.

Accepted for the Air Force  
Eugene C. Raabe, Lt. Col., USAF  
Chief, ESD Lincoln Laboratory Project Office

## CONTENTS

Abstract	iii
Summary	v
Glossary	vi
 I. INTERNATIONAL SEISMIC MONTH	 1
A. ISM Event List Characteristics	1
B. Analysis of the ISM Long-Period Data	6
 II. ARRAY STUDIES	 15
A. NORSAR Epicenter Azimuth Errors	15
B. Analysis of Array Diagrams at LASA and NORSAR	15
C. A Random Medium Analysis of Crust and Upper-Mantle Structure Under NORSAR	18
D. Amplitude and Phase Variations of Signals Within NORSAR and LASA Subarrays	20
E. P-Wave Amplitude Patterns Across NORSAR	21
F. Effects of Crustal Structure Beneath NORSAR on Short-Period Teleseisms	23
G. Phase Velocity and Azimuth Deviations Across LASA and NORSAR for Local Events	24
H. Locating Ability of LASA and NORSAR	28
 III. SEISMIC DISCRIMINATION	 58
A. Detection of Interfering Rayleigh Waves at NORSAR	58
B. Precursors to pP from Deep South American Earthquakes	60
C. Comparison of pP-P Delay Times from Surface-Zero and Teleseismic Records of Nuclear Explosions	62
 IV. GENERAL SEISMOLOGY	 75
A. Digital Event Detector in Real Time	75
B. Travel-Time Anomalies for the Global Station Network	76
C. P and S Velocity Structure of the Lower Mantle	77
D. The Paleomagnetism and Tectonics of Asia	79
 V. COMPUTER FACILITIES	 91
A. ARPA Network Computer Facility Development	91
B. PDP-7 Computer System	92

## SUMMARY

This is the twentieth Semiannual Technical Summary report of M.I.T. Lincoln Laboratory's Seismic Discrimination Group. The research activities of this Group are directed toward the solution of the seismological problems associated with the detection, location and identification of earthquakes and nuclear explosions. We are particularly concerned with the analysis of global seismic information, utilizing modern interactive computer-processing techniques, in order to develop the technological background necessary for the negotiation of a comprehensive test-ban treaty.

A major effort of the Group has been to study the detection and location capability of the existing network of seismic stations and arrays. The period 20 February to 19 March 1972 was designated as the International Seismic Month and, with the excellent cooperation of seismologists in many countries, the available seismic data for this period have been analyzed in detail. The first phase of this project consisted of the preparation of an epicenter list based on the short-period arrivals at selected WWSSN stations, Canadian network stations, and a number of arrays including LASA and NORSAR. This phase is now completed, and the final epicenter list contains 996 entries. Special attention has been given to the precision of the estimates of epicentral location, focal depth and magnitude, and the events have been categorized by the reliability of these estimates. The second phase of the study concerns the association of long-period arrivals with the listed events, and the assignment of surface wave magnitudes. The problem of associating the long- and short-period data has raised a number of interesting questions that are important for seismic discrimination. This phase will be completed shortly. The final report on this study, including basic statistical analyses of the data, will be available in the spring of 1974.

We continue to have a strong interest in research concerning the performance of seismic arrays, and a number of studies of this kind are described. We have developed the comparison of NORSAR with LASA, and it is becoming apparent that much of the observed complexity of short-period arrivals at NORSAR may be attributed to crust and upper-mantle structure. Results are presented detailing the nature of this complexity for each subarray, in terms of spectral characteristics, and explaining how these influence the performance of the array as a whole, in terms of array diagrams. Some of these features are similar to those found at LASA.

Research in seismic discrimination has concentrated on two subjects - the interfering Rayleigh wave problem, and the further study of the depth phase pP. The presence of multipathing can complicate the process of the separation of Rayleigh waves from two events, but results are given that indicate some success using high-resolution frequency-wave number techniques. Complications in the structure of pP due to reflections at internal boundaries in the earth are described, and the identification of pP in explosion records is discussed.

In preparation for making use of the global seismic information to be available via the ARPA Network, we have been extending our research into global seismology, and are strengthening our facilities for the rapid access and processing of digital data. Improvements in world-wide seismic station corrections are proposed, and we continue our study of inhomogeneities in the earth. S-wave travel-time anomalies show evidence of these inhomogeneities even more clearly than P-waves. In addition, we describe a study that is the first step in a series of investigations attempting to relate earthquake source mechanisms to large-scale tectonics.

Our development of a sophisticated interactive computer facility for utilizing the capabilities of the ARPA Network is continuing. We shall have a permanent connection into the network in the very near future, and we expect to be ready to receive seismic information as it becomes available on the Network.

M. A. Chinnery



## GLOSSARY

ALPA	Alaskan Long-Period Array
ANTS	ARPA Network Terminal System
ARPA	Advanced Research Projects Agency
CRT	Cathode Ray Tube
GMT	Greenwich Mean Time
IMP	Information Message Processor
ISM	International Seismic Month
J-B	Jeffreys-Bullen (Tables)
LASA	Large Aperture Seismic Array
MOHO	Mohorovicic Discontinuity
NCP	Network Control Program
NORSAR	Norwegian Seismic Array
NOS	National Ocean Survey
PDE	Preliminary Determination of Epicenters
SATS	Semiannual Technical Summary
SDAC	Seismic Data Analysis Center
USCGS	United States Coast and Geodetic Survey
USGS	United States Geological Survey
VLPE	Very Long-Period Experiment
VM	Virtual Machine
WWSSN	World-Wide Standard Seismographic Network

## SEISMIC DISCRIMINATION

### I. INTERNATIONAL SEISMIC MONTH

#### A. ISM EVENT LIST CHARACTERISTICS

The International Seismic Month (ISM) is a multi-national cooperative experiment which has been discussed in previous SATS<sup>1</sup> and in a recent report<sup>2</sup>. Our final list of verified events for that experiment contains 996 entries, 169 of which have not been assigned body wave magnitudes. The most common reasons for this are:

- (1) The lack of reported amplitudes by certain stations.
- (2) The lack of recorded P arrivals at distances greater than 10°.

Obviously, the first of these also affects the quality of the  $m_b$  value even when we do have enough amplitudes to assign  $m_b$  to an event. With this in mind, we have taken steps to partially correct the situation. Our film library was searched to find film chips for stations which were used in the ISM but which previously had not been completely read specifically for the ISM. There were 20 such stations. A search of ISM data indicated that more than 800 P arrivals at these stations had been associated with events, but that no amplitude or period readings were in the data base. The film data have been reviewed and the missing amplitude and period data obtained. These data will shortly be integrated into the rest of the ISM information, and  $m_b$  values revised accordingly. This is expected to change some of the statistics which are discussed below.

An attempt has been made to grade events according to the reliability that we can assign to the event parameters. There are eight grades, namely, A, B, C, and D for events which could be located without restraining the depth in any way, and AI, BI, CI, and DI for cases when the data left the depth indeterminate and it was necessary to arbitrarily restrain depth. To avoid confusion, we should note that depth phases are used routinely by our location program, and that a hypocenter obtained using depth phases is considered unrestrained. An indeterminate depth indicates that the location program converged to a negative depth or a depth greater than 700 km, or that depth was so poorly constrained that convergence could not be obtained.

The event grades are based upon six different parameters. One of these, NAVEMB, is the number of individual station  $m_b$  values averaged to get the ISM  $m_b$  value, AVEMB. The other five, which relate to location, are:

DEGF	Degrees of freedom in the location. This is the number of observations used minus the number of parameters to be determined.
RATIO	Goodness of fit measure. Residuals are weighted inversely by their assigned standard deviations, summed, and divided by DEGF to obtain RATIO.
MAXAX2	Largest principal semiaxis of our estimated epicenter error ellipse. Calculated only for unrestrained locations. Units are kilometers.
DEPTHQ	1/2 length of our estimated depth error bar, in kilometers. Calculated only for unrestrained locations.
DEPTH	ISM assigned depth for the event, in kilometers.

The exact quantitative meaning of some of these items is not finalized, but we have tried to use them nevertheless. Some discussion of them, and our location program, will be found in our last SATS (30 June 1973).<sup>1</sup>

TABLE I-1 LINCOLN ISM GRADING RULES	
Run Free	Restrained
Grade = A (287) $MAXAX2 \leq 100$ $RATIO \leq 2$ $DEGF \geq 4$ $DEPTHQ/DEPTH \leq 0.5$ or $DEPTHQ \leq 25$ $NAVEMB \geq 3$	Grade = AI (61) $RATIO \leq 1$ $DEGF \geq 5$ $NAVEMB \geq 3$
Grade = B (56) $MAXAX2 \leq 100$ $RATIO \leq 2$ $DEGF \geq 4$ $DEPTHQ/DEPTH \leq 0.5$ or $DEPTHQ \leq 25$ $NAVEMB = 1$ or $2$	Grade = BI (19) $RATIO \leq 1$ $DEGF \geq 5$ $NAVEMB = 1$ or $2$
Grade = C (60) $MAXAX2 \leq 100$ $RATIO \leq 2$ $DEGF \geq 4$ $DEPTHQ/DEPTH > 0.5$ $DEPTHQ > 25$ $NAVEMB \geq 1$	Grade = CI (32) $RATIO > 1$ $RATIO \leq 2$ $DEGF \geq 5$ $NAVEMB \geq 1$
Grade = D (197) All run free which are not A, B, or C	Grade = DI (264) All restrained which are not A, B, or C

Table I-1 gives the definition of grades in terms of the above parameters. The number of events in each grade is given in parentheses. For a given grade, all conditions must be met.

The transition from Grade A to D is fairly clear in the case of unrestrained events; that is:

- A = Excellent hypocenter and  $m_b$
- B = Excellent hypocenter, but perhaps less reliable  $m_b$
- C = Excellent epicenter, but perhaps less reliable depth as well as  $m_b$
- D = All others.

The transition is more arbitrary and less clear for AI to DI. First note that  $DEGF \geq 5$  for AI, BI, and CI, whereas it is  $DEGF \geq 4$  for A, B, and C. In effect, this means that we must have at least eight observations used for location in all cases.

For AI and BI, we require  $RATIO \leq 1$  rather than  $RATIO \leq 2$  in the hope that tighter control on that parameter will compensate for not having  $DEPTHQ$  or  $MAXAX2$ . In case CI, we include events with  $1 < RATIO \leq 2$  in place of relaxing the depth control parameters which are not available. The transition in terms of  $NAVEMB$  is unchanged for restrained events. We should note that for many purposes events in grades AI, BI, and CI, and even many in DI, probably have good depths. That is, shallow depths are probably good within a few tens of kilometers and deep events do get listed as deep. Unfortunately, this is a subjective and unsubstantiated assertion. A final point to re-emphasize is that events were restrained in depth only when that was the only way convergence of the location program could be obtained.

Events in grades D and DI tend to be the lower-magnitude events. This is clear from Fig. I-1. However not all (D, DI) events have assigned magnitudes so small that they are of no interest for

discrimination. This creates a problem unless these events can be somehow upgraded or it can be established that the assigned magnitude is very much in error. Our reading of additional amplitudes should help this situation somewhat.

The overall geographical distribution of all ISM events is shown in Fig. I-2(a). Figure I-2(b) shows the distribution of events when (D, DI) events are excluded from the population. Table I-2 is a somewhat more detailed breakdown of geographical distribution by grade and seismic region (Flinn and Engdahl<sup>3</sup>). The fraction of events in the (D, DI) categories for a region gives a crude idea of how well that region was covered by ISM data and procedures. No more than 25 percent of the events from regions 18, 21, 24, 26, 27, 28, and 31 are D or DI. However more than 75 percent of events in regions 3, 11, 16, 35, 36, 37, 38, 39 and 43 are category D or DI, leading us to believe that these regions require improved station coverage or data-processing methods.

It is our belief that all events on the ISM list are real. However, when dealing with large numbers of observations, it is always possible for data to erroneously fit together to create bogus events. An experiment was conducted with the help of USGS to see how serious a problem this might be. A set of random arrival times was generated for a simulated period of ten days with approximately the same number of arrivals per day as was reported during the ISM. These data were processed by the USGS program which is normally used to associate arrivals and locate events for PDE. Of course, all the arrivals in this experiment were false whereas half or more of the arrivals in the actual ISM clearly associate with real events. Nevertheless, the program generated a surprising 99 bogus events. However, unlike the 996 ISM events, the 99 events were not subjected to careful analysis, review, and reworking. For example, 17 of the 99 events have a *RATIO* (defined above) larger than all but two of the actual ISM events. No array azimuth and velocity information was available for control. The distribution of the stations associated with an event was not considered by the program. Although it has not been possible to complete the analysis of these 99 pseudo-events without prejudice, it is our belief that no more than a few would have been accepted during routine ISM processing. Any accepted ones would certainly have been graded either D or DI. In summary, we conclude that no more than a small fraction of 1 percent of ISM events might be bogus.

Some comparisons have been made between ISM epicenters and epicenters from other sources. Events of grades D and DI were excluded for these comparisons. The other sources of epicenters were the USGS PDE list, the LASA daily bulletin, and the NORSAR daily bulletin. The distance in degrees from the ISM epicenter to each of these was calculated and the histograms in Fig. I-3(a-c) were generated. The histograms are constructed with boxes of unit width centered at 1°, 2°, ..., 20°. The number of ISM-PDE, ISM-LASA, ISM-NORSAR events used were 304, 362, and 285, respectively. There were 5 LASA and 2 NORSAR cases off the scale of the histograms. These and other large discrepancies are being checked for specific explanations and/or clerical errors. ISM and PDE epicenters are quite close to each other. However, ISM and LASA or NORSAR can differ by several degrees, with NORSAR showing more spread than LASA. This is to be expected since NORSAR has a smaller aperture and also gives bulletin reports based on PKP phases. The possibility that ISM epicenters are in error by several degrees must be briefly entertained, but the consistency of ISM and PDE epicenters seems to make that unlikely.

A subset of 32 of the almost 200 stations used in generating the ISM event list have been selected for additional study. These stations were selected to give good global coverage while using stations which contributed data to large numbers of ISM events. Table I-3 shows this list of stations and an indication of their contribution to the ISM in terms of total picks submitted, total

TABLE I-2  
DISTRIBUTION OF ISM EVENTS BY GRADE AND SEISMIC REGION

Region No.	Region Name	Number of Events by Grade									
		A	AI	B	BI	C	CI	D	DI	All	
1	Alaska-Aleutian Arc	24	2	1	4	6	1	17	14	69	
2	Eastern Alaska to Vancouver Island	1			1				1	3	
3	California-Nevada Region	1	1			2		2	14	20	
4	Baja California and Gulf of California	2	4	1	1	8	3	6	18	43	
5	Mexico-Guatemala Area	9	4			2	3	8		26	
6	Central America	4	2			3		7	5	21	
7	Caribbean Loop	10	1			1		1	6	19	
8	Andean South America	17	2	11	2	1	1	23	20	77	
9	Extreme South America	1					1		1	3	
10	Southern Antilles	1		1		1		2	3	8	
11	New Zealand Region			1				3		4	
12	Kermadec-Tonga-Samoa Area	14	2	2	3	2	3	10	18	54	
13	Fiji Islands Area	5	3	1			1	8	5	23	
14	New Hebrides Islands	13		3		2	1	8	9	36	
15	Bismarck and Solomon Islands	6	1	3	1	4	1	12	12	40	
16	New Guinea	4		1		1		11	8	25	
17	Caroline Islands to Guam										
18	Guam to Japan	57	5	8		8	4	12	13	107	
19	Japan-Kuriles-Kamchatka	43	5	9	2	16	2	25	32	154	
20	Southwestern Japan and Ryukyu Islands	3	1						4	8	
21	Taiwan	4	1	1		1	1		2	10	
22	Philippines	8	2			3	1	2	3	19	
23	Borneo-Celebes	1			1	1			3	6	
24	Sunda Arc	8	1	6		3	1	2	2	23	
25	Burma and Southeast Asia	2							1	3	
26	India-Tibet-Szechwan-Yunan		2			1			1	4	
27	Southern Sinkiang to Kansu					3				3	
28	Alma-Ata to Lake Baikal	2	2			1				5	
29	Western Asia	6	2			1	3	3	15	30	
30	Middle East-Crimea-Balkans	12	1	4	2	1	1	7	10	38	
31	Western Mediterranean Area	3	3		1				1	8	
32	Atlantic Ocean	3	1			2	1	7	3	17	
33	Indian Ocean	1	4		1	2	1	3	1	13	
34	Eastern North America	1	1			1	1		5	9	
35	Eastern South America								1	1	
36	Northwestern Europe							1	4	5	
37	Africa							3	6	9	
38	Australia								2	2	
39	Pacific Basin					1		2	2	5	
40	Arctic Zone	5	1				1	2	1	10	
41	Eastern Asia	5						2	3	10	
42	N. E. Asia, Northern Alaska to Greenland	1							1	2	
43	Southeastern and Antarctic Pacific		2	1				6	4	13	
44	Galapagos Area	1						1	1	3	
45	Macquarie Loop		1						1	2	
46	Andaman Islands to Sumatra	1				1			2	4	
47	Baluchistan	1							1	2	
48	Hindu Kush and Pamir	7	4	2		1		1	5	20	
49	Northern Asia										
50	Antarctica										

TABLE 1-3  
CONTRIBUTION OF 32 SELECTED STATIONS TO THE ISM EVENT LIST

Station	Location	Distinct Input Picks	Associated Picks	Associated Events	Phase Associated Picks			
					P	Ph.P	AP	Other
LAO	Montana	3881	1358	734	672	46	217	423
YKA	N. W. Territory Canada	634	509	500	480	16	8	5
UBO	Utah	1082	480	466	433	33	7	7
NAO	Norway	2297	582	426	350	66	39	127
HFS	Sweden	502	355	341	288	54	5	8
MBL	N. W. Territory Canada	442	332	331	308	20	1	3
KBL	Afghanistan	983	298	291	243	44	7	4
ASP	N. Territory Australia	535	281	281	272	8	1	0
MAT	Honshu, Japan	544	255	252	248	3	0	4
COL	Alaska	318	231	228	223	5	1	0
CHG	Thailand	892	256	222	202	18	24	4
PNS	Polivia	330	173	173	104	69	0	0
CTA	Queensland, Australia	304	172	171	164	7	0	1
BLC	N. W. Territory Canada	195	167	166	149	16	1	1
NUR	Finland	215	166	162	132	30	2	1
TUC	Arizona	177	152	150	146	4	1	1
FBC	N. W. Territory Canada	166	147	147	127	20	0	0
GBA	India	268	144	144	123	21	0	0
SPA	South Pole	192	141	141	114	27	0	0
PMG	New Guinea	236	125	125	125	0	0	0
KIC	Ivory Coast	227	114	112	68	44	1	0
CLL	E. Germany	237	109	107	77	30	0	0
SSF	France	123	103	100	57	43	1	2
BDF	Brazil	272	101	101	76	25	0	0
BNG	Central African Republic	209	99	99	51	48	0	0
QJE	Pakistan	141	99	99	87	11	0	0
SHI	Iran	185	79	78	73	5	0	1
BAG	Philippine Islands	84	69	68	67	1	0	1
BUL	S. Africa	118	68	66	34	32	0	0
AFI	Samoa	166	56	56	55	1	0	0
EZN	Turkey	144	55	55	44	8	0	3
SHL	India	114	52	52	48	4	0	0

used in some way, number of events to which the station contributed, and a breakdown of phase assignments. Of these stations, LAO, NAO, HFS, KBL, CHG, and all Canadian stations were carefully read by an analyst or in some other way treated especially for the ISM. For the other stations, only the picks routinely submitted by them to USGS for PDE were used for ISM. One purpose in selecting this smaller number of stations was to isolate a limited number of stations for more detailed study. The other was to configure a modest network and evaluate its performance relative to the overall ISM.

TABLE I-4 COMPARISON OF GRADE DISTRIBUTION OF ISM EVENTS WITH THAT OF SUBLIST GENERATED AND GRADED USING ONLY A SUBSET OF 32 STATIONS		
Grade	Number of ISM Events	Number of Regraded ISM32 Events
A	287	233
AI	61	67
B	56	0
BI	19	5
C	80	8
CI	32	8
D	197	239
DI	214	268

An attempt has been made to locate all ISM events using only the 32-station network. The result has been encouraging. It has been possible to locate 818 of the 996 events using just the 32 stations. Of the 178 which could not be located, 168 of them were in the (D, DI) category, 6 in the (C, CI) category, and 4 in the B category in the original ISM list. However, when the events located with 32 stations were graded there was a modest downgrading of event quality. The number of events in each grade for the ISM and the 32-station network is shown in Table I-4. The capability of smaller networks will continue to be investigated.

R. T. Lacoss  
R. E. Needham  
R. M. Sheppard

#### B. ANALYSIS OF THE ISM LONG-PERIOD DATA

The second half of the ISM experiment concerns the detection and association of surface waves recorded during the month and the assignment of surface wave magnitudes to the events located using short-period data. This will allow the evaluation of the existing long-period arrays and networks over an extended period of time using a comprehensive epicenter list and help focus the problems that a world-wide, operational, discrimination effort might encounter. The analysis of the long-period data is not yet complete and what follows is a brief, interim report.

## 1. The Data

The long-period data for the ISM study came from three major sources and, for the most part, are based on readings of seismograms from stations of various networks. The source and type of data are:

Department of Energy, Mines, and Resources, Ottawa, Canada. Amplitudes, periods, and associations of Rayleigh waves recorded at selected stations of the World-Wide Standard Seismographic Network (WWSSN) and Canadian networks and the Hagfors array, Sweden.

Lamont-Doherty Geological Observatory. Amplitudes, periods, and approximate arrival times of Rayleigh and Love waves recorded at stations of the Very Long-Period Experiment (VLPE) network.

Lincoln Laboratory. Amplitudes, periods, associations and arrival times of Rayleigh waves recorded at selected stations of the WWSSN.

In addition, selected data from the long-period arrays (LASA, NORSAR, and ALPA) were provided by the Seismic Data Analysis Center (SDAC) and Texas Instruments.

## 2. Association

The most difficult problem encountered thus far has been in the development of an optimum automatic scheme to be used in the association of the 15,000 long-period readings with the 996 ISM events. Although in many cases associations were made by the readers, the criteria for declaring an association were not uniformly set down nor were the cases of multiple associations adequately recorded. The association schemes studied all follow the same pattern. The velocity of each Rayleigh phase was computed using the origin times of earthquakes in the previous two hours, and this velocity was compared with a theoretical group velocity. If the observed group velocities fell within a window centered on the theoretical group velocity for the appropriate period, an association was declared. Multiple associations were allowed and recorded.

Initially, the theoretical group velocity was taken as an average between pure continental and oceanic extremes, and velocity windows of  $\pm 0.7$ ,  $0.5$ , and  $0.3$  km/sec were used. Then a more elaborate scheme to estimate the theoretical group velocity was employed in which the earth was divided into  $15^\circ \times 15^\circ$  sectors and each sector was designated as oceanic, continental, or mixed. For each attempted association, a path was traced from the station to the hypothetical epicenter and a path parameter, based on the percentage of the path in the various sectors, was assigned. A continental or oceanic group velocity curve was employed if the path was more than 50 percent either one. Otherwise, an average group velocity curve was used to compute the theoretical group velocity. In this scheme, the observed velocity had to fall within  $\pm 0.2$  km/sec of the theoretical one in order for an association to be declared.

These methods were tested on all 1995 readings of main Rayleigh phases made by the Lincoln Laboratory Group for the first 10 days of the ISM. A second test was made on a subset of those readings with amplitudes of 3 mm or more on the original seismogram. The results of these tests are shown in Tables I-5 and I-6. Table I-5 shows the number of times that all individual readings and those of the subset were associated with an event using the various association methods. In the sense that the method which yields the maximum number of unique associations is the optimum one, an average group velocity curve with a 0.5-km/sec window would appear to yield the best results of all the methods tested when all the readings are considered. The percentage of unique associations increases for all methods when only readings of amplitude  $\geq 3.0$  mm



TABLE I-5  
NUMBER OF TIMES THAT LONG-PERIOD READINGS MADE  
DURING FIRST 10 DAYS OF ISM WERE ASSOCIATED WITH EVENTS

	Number of Associations of a Single Reading					Method of Association
	0	1	2	3	4	
Number/percentage of all readings (1995)	793 39	878 44	254 12	57 3	8 0.4	Average velocity ± 0.7 km/sec window
	637 32	936 47	341 17	67 3	11 0.6	Average velocity ± 0.5 km/sec window
	968 48	841 42	160 8	22 1	4 0.2	Average velocity ± 0.3 km/sec window
	1184 59	741 38	64 3	4 0.2	2 0.1	Path-dependent velocity ± 0.2 km/sec window
Number/percentage of readings ≥ 3.0 mm (372)	66 17	184 49	90 24	23 6	7 2	Average velocity ± 0.7 km/sec window
	92 24	199 53	67 18	12 5	2 0.5	Average velocity ± 0.5 km/sec window
	149 40	182 49	38 10	2 0.5	1 0.3	Average velocity ± 0.3 km/sec window
	156 42	196 53	19 5	1 0.3	0 0	Path-dependent velocity ± 0.2 km/sec window

TABLE I-6 NUMBER AND PERCENTAGES OF AGREEMENTS BETWEEN AUTOMATIC ASSOCIATION SCHEMES AND THOSE MADE BY HAND WHEN ONLY ONE AUTOMATIC ASSOCIATION WAS MADE		
Method	All	Percentage
	Like Associations Total Single Associations	
Average velocity $\pm 0.7$ km/sec window	694 878	0.79
Average velocity $\pm 0.5$ km/sec window	740 936	0.79
Average velocity $\pm 0.3$ km/sec window	664 841	0.79
Path-dependent velocity $\pm 0.2$ km/sec window	613 741	0.82
Amplitude $\geq 3.0$ mm		
Average velocity $\pm 0.7$ km/sec window	155 184	0.84
Average velocity $\pm 0.5$ km/sec window	164 199	0.82
Average velocity $\pm 0.3$ km/sec window	147 182	0.80
Path-dependent velocity $\pm 0.2$ km/sec window	170 196	0.86

are used. This increase is most dramatic for the method which used a path-dependent group velocity and a smaller association window. Assuming that the period and arrival time of the larger phases were read with greater accuracy than smaller ones, we must conclude that path-dependent velocities are justified when the data were based on large, clear phases.

Table I-6 summarizes another test that was made of the association algorithms using the associations made by the readers at Lincoln Laboratory. Based on the same readings as Table I-5, this table shows the number and percentages of times that a unique automatic association agreed with the Lincoln readers' association. If the latter are assumed to be the correct association, then the various automatic methods can be tested on the criteria of number of correct unique associations and percentage of correct associations based on the number of unique associations. Table I-6 shows that when all the data are considered, the average group velocity curve with a 0.5-km/sec window gives the maximum number of agreements, although the percentage of like associations made by this method is the same or less than the others. When the larger amplitude data are considered, the method which uses the path-dependent velocities is slightly better than the others tested. Clearly, criteria other than group velocity could be used in the automatic association of surface wave readings with a list of earthquakes. The amplitude of the surface wave considered with the body wave magnitude, depth, and distance of the event

would certainly help sort out multiple associations. However, such a scheme would have to be applied with care in a discrimination experiment.

Although work continues on an optimum surface wave association algorithm, we have applied the one based on an average group velocity curve and a  $\pm 0.5$ -km/sec window to the entire ISM long-period data set. Using only readings which possess a unique association and the surface wave magnitude formula  $M_s = \log(A/T) + 1.66 \log \Delta + 3.3$  (a vertical Rayleigh amplitude in microns,  $20^\circ \leq \Delta \leq 160^\circ$ , and  $15 \leq T \leq 30$  sec), we have computed an average  $M_s$  based on two or more readings for 264 of the 827 ISM events to which a body wave magnitude ( $m_b$ ) was assigned. In Fig. I-4, we inevitably plot this average  $M_s$  vs the average  $m_b$  of these events. Although there are yet errors in association represented in Fig. I-4, it gives us something to test subsequent schemes against. In order to be considered improvements, other methods of magnitude determination or reading association should reduce the scatter in or add more points to Fig. I-4, or both. Figure I-4 does produce one encouraging note; the circled point is a presumed underground nuclear test at the Semipalatinsk test site in Eastern Kazakh. Without qualifying the remaining events by depth or region, this presumed explosion separates from them rather well.

J. Filson

#### REFERENCES

1. Seismic Discrimination SATS, Lincoln Laboratory, M.I.T. (30 June 1972), Sec. VI, DDC AD-748304; (31 December 1972), Sec. V, DDC AD-757560; (30 June 1973), Sec. I, DDC AD-766559.
2. D. Davies and R. T. Lacoss, "First Results from the International Seismic Month," Technical Note 1973-32, Lincoln Laboratory, M.I.T. (2 July 1973), DDC AD-762921.
3. E. A. Flinn and E. R. Engdahl, "A Proposed Basis for Geographical and Seismic Regionalization," Rev. Geophys. **3**, 123-149 (1965).

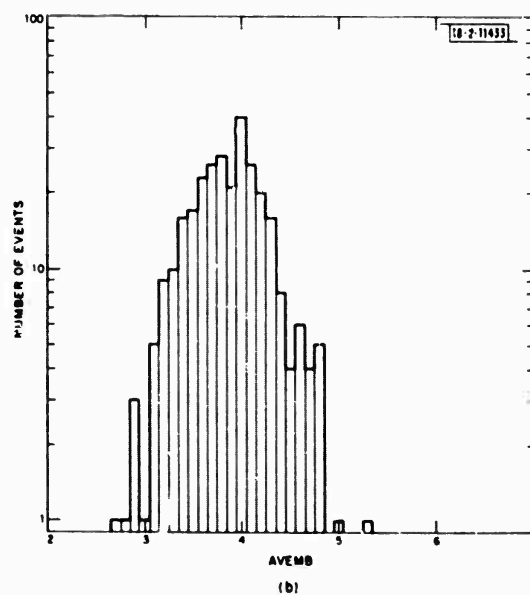
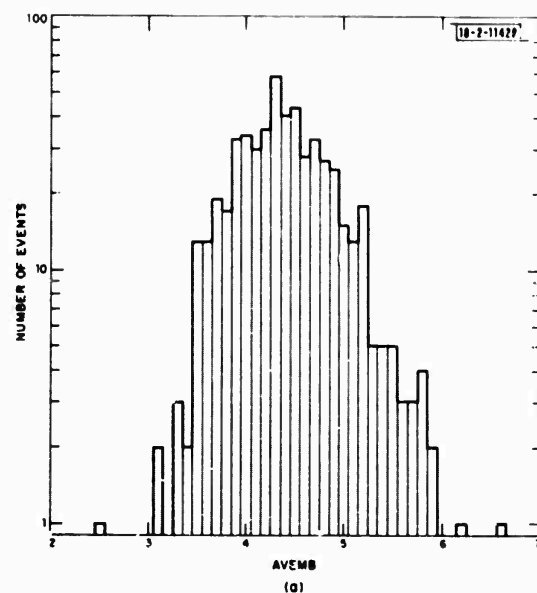


Fig. I-1. Incremental histogram of ISM  $m_b$  (AVEMB) for (a) events graded, A, AI, B, BI, C, and CI, and (b) events graded D or DI which have an assigned magnitude.

-2-11430

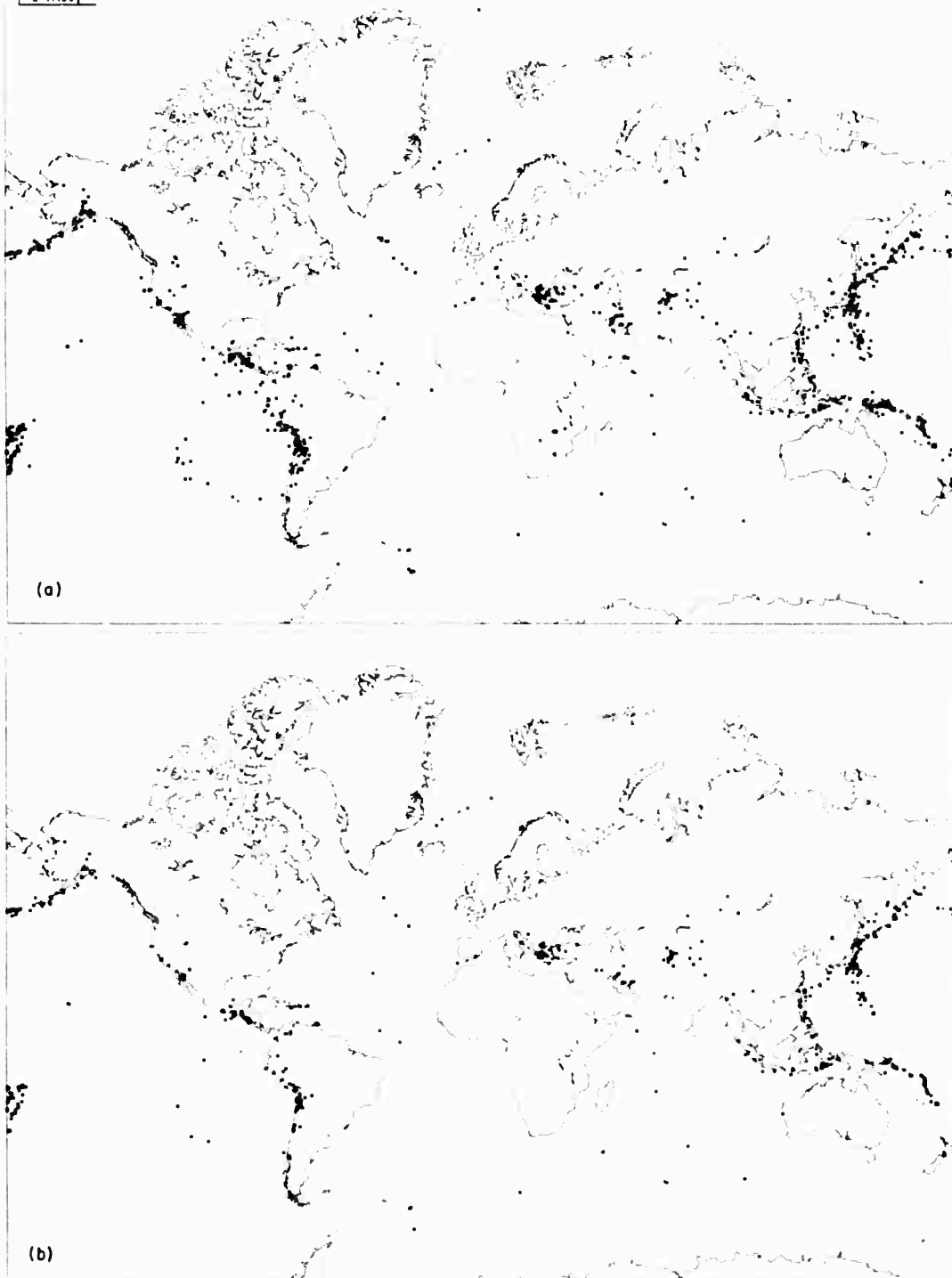
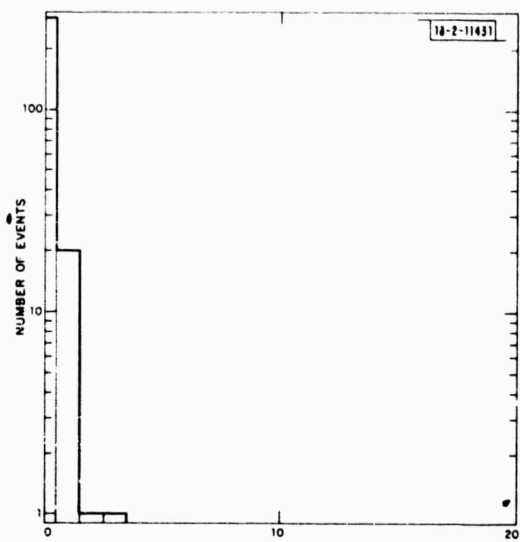
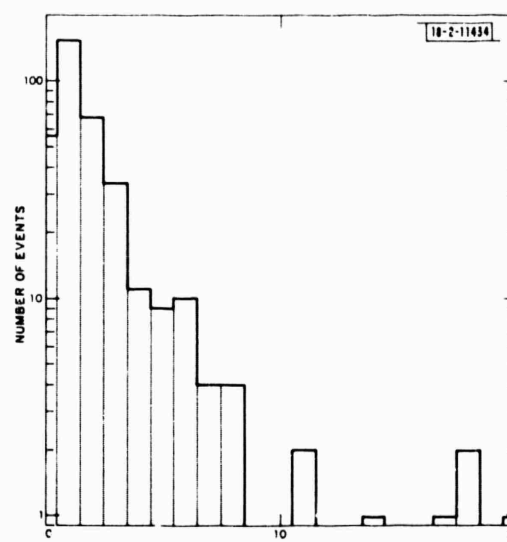


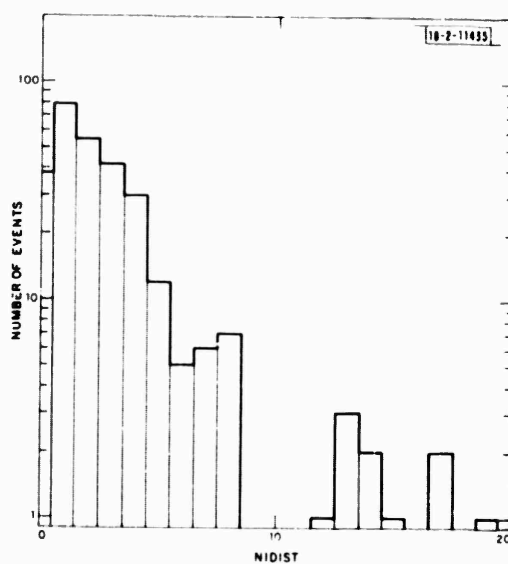
Fig. I-2. Geographic distribution of ISM events: (a) all events, and (b) events of grades A, AI, B, BI, C, and CI.



(a)



(b)



(c)

Fig. 1-3. Histograms comparing A, AI, B, BI, C, and CI grade ISM epicenters with (a) USGS Preliminary Determination of Epicenters list, (b) LASA daily bulletin, and (c) NORSAR daily bulletin. Units are degrees.

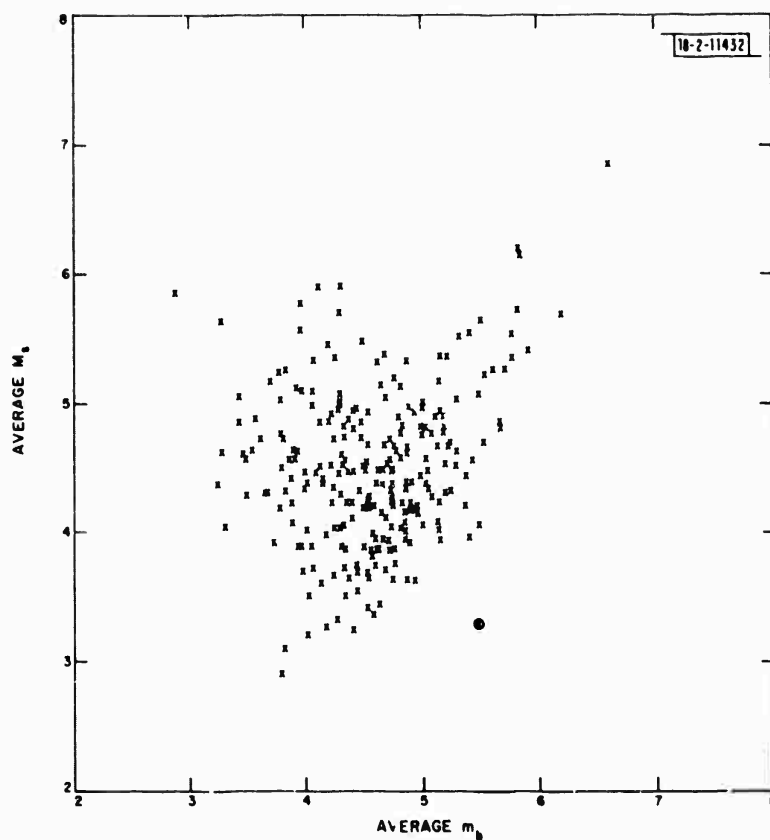


Fig. 1-4. Average  $M_s$  vs average  $m_b$  for 264 events of ISM. Average  $M_s$  determinations are based on two or more measurements in restricted period and distance range. Only unique associations from one of association schemes was used. Circled point is presumed explosion in Eastern Kazakh.

## II. ARRAY STUDIES

### A. NORSAR EPICENTER AZIMUTH ERRORS

A continuing effort to understand the NORSAR epicenter anomalies is producing more interesting results than the LASA epicenter anomalies. The NORSAR azimuth anomaly, in particular, is one that is difficult to understand or approximate with a model. The azimuth anomaly is defined as the difference between the true azimuth to the epicenter and the actual observed azimuth at NORSAR. A least-square fit was made to the subarray arrival times obtained from the event processor that were corrected to remove any misalignment. From this process the velocity, azimuth, and epicenter were obtained. When the array epicenter is plotted with the true PDE epicenter (Fig. II-1), the azimuth error is not only apparent but is quite profound. Because of the character of this anomaly, the primary cause must be the array, with minor secondary effects caused by the epicenter.<sup>1</sup> One cannot account for the azimuth error as a result of a plane-dipping interface at the MOHO. Only in a very general way would a plane-dipping MOHO approximate the azimuth or  $dT/d\Delta$  error. More likely, one needs a dipping MOHO with an egg-shaped bulge under NORSAR. The dip of the MOHO would be westerly while the axis of the dome in the MOHO would be west-northwesterly. Ray tracing is now being used to model the actual data.

R. M. Sheppard

### B. ANALYSIS OF ARRAY DIAGRAMS AT LASA AND NORSAR

A powerful method for the analysis of approach angle, or slowness, anomalies for P-wave signals at an array is based on their representation in slowness ( $dT/d\Delta$ , azimuth) space. Such a representation, known as an array diagram, involves the plotting of these anomalies as arrows, in which the tail represents the  $dT/d\Delta$  and azimuth measured for the P-wave signal at the array, and the head represents the  $dT/d\Delta$  and azimuth that would be obtained from the true, or in this case NOS, location and J-B tables. This approach has been used by Manchee and Weichert,<sup>2</sup> Vinnik and Nikolayev,<sup>3</sup> and by Davies and Sheppard,<sup>4</sup> and Capon<sup>5</sup> at LASA.

A problem of considerable importance is the determination of the various inhomogeneous regions within the earth that are responsible for these P-wave slowness anomalies measured by LASA. These inhomogeneities may be described broadly as due to the following causes:

- (1) Random part of local crust and upper-mantle structure at the receiver,
- (2) Deterministic part of local crustal structure at the receiver,
- (3) Propagation path effects, primarily in the lower mantle, and
- (4) Source region effects, due to structures such as dipping plates of lithosphere.

It has been shown by Capon<sup>5</sup> that the effect, due to the structure listed in item (1), on the P-wave slowness anomaly is negligible. The reason for this is that the LASA tends to average out the effect due to this structure when the slowness of the P-wave is measured by means of a least-squares fit of a plane wave set of arrival times to the actual set of arrival times measured over the entire LASA. This means that the source of the anomaly must then be due to some, if not all, of the structures listed in items (2), (3), and (4).

If the anomaly were caused by a plane-dipping interface directly under the array, the array diagram would consist of a set of error vectors whose magnitudes were all approximately the



same and which all pointed precisely in the direction of dip of the interface. Thus, the effect of a sloping interface can be obtained from the array diagram by fitting a constant vector to the error vectors in the diagram. These results were first shown by Manchee and Weichert,<sup>2</sup> and an example of this has been given by Capon.<sup>5</sup> Davies and Sheppard<sup>4</sup> have pointed out that a slowly varying distribution of arrows, all approximately of equal length and pointing in the same direction, would indicate a bias introduced beneath the array. This bias may not be due necessarily to a dipping interface but, for example, from a distribution or coating of incremental time delays that are not independent of each other for the various directions of approach. That is, these incremental time delays are directionally independent. Thus, the effect of the deterministic part of the local crustal structure at the array, given in item (2), may be obtained by determining the average of all the error vectors in the array diagram. For simplicity, this structure may be considered to be represented by some equivalent plane-dipping interface, and the dip and strike direction for it may be obtained easily from the magnitude and direction of the average vector by using some results due to Niazi.<sup>6</sup> Once the effect due to this structure has been removed, by subtracting the average of all the error vectors from each of the vectors in the array diagram, then the source of the remaining anomaly must be due to the structures in items (3) and (4).

In the previous SATS,<sup>1</sup> a method of analysis based on the array diagram was presented which showed that the crust, upper, and mid-mantle structures directly beneath LASA were responsible for most of the P-wave slowness anomaly. The proof was, of necessity, only heuristic in nature since there is no unique way in which earth structures can be defined as responsible for the anomaly. However, additional results are now presented to support the proof presented previously, and similar results for the NORSAR are also presented.

The basis of the proof presented in the previous SATS<sup>1</sup> is that the spatial rate of variation of the error vectors can, at least formally, be associated with heterogeneities at certain depths in the earth. The more rapid these spatial variations become, the more distant from LASA the heterogeneities must be placed to explain the anomalies. Some artificial array diagrams are now presented, for hypothetical earth structures, to support this conclusion. All these results were obtained by using a ray-tracing program which is based on the computational procedure of Niazi<sup>6</sup> for finding the slowness of a ray which is refracted by a plane-dipping interface. The first example deals with the corrugated surface proposed by Greenfield and Sheppard,<sup>7</sup> as a model for the MOHO under LASA, in order to explain the source of the anomaly. The array diagram for this structure is shown in Fig. 11-2, and it is seen that a relatively slowly varying distribution of arrows, all approximately of equal length and pointing in almost the same direction, is obtained. This result agrees with the notion that such a distribution of arrows should be associated with a structure located beneath the array.

The average vector in Fig. 11-2 has a magnitude of 0.66 sec/deg, and points at an azimuth of 340°. By using the procedure of Niazi<sup>6</sup> once again, it is possible to show that this error vector is due to a hypothetical plane-dipping interface under LASA with dip of about 8° and direction of dip at an azimuth of 340°, assuming that the ratio of crustal-to-mantle velocity is 0.75. These parameters correspond roughly with those of a plane which might be considered as a least-squares fit for the corrugated surface. That is, this average plane can be considered as one which intersects the corrugated surface in such a way as to minimize the sum of the squares of the deviations between them. The error vectors in the array diagram in Fig. 11-2 can be considered as due primarily to this average plane, with small deviations introduced due to the effect of the corrugated surface.

The second example deals with a pyramidal structure whose apex is located 150 km beneath the center of LASA. The dip angle, for all four sides of the pyramid, is  $10^\circ$  and the dip direction of one of the sides is at an azimuth of  $45^\circ$ , so that, of course, the dip directions for the other sides are  $135^\circ$ ,  $225^\circ$ , and  $315^\circ$ . The velocity contrast across the structure is taken as 0.85. The array diagram for this structure is shown in Fig. II-3, and it is seen that a relatively rapidly varying distribution of arrows is obtained. It is recalled from Fig. III-6 of the previous SATS<sup>1</sup> that the horizontal cross section of the disk in the 75- to 225-km depth range, at a depth of about 150 km, is equal to about four times the area of the LASA aperture. As a consequence, it was shown<sup>1</sup> that there should be four independent error vectors introduced in the array diagram by a structure located at a depth of 150 km. It is expected, therefore, that the array diagram in Fig. II-3 should contain four independent error vectors. This is not exactly true, but can be considered as a reasonable approximation. For example, the array diagram in Fig. II-3 can be divided into four equal quadrants, and within each particular quadrant the average vector can be found, and it can be used to replace the vectors within the quadrant. The array diagram obtained in this manner contains four independent vectors and can be considered a good approximation for the result in Fig. II-3. It should be noted that the orientation of the axes used to obtain the quadrants is not particularly important, as a good approximation is obtained for all such orientations. Thus, this example also provides further corroboration for the heuristic proof presented in the last SATS.<sup>1</sup>

The analysis procedure described previously<sup>1</sup> has been applied to the array diagram at NORSAR. The decomposition of the region directly under NORSAR is shown in Fig. II-4, and differs somewhat from the corresponding result for LASA shown in Fig. III-6 of the previous SATS, since the aperture of NORSAR is 110 km as compared with 200 km for LASA. The original data consisted of 722 error vectors. However, in order to provide uniform coverage in the array diagram, a data decimation scheme was used in which the array diagram was divided into a grid of  $20 \times 20$  cells, where each cell is a square of  $1 \times 1$  sec/deg. The first ten vectors to fall within a given cell were taken as acceptable data. This led to a total of 218 error vectors as shown in Fig. II-5. The average of these error vectors was computed and found to point in the direction corresponding to an azimuth of  $286^\circ$ , with a modulus of 0.52 sec/deg. This mean vector could be associated with a plane-dipping interface which dips down at an azimuth of  $286^\circ$ . These parameters could be associated with a mean dip of  $6^\circ$  of the MOHO under NORSAR, assuming a crustal-to-mantle velocity ratio of 0.75, although the MOHO is not necessarily the only source of anomaly.

In Fig. II-6 we have the sum of the average vector and all the vectors obtained using the sub-averaging method described previously.<sup>1</sup> The great similarity of the array diagram in Fig. II-6 with that in Fig. II-5 should be noted. This similarity is also borne out by the small magnitudes of the vectors shown in Fig. II-7 which depicts the difference between the error vectors in Figs. II-5 and II-6. The mean-square value of the error vectors shown in Fig. II-7, relative to that in the original array diagram shown in Fig. II-5, is about -13.5 dB. This means that the analysis procedure has been able to remove more than 96 percent of the original error vectors, when measured in terms of mean-square value of the magnitudes. This should be compared with the corresponding result for LASA of 90 percent obtained previously.<sup>1</sup>

It is also possible to find the mean-square value of the error vectors in each depth range, relative to that in the original array diagram shown in Fig. II-5. The results of such a computation are shown in Fig. II-8, where the ordinate has been labeled as relative amount of heterogeneity. It is seen from this figure that there is an approximately decreasing amount of

heterogeneity as the depth increases. This agrees roughly with the notion that the earth becomes more homogeneous as the depth increases, and agrees reasonably well with the corresponding result obtained previously for LASA.<sup>1</sup>

It should be mentioned that the orientation of the axes used to divide the array diagram into cells, for the purpose of obtaining the sub-averages, is allowed to vary in six steps, from 0° to 75°, with increments of 15° between the steps. The results for the various orientations are averaged to obtain the final sub-averages. In addition, the results for the various orientation angles are similar to each other. This should serve to eliminate any criticism that the analysis procedure is sensitive to the orientation angles employed to obtain the sub-averages. Another refinement used in the method is to apply a two-dimensional triangular weighting function to the data in each cell when the sub-averages are obtained. This is done to prevent the analysis method from being sensitive to large error vectors near the boundaries of a cell. However, the results obtained either with, or without, this type of weighting are quite similar.

It is also possible to sum the average vector and all the vectors obtained using the sub-averaging method at points in the array diagram which do not necessarily represent the original data points, e.g., on a uniform grid. This has been done at both NORSAR and LASA and the results are shown in Figs. II-9 and II-10, respectively. These data can serve to define the P-wave anomalies, and thus the station corrections, from aseismic regions. It should be noted that the anomalies to be expected for the core phases at NORSAR and LASA are also depicted in Figs. II-9 and II-10 respectively.

J. Capon

#### C. A RANDOM MEDIUM ANALYSIS OF CRUST AND UPPER-MANTLE STRUCTURE UNDER NORSAR

The measurement of the P-wave amplitude, phase, and slowness within subarrays at LASA has been considered extensively in the past. These analyses have revealed substantial variations in these quantities between subarrays. Until recently, there was no adequate geophysical model of the crust and upper mantle under LASA which could explain these P-wave anomalies. However, recent work by Aki<sup>8</sup> and Capon<sup>5</sup> has led to the development of earth models which could successfully explain the source of these anomalies in certain cases. This recent work is based on the notion of characterizing the crust and upper-mantle structure under LASA as a random, or Chernov-type,<sup>9</sup> medium.

A similar analysis has now been done at NORSAR. Toward this end, the P-wave amplitude and phase spectra have been measured for a total of 32 events distributed at various azimuths and distances from NORSAR. These spectra were measured over a 5-sec interval starting at a time which is determined by the arrival time at a sensor of the best-fitting plane wave propagating across NORSAR. The slowness of this plane wave is determined from the P-wave beamforming location system at NORSAR. This procedure is similar to that used by Aki.<sup>8</sup> The body-wave magnitudes of the events employed in the study were all larger than about 5.0, in order to insure a reasonably good signal-to-noise ratio.

There were 9 subarrays and 6 sensors per subarray at which spectral measurements were made. These 54 measurements were divided into three sets, and within each set 13 sensors were considered. The subarrays used in each set are:

Set	Subarrays
1	01B, 02B, 03B
2	01A, 04B, 06C
3	05B, 06B, 07B

These sets of subarrays were chosen so that within each set the subarrays are located on similar geologic structures at NORSAR. The particular frequencies used in the analysis were 0.6, 0.8, 1.2, 1.6, and 2.0 Hz. These five frequencies were chosen since they are similar to those used by Aki<sup>8</sup> and Capon<sup>5</sup> in their related work at LASA.

The method which has been used by Aki<sup>8</sup> and Capon<sup>5</sup> to test whether a medium can be considered to be randomly inhomogeneous, in the sense given by Chernov,<sup>9</sup> is as follows. The theoretical relationship, due to Chernov,<sup>9</sup> between  $\overline{B^2/S^2}$  and  $R_{bs}$  for various values of the wave parameter is plotted, as shown in Fig. II-11, where  $\overline{B^2}$  and  $\overline{S^2}$  are the mean-square fluctuations of amplitude and phase, respectively, and  $R_{bs}$  is the crosscorrelation coefficient between the amplitude and phase fluctuations. The 90-percent confidence region is also shown in Fig. II-11, as determined from the size of the sample used in the investigation. The method is to estimate  $\overline{B^2/S^2}$  and  $R_{bs}$  from the P-wave amplitude and phase fluctuations and determine whether these estimates fall within the 90-percent confidence region predicted by the Chernov<sup>9</sup> theory, as given in Fig. II-11. These estimates have been made at NORSAR for the five frequencies and the three sets of sensors indicated previously, and the results of these 15 measurements are shown in Fig. II-11. It is quite clear from the figure that all, except one, of the measurements fall outside the confidence limits. This indicates that the crust and upper-mantle structure under NORSAR does not appear to satisfy the conditions required for a Chernov-type medium.

Measurements were also made of the transverse autocorrelation coefficients of the amplitude and phase fluctuations at 78 ( $=13 \cdot 12/2$ ) spatial lags and six successive values were averaged together, to improve the stability of the results, so that a total of 13 points was obtained. These measurements are shown in Figs. II-12 and II-13 for a frequency of 1.2 Hz and for the second set of sensors, along with the theoretical predictions due to Chernov.<sup>9</sup> These results are typical of those obtained at other frequencies and for other sets of sensors. The results in Figs. II-12 and II-13 show quite clearly that the correlation distance for this particular set of measurements is about 4 km. However, if the entire set of 15 measurements is considered, it is found that the correlation distance varies between about 4 and 8 km, with many of the measurements between 4 and 6 km. Thus, it appears that the average correlation distance for the 15 measurements is about 6 km.

The interpretation of these results is as follows. The wavelength of the P-wave in the 0.6- to 2.0-Hz range varies from about 13 to 4 km, assuming an average compressional velocity of 8 km/sec in the upper mantle. Thus, the wavelengths are larger or, at best, of the same order as the size of the inhomogeneity, or correlation distance. This violates the condition of large-scale inhomogeneities, assumed by Chernov,<sup>9</sup> which requires that the wavelength be much smaller than the correlation distance. Hence, it appears that the Chernov theory may not be applicable to the problem of the scattering of the P-waves under NORSAR. In particular, it appears that multiple, and not single, scattering is taking place under NORSAR, so that the conditions required in the solution of the wave equation by means of the Born approximation are not satisfied. This conclusion was also reached by Aki<sup>8</sup> in his analysis at LASA for frequencies greater than 1 Hz.

J. Capon  
K. A. Bertcussen

#### D. AMPLITUDE AND PHASE VARIATIONS OF SIGNALS WITHIN NORSAR AND LASA SUBARRAYS

P-wave amplitude and phase fluctuations are being studied at subarrays of NORSAR and LASA. The amplitude fluctuations on seismograms recorded at NORSAR appear to be more severe than those at LASA, the main reason being that the high-Q shield structure under NORSAR transmits a wide band of frequencies especially greater than 1 Hz to the sensors. However, LASA is located on crustal sediments over a low-Q upper mantle, which attenuates high frequencies.

As a function of frequency, the amplitude fluctuations within NORSAR subarrays are surprisingly similar to those within LASA subarrays. Here we present some observations of amplitude and phase variation within the subarray of NORSAR and LASA for a presumed explosion in Eastern Kazakh on 6 June 1974. In order to equalize the subarray size at each array, six outer ring sensors and the center sensor of each subarray at LASA were used, and at NORSAR all five outer subarray sensors and center sensors were used. Figure II-14 shows a comparison between typical subarrays at LASA and NORSAR.

At each subarray, the Fourier spectral ratio of each sensor to the subarray beam was computed using 10 sec of P-wave data. From the spectral ratios, the mean and standard deviation of the amplitude and phase delay spectra were computed for each subarray. The phase delay is defined here to be the time delay in seconds of each frequency component. It is given by  $-\phi(\omega)/\omega$ , where  $\omega$  is in radians/second and  $\phi(\omega)$  is the unwrapped phase of the spectral ratio.

Figure II-15 shows the mean and standard deviation of the amplitude spectral ratio at two subarrays at NORSAR and LASA. Subarrays 6C at NORSAR and F3 at LASA are typical of the best quality subarrays for this event. The mean amplitude spectral ratio of sensor to subarray beam is very flat over the frequency band 1 to 2.5 Hz for both subarrays. The dashed lines show the amplitude ratio plus and minus the standard deviation across each subarray. Below these plots are the mean phase delay in seconds with standard deviation scatter limits for the same subarrays. For both subarrays, the mean phase delay is nearly 0 sec, indicating that all frequency components of the single sensor are in phase with the beam components.

In Fig. II-16, a similar set of amplitude and phase delay data is displayed for a pair of poor-quality subarrays at NORSAR and LASA, 1C and C4 respectively. These plots illustrate the effect of incoherent sensors on the subarray beams. Due to destructive interference, the subarray beams are deficient in certain frequencies, causing peaks in the spectral ratio of sensor to beam. Such peaks are seen between 1 and 2 Hz in this figure. A corresponding scatter in the phase delay data is also seen.

At 1 Hz, the standard deviations at the LASA and NORSAR subarrays are rather similar for the event considered. These deviations are shown in Fig. II-17; the average deviations are 2.4 dB at NORSAR and 1.9 dB at LASA, an insignificant difference.

If we examine how the standard deviations vary with frequency, it clarifies why the seismogram amplitudes show more variation at NORSAR than at LASA. Figure II-18 shows the standard deviations for four NORSAR and four LASA subarrays. The subarrays from both arrays show a similar increase in standard deviation from 1 to 2 Hz, and no clear differences in scatter can be observed between LASA and NORSAR. However, events arriving at NORSAR very often have spectra peaking at higher frequencies than at LASA. These signals therefore experience more scatter and amplitude variation on NORSAR records than at LASA.

C. W. Frasier

## 11. P-WAVE AMPLITUDE PATTERNS ACROSS NORSAR

In the previous SVES,<sup>1</sup> the strong frequency dependence of short-period P-wave amplitudes at NORSAR was demonstrated. One important conclusion was that trace amplitudes in nanos/sec. and were too crude a measurement to adequately describe the amplitude variations across NORSAR.

Efforts are under way to calibrate the spectral amplitude variations at NORSAR as a function of azimuth and distance of the incoming events. The purpose of this is to provide a data base which can be used in conjunction with the subarray time residuals obtained by Sheppard (see p. 12 in Ref. 11) to determine the crustal structure under NORSAR. This could provide an independent check on the NORSAR model proposed by Kanestrom<sup>10</sup> which was deduced from  $P_n$  studies of local events in Scandinavia.

The computational scheme presented here is to form beams using the center sensors of each subarray, and compute the spectral ratio of each center sensor to the beam. Events were chosen which all have good signal-to-noise ratios at a common frequency, here taken to be 1 Hz.

Thus far, eleven events have been processed in this manner; they are listed in Table II-1 arranged in order of increasing back azimuth from NORSAR to each epicenter. Figure II-19 shows the configuration of back azimuths for these events on a map of NORSAR.

For each of the above events, 10 sec. of each subarray center sensor were tapered using a one-sided cosine window. The tapered signals were then Fourier transformed and smoothed again in the frequency domain. The spectral ratio of each signal to its corresponding beam was computed at 1 Hz in decibels, and plotted on a map of NORSAR. The resulting maps were automatically contoured by computer using a simple scheme. The array was divided into triangular facets, each triangle having three subarray positions as vertices. The three amplitudes at the vertices were used to define a plane of dipping amplitude over which amplitudes vary linearly. Contour lines are therefore straight lines on each triangular facet, which always connect with other contour lines on adjacent facets. The purpose of this was to produce simple, unique maps not subject to interpretive smoothing by the analyst.

Figures II-20(a) through (k) are the contoured maps of amplitudes with 2-dB contour intervals. The figures are in the order of increasing azimuth of events in Table II-1, and this sequence is the most interesting one to examine. Figures II-20(c) and (d) are amplitude maps for two presumed explosions in Eastern Kazakh and they are quite similar. In Fig. II-20(b), the amplitude for a Banda Sea earthquake is shown. This event is nearly in the shadow zone at a distance of  $109^\circ$ , yet it produces an amplitude map with many features similar to those in Figs. II-20(c) and (d). This is because the Banda Sea event has an azimuth close to that of the Kazakh events. Figures II-20(e) and (f) show very similar amplitude patterns for two Hindu Kush earthquakes with different depths. Clearly these patterns are caused by crustal and mantle structure under NORSAR, yet the patterns are so sensitive to event azimuth that Figs. II-20(e) and (f) are quite different from (c) and (d), the difference in azimuth between the two pairs of events being only about  $20^\circ$ . A similar difficulty occurs in Figs. II-20(h) and (i) which show dissimilar patterns for two events with azimuths differing by only  $10^\circ$ .

This suggests that some smoothing with azimuth may be required in order to adequately model the transmission response of the structure under NORSAR.

TABLE II-1 TABLE OF EVENTS USED IN AMPLITUDE STUDY							
Event	Date	Origin Time (GMT)	Region	Magnitude (m <sub>b</sub> )	Depth (km)	Distance (deg)	Azimuth (deg)
1	10-30-71	14:16:23.6	South of Honshu	5.6	393D	77.8	44.0
2	7-8-71	19:07:00.4	Banda Sea	6.3	33N	109.8	67.7
3	6-6-71	04:02:57.1	Eastern Kazakh	5.5	0	38.4	74.1
4	6-30-71	03:56:57.2	Eastern Kazakh	5.4	0	39.0	73.2
5	8-4-71	01:59:03.1	Hindu Kush	5.0	206	44.5	95.1
6	6-26-71	22:23:29.0	Afghanistan-USSR Border	5.0	127	44.9	94.7
7	9-30-71	21:24:11.0	South Atlantic	6.0	33N	61.5	197.1
8	1-12-72	09:59:10.3	Western Brazil	5.9	580	92.4	260.3
9	9-13-71	04:18:01.9	Dominican Republic	5.7	48	69.6	270.5
10	7-8-71	14:00:00.1	Nevada Test Site	5.5	0	73.5	317.7
11	9-4-71	15:53:25.4	Unimak Islands	5.8	107	65.1	355.9

In conjunction with this work, a program is being written to compute the three-dimensional diffracted field transmitted by realistic models<sup>10</sup> of the MOHO under NORSAR. The method is based on an application of Green's theorem described by Trorey<sup>11</sup> as used in seismic exploration work.

C. W. Frasier

#### F. EFFECTS OF CRUSTAL STRUCTURE BENEATH NORSAR ON SHORT-PERIOD TELESEISMS

Finite difference solutions for teleseismic P-waves emerging into an irregular boundary with an impedance contrast characteristic of the Mohorovicic discontinuity beneath NORSAR have been generated to determine if such a structure can cause the amplitude anomalies observed at that array.<sup>1,12,13</sup> The shape of the boundary is taken from Kanestrom.<sup>14</sup> His model is based on  $P_N dT/d\Delta$  variations across the array and agrees with Sheppard's model<sup>1</sup> based on the travel-time anomalies across the array. Depth to the Mohorovicic discontinuity for the model is contoured in Fig. II-21. The three-dimensional structure has been divided into 2 two-dimensional structures along A-A' and B-B' to facilitate computation. Consequently, the wave solutions will not be valid in the transition regions.

Along A-A', the crust thins about 8 km, in isostatic response to the less-dense rocks comprising the Oslo Graben.<sup>15</sup> This step-like shape is shown in Fig. II-22. The solid line is taken directly from Fig. II-21; the dashed line is the approximation used in the computations. Figure II-23 shows the velocities and densities and illustrates the initial conditions for which solutions were obtained. Plane harmonic 0.5-sec P-waves emerging from the mantle side, with angles of incidence ranging from normally incident to  $\pm 30^\circ$  by  $10^\circ$  increments, were propagated through the model. Solutions at 0.75, 1, 1.25, and 1.5 sec for normal incidence were also obtained. The numerical technique used to solve this boundary value problem is explained by Landers.<sup>16</sup> The solution is approximate in that backscattered radiation in the X-direction is not computed. The grid sizes and the numerical mixing parameter<sup>16</sup>  $\theta$  are also given in Fig. II-23. Figure II-24 shows an equal-amplitude plot of the solution for normal incidence at a period of 1.5 sec. Each character is the amplitude of the wave at that grid point. The alphabet has been used to extend the integers over a range of 1 to 36 (e.g., A = 10). Negative amplitudes are plotted as blanks to accentuate wavefronts (amplitude). The solution at 38 km above the step (i.e., across NORSAR) shows the offset wavefront (time-anomaly) and the amplitude variation along the wavefront caused by the step-like structure below. Figure II-25 shows the time and amplitude anomaly at 38 km above the step for normally incident waves with different periods. The time delay (the constant phase wavefront) is essentially identical for each period. The amplitude anomaly at 1.5 sec indicates that the diffractions from the sides of the step and the refraction from the step are producing significant amplitude variations at 38 km. For 0.5-sec waves, the amplitude is that of a smooth shadow zone above the step with a 2-to-1 amplitude anomaly. Figure II-26 shows the amplitude anomaly for 0.5-sec waves emerging at various angles. With minor variations, the overall shape of the curves remains the same, 2-to-1 anomalies with sharp transition zones. Figure II-27 shows the amplitude of the S-waves produced by conversion at the interface. While the anomalies are very distinctive, these waves are essentially horizontally polarized and so not observable across the array of vertical seismometers.

The same set of solutions computed for the North-South model were computed for the East-West model shown in Fig. II-28. As illustrated, the mantle bows up into the crust, producing an anticlinal structure. Again, the model is consistent with isostatic compensation at the depth



of the Mohorovicic discontinuity for the less-dense rocks filling the Permian Oslo Graben.<sup>15</sup> Figure II-29 gives the pertinent numerical values and illustrates the model and initial conditions for which solutions were obtained. Figure II-30 shows the equal-amplitude plot for a normally incident 1.5-sec-period P-wave. The shape and depth of the anticline defocus the incident wave producing a time advanced lower amplitude wave over the center of the structure. Figure II-31 shows the anomaly as function of period and the time delay which is essentially the same at all periods. Once again, at longer periods, rapidly varying amplitude anomalies of about 4:3 magnitude become a well-defined pair of shadow zones with amplitude anomalies of about 2:1 at short periods. Figure II-32 shows the variations in amplitudes for various incidence angles.

In summary, rather simple structures at the mantle-crust interface can cause 2:1 amplitude variations in teleseismic P-waves over distances as small as 10 km. The size of the anomalies should decrease with increasing period; however, the variations at these periods may not be as smooth. Because of the rapid variation of amplitude over small distances, amplitude anomalies observed at the relatively widely spaced subarrays across NORSAR should not be expected to vary smoothly for events with smoothly changing epicentral co-ordinates. A detailed model of the crust and upper mantle beneath the array could provide deterministic travel-time corrections but would be necessary to compute waveform corrections for improving the array location and detection capabilities.

T. E. Landers

#### G. PHASE VELOCITY AND AZIMUTH DEVIATIONS ACROSS LASA AND NORSAR FOR LOCAL EVENTS

The source of the large amplitude and phase anomalies across LASA and NORSAR has not yet been characterized adequately. Various authors have shown that the effects of a laterally varying sedimentary section,<sup>13</sup> an irregular Mohorovicic discontinuity,<sup>7,17</sup> a random scattering mechanism in the upper mantle,<sup>5,8</sup> and a laterally varying structure in the lower mantle<sup>1</sup> can explain to a certain degree the observed fluctuations in the data. While it is most likely that all of the above contribute to the overall behavior of seismic waves observed across the arrays, it is of primary interest to determine which ones have first-order effects on slowness and travel times if the use of these arrays as arrays is to be maximized. For example, the improvement in detection level could be as much as an order of magnitude if station corrections were deterministic, since a subarray beam at NORSAR may be no larger than the seismogram from a single element of that subarray. To aid in determining the nature of the crust and uppermost mantle beneath the arrays, a study of local and near-regional events has been undertaken. Such data have a distinct advantage over teleseismic data in that wave paths traverse only the region under study. The use of an array of subarrays also has the advantage of having local values of phase velocity and azimuth as well as travel time in the data base.

Tables II-2, II-3, and II-4 show data for a local and a near-regional event at LASA and for a local event at NORSAR. The phase velocity  $C$  and azimuth  $AZI$  at each subarray were determined by time picking the outer 6 elements (5 at NORSAR) and center instrument and least-squares fitting a plane wave to the picks. The rms time error  $\Delta t$ , as well as the rms error in phase velocity  $\Delta C$  and azimuth  $\Delta AZI$  are also given.  $\Delta C$  and  $\Delta AZI$  are computed from the relationship given by Kelly<sup>18</sup>

$$\Delta AZI = \frac{\Delta C}{C} = \frac{\Delta T * C}{N \text{ VAR } X}$$

TABLE II-2					
EVENT AT 45.9°N, 106.6°W, 14:18:00					
Subarray	C	AZI	$\Delta T$ (rms)	$\Delta C$ (rms)	$\Delta AZI$ (rms) (deg)
A0	6.55	198.8	0.0199	0.14	1.3
B1	6.89	210.9	0.0503	0.39	3.4
B2	6.61	203.7	0.0094	0.07	0.6
B3	6.32	187.3	0.0160	0.11	0.9
B4	6.07	196.2	0.0214	0.13	1.2
C1	6.29	194.8	0.0079	0.05	0.5
C2	6.18	203.7	0.0242	0.15	1.4
C3	6.10	194.9	0.0196	0.12	1.1
C4	6.30	182.2	0.0110	0.07	0.6
D1	6.03	208.6	0.0156	0.09	0.8
D2	6.20	208.4	0.0166	0.11	1.0
D3	7.55	184.9	0.0153	0.14	1.1
D4	6.16	183.2	0.0121	0.08	0.7
E1	8.33	195.9	0.0166	0.19	1.3
E2	7.25	230.2	0.0354	0.31	2.3
E3	5.99	203.6	0.0850	0.19	1.9
E4	6.32	166.2	0.0344	0.23	2.0
F1	7.63	204.9	0.0201	0.20	1.5
F2	7.84	267.6	0.0696	0.70	5.2
F3	7.61	110.2	0.0270	0.21	1.8
F4	6.87	172.3	0.0625	0.49	4.1

where  $N$  is the number of elements and  $\text{VAR } N$  is the rms value of one of the orthogonal components of the station locations. The derivation assumes a normal distribution of travel-time errors and a symmetric array. For the LASA configuration (hexagonal),

$$\Delta AZI = \frac{\Delta C}{C} = \frac{\Delta T \cdot C}{\sqrt{3} R}$$

and for NORSAR (pentagonal),

$$\Delta AZI = \frac{\Delta C}{C} = \frac{\Delta T \cdot C}{1.44 R}$$

where  $R$  is the distance from the center to an element of the outer ring. The quantizing error,  $\pm 0.025$  sec, leads to a  $\Delta T$  of 0.01 and a nominal  $\Delta AZI$  and  $\Delta C$  of  $1^\circ$  and 0.1 km/sec, respectively, for both arrays. As seen from Tables II-2 through II-4, the arrivals often differ significantly from plane waves by more than quantizing can account for; however, in general,  $P_g$  arrivals are nearly planar whereas  $P_N$  arrivals are somewhat worse. Figure II-33 shows the azimuths of the E- and F-rings at LASA for the event in Table II-2. The epicenter is well defined in an area of about  $25 \text{ km}^2$ . The  $P_N$  arrival at F1 is about  $10^\circ$  in error. Figure II-34 shows the azimuths for the NORSAR event given in Table II-4. The epicenter here is not nearly as well defined, however, excluding the subarrays lying to the south and east of the dashed line in the

TABLE II-3					
EVENT AT 44.3°N, 105.1°W, 11:44:20.4					
Subarray	C	AZI	$\Delta T$ (rms)	$\Delta C$ (rms)	$\Delta AZI$ (rms) (deg)
A0	8.06	171.3	0.0166	0.18	1.2
B1	9.13	169.3	0.0119	0.16	1.1
B2	9.89	171.6	0.0435	0.70	4.0
B3	7.22	161.2	0.0242	0.21	1.7
B4	7.27	169.3	0.0395	0.34	2.8
C1	7.54	172.6	0.0269	0.25	1.9
C2	7.75	170.2	0.0386	0.38	2.9
C3	9.75	185.4	0.0389	0.61	3.5
C4	7.96	173.0	0.0097	0.10	0.7
D1	7.10	179.1	0.0240	0.20	1.6
D2	7.89	163.7	0.0233	0.24	1.8
D3	8.32	172.3	0.0513	0.59	4.0
D4	6.86	168.8	0.0316	0.25	2.0
E1	8.22	173.9	0.0207	0.23	1.5
E2	8.62	163.9	0.0065	0.08	0.6
E3	9.27	161.1	0.0274	0.15	0.8
E4	11.40	164.0	0.0275	0.19	2.9
F1	7.93	175.1	0.0339	0.35	2.5
F2	7.81	166.7	0.0062	0.06	0.5
F3	9.22	146.6	0.0354	0.50	3.0
F4	7.57	166.8	0.0256	0.24	1.7

TABLE II-4					
EVENT AT 59.9°N, 11.4°E, 16:44					
Subarray	C	AZI	$\Delta T$ (rms)	$\Delta C$ (rms)	$\Delta AZI$ (rms) (deg)
01A	6.69	165.9	0.0036	0.25	0.22
01B	6.70	166.6	0.0171	0.12	1.04
02B	5.96	174.5	0.0297	0.16	1.60
03B	6.11	175.3	0.0102	0.06	0.56
04B	6.23	173.8	0.0187	0.11	1.05
05B	6.73	160.4	0.0158	0.11	0.96
06B	6.74	149.9	0.0206	0.15	1.26
07B	6.72	160.2	0.0334	0.24	2.03
02C	6.81	169.3	0.0240	0.16	1.48
03C	6.60	185.1	0.0087	0.06	0.52
04C	6.47	188.8	0.0087	0.06	0.51
05C	6.11	189.4	0.0176	0.10	0.97
06C	6.34	185.3	0.0152	0.10	0.87
07C	6.58	184.2	0.0192	0.13	1.14
08C	6.07	157.6	0.0331	0.19	1.82
09C	6.82	142.3	0.0300	0.22	1.85
10C	6.73	137.1	0.0320	0.23	1.95
11C	8.14	142.0	0.0350	0.37	2.58
12C	7.30	139.9	0.0329	0.28	2.17
13C	6.75	148.2	0.0300	0.22	1.83

figure (2B, 3B, 5C, 4B, 5C, 8C, and 7C), the epicenter can be located in an area of about 100 km.<sup>2</sup> All the aforementioned subarrays then have large easterly azimuth anomalies. Figure II-35 shows the phase velocity measurements for the same event. The circled values are those for the subarrays with the azimuth anomalies. They are anomalously low in phase velocity. The upper crust beneath NORSAR seems to be divided into at least two provinces. If the difference in crustal velocities (6.1 km/sec average for the SE, 6.7 km/sec otherwise) persisted over 30 km in depth, a travel-time anomaly of 0.4 sec would be expected. In Fig. II-36, the phase velocity at the different subarrays for the two LASA events is plotted with error bars of  $\pm \Delta C$ . The variation in  $P_N$  values is considerably larger than for  $P_g$  values. Whereas at NORSAR the azimuth and phase-velocity variations indicate significant lateral variation in the crust, the values at LASA indicate that the greater variation in structure lies near the Mohorovicic discontinuity.

Continuing analysis of the large number of local strip-mining explosion records at LASA and near events at NORSAR should lead to a better understanding of the crust and mantle beneath these arrays, and that, in turn, may lead to improved array capability.

T. E. Landers  
H. Bungum

## H. LOCATING ABILITY OF LASA AND NORSAR

Large seismic arrays such as LASA and NORSAR have been used singly to locate seismic events on a routine basis for several years, but few attempts have been made to use two or more arrays simultaneously for this purpose. The event location algorithm described in the last SATS<sup>1</sup> enables one to calculate the theoretical resolving power of any network of arrays and/or single stations, and we present here as an illustration of this ability the confidence regions expected when LASA and NORSAR are used separately and in conjunction to locate events in central Asia. Gjoystdal, *et al.*<sup>19</sup> analyzed this problem using a Monte Carlo technique to simulate random errors.

Figure II-37 shows the theoretical resolving power of LASA for shallow events in central Asia. These calculations are based on the assumption that LASA can measure slowness with a standard deviation of 0.05 sec/deg, and thus represent the "best possible" situation in which virtually perfect site corrections for the array sensors are available. Without such corrections, systematic location errors would of course be much larger than those illustrated. The regions shown are formal 50-percent confidence ellipses for a normal distribution of observational errors. Regions of greater confidence have deliberately been avoided, since their size would depend critically on the details of the "tail" of the distribution of measurement errors. The numbers given to the right of some of the ellipses give, respectively, their aspect ratios and areas (in thousands of km<sup>2</sup>). Several points about Fig. II-37 should be noted. The loss of resolution near the bottom of the figure as the core shadow is approached is obvious. The overlap of regions of radically different size indicates that the linearization of the equations implicit in these calculations is not a valid approximation in the large ellipses. The large differences in size between some adjacent ellipses are caused by irregularities in the theoretical slowness-vs-distance curve, and probably are not meaningful.

Figure II-38 shows the corresponding confidence regions for NORSAR (assumed to have a resolution of 0.1 sec/deg). Some of the apparent difference between the ellipticities of the regions on Figs. II-37 and II-38 are the result of distortion introduced by the map projection (cf. the regions at 65°N, 140°E). The regions in the upper-left corner of Fig. II-38 should not be taken seriously, since they are less than 25° from NORSAR, where the travel-time curve is multi-branched and strongly varying regionally.

Figures II-39 and II-40 show the confidence regions expected if LASA and NORSAR are used together to locate events. Figure II-39 is based on an uncertainty in absolute travel times of 1.5 sec, which probably corresponds fairly well to the accuracy obtainable with simple tables. In Fig. II-40, this figure has been reduced to 0.5 sec, which might be obtainable if regional variations were included in the tables. It is evident that accurate arrival-time data are potentially much more useful than slowness measurements, although the earth must be "calibrated" to fully take advantage of them. It is also clear from Fig. II-40 that the optimum location for another low-threshold station would be somewhere in southern Asia.

B. R. Julian

# REFERENCES

1. Seismic Discrimination SATS, Lincoln Laboratory, M.I.T. (20 June 1973), DDC AD-766559.
2. E. B. Manchee and D. H. Weichert, "Epicentral Uncertainties and Detection Probabilities from the Yellowstone Seismic Array Data," *Bull. Seismol. Soc. Am.* 58, 1359-1377 (1968).
3. L. P. Vinnik and A. V. Nikolayev, "The Velocity Profile of the Lower Mantle from Direct Measurements of  $dT/d\Delta$ ," *Izv. Akad. Nauk. Fiz. Zemlya* 11, 24-40 (1970).
4. D. Davies and R. M. Sheppard, "Lateral Heterogeneity in the Earth's Mantle," *Nature* 239, 318-323 (1972), DDC AD-758942.
5. J. Capon, "Characterization of Crust and Upper Mantle Structure Under LASA as a Random Medium," to be published in *Bull. Seismol. Soc. Am.* (February 1974).
6. M. Niazi, "Corrections to Apparent Azimuths and Travel-time Gradients for a Dipping Mohorovicic Discontinuity," *Bull. Seismol. Soc. Am.* 56, 491-509 (1966).
7. R. J. Greenfield and R. M. Sheppard, "The Moho Depth Variations under the LASA and Their Effect on  $dT/d\Delta$  Measurements," *Bull. Seismol. Soc. Am.* 59, 409-420 (1969).
8. K. Aki, "Scattering of P Waves Under the Montana LASA," *J. Geophys. Res.* 78, 1334-1346 (1973).
9. L. A. Chernov, Wave Propagation in a Random Medium (McGraw-Hill, New York, 1960).
10. R. Kanestrom, "A Crust-Mantle Model for the NORSAR Area," *Pure Appl. Geophys.* 105, 729-740 (1973).
11. A. W. Trorey, "A Simple Theory for Seismic Diffractions," *Geophysics* 35, 762-784 (1970).
12. Seismic Discrimination SATS, Lincoln Laboratory, M.I.T. (30 June 1972), DDC AD-748304.
13. *Ibid.* (31 December 1972), DDC AD-757560.
14. R. Kanestrom, "A Crust-Mantle Model for the NORSAR Area," Part II in "Crustal Structure in Southeastern Norway from Seismic Refraction Measurements," Scientific Report No. 5, Seismological Observatory, University of Bergen (30 April 1971), pp. 46-71.
15. I. B. Ramberg, "Crustal Structure across the Permian Oslo Graben from Gravity Measurements," *Nature*, PS 240, 149-153 (18 December 1972).
16. T. E. Landers, "Numerical Solutions for Elastic Waves in Laterally Inhomogeneous Media," Ph. D. Thesis, Stanford University (1971).
17. H. Mack, "Nature of Short-Period P-wave Signal Variations at LASA," *J. Geophys. Res.* 74, 3161-3170 (1969).
18. E. J. Kelly, Jr., "Processing of Limited Network Seismic Signals," Group Report 1964-44, Lincoln Laboratory, M.I.T. (4 September 1964), DDC AD-447220.
19. H. Gjoystdal, E. S. Husebye and D. Rieber-Mohn, "One-Array and Two-Array Location Capabilities," *Bull. Seismol. Soc. Am.* 63, 549-569 (1973).

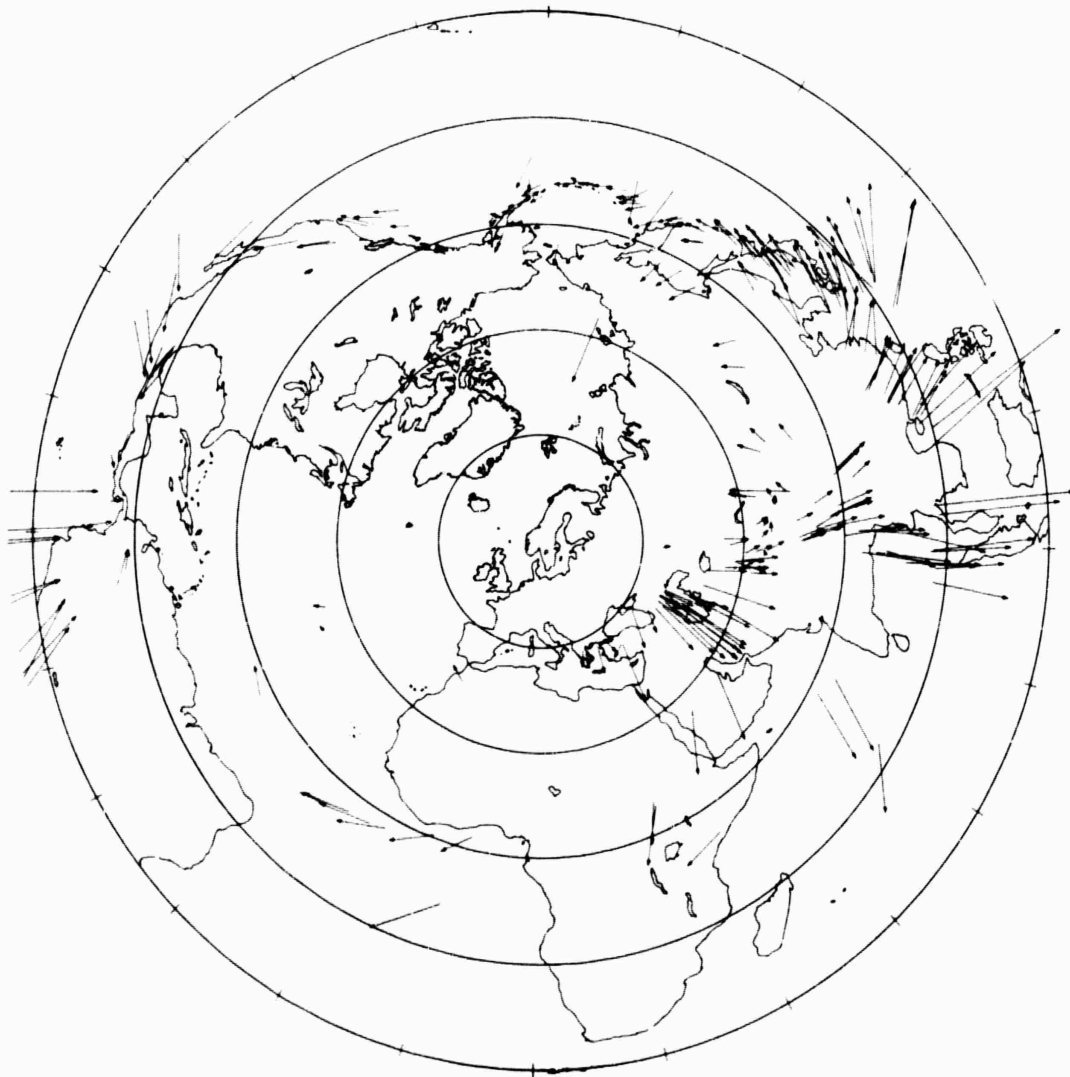


Fig. II-1. NORSAR epicenter location errors. PDE epicenter is arrow head; NORSAR is arrow tail.

18-2-11566

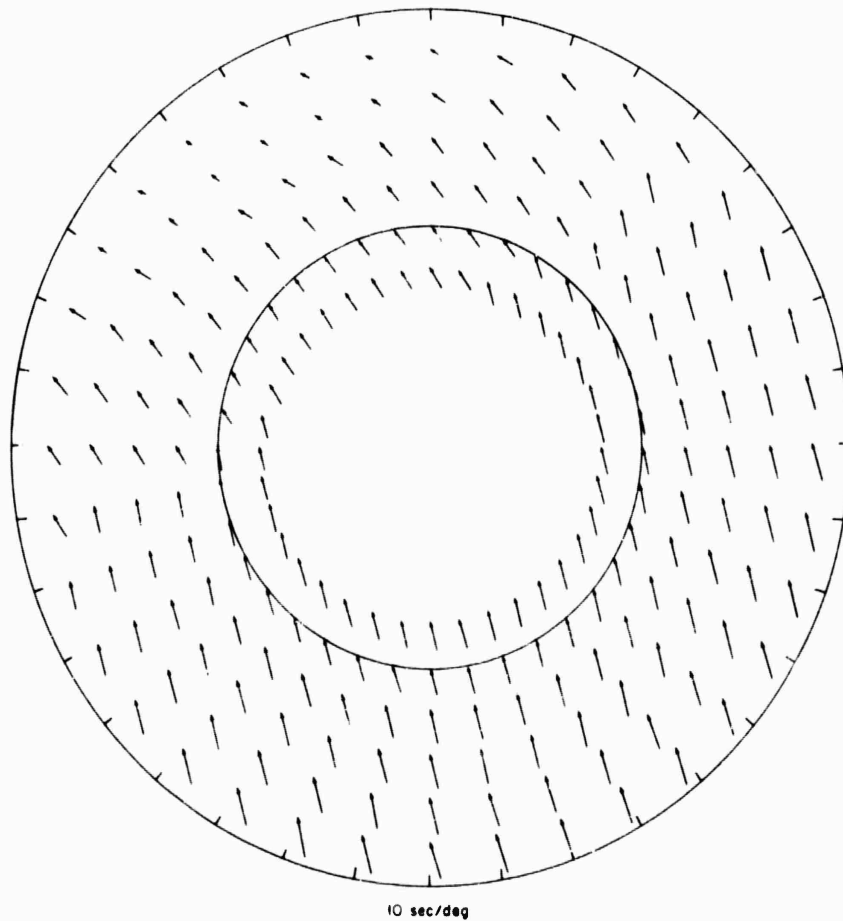
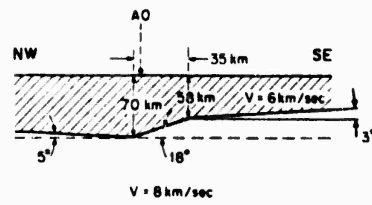


Fig. II-2. Array diagram for Greenfield-Sheppard corrugated surface obtained using ray-tracing program.



10-2-11567

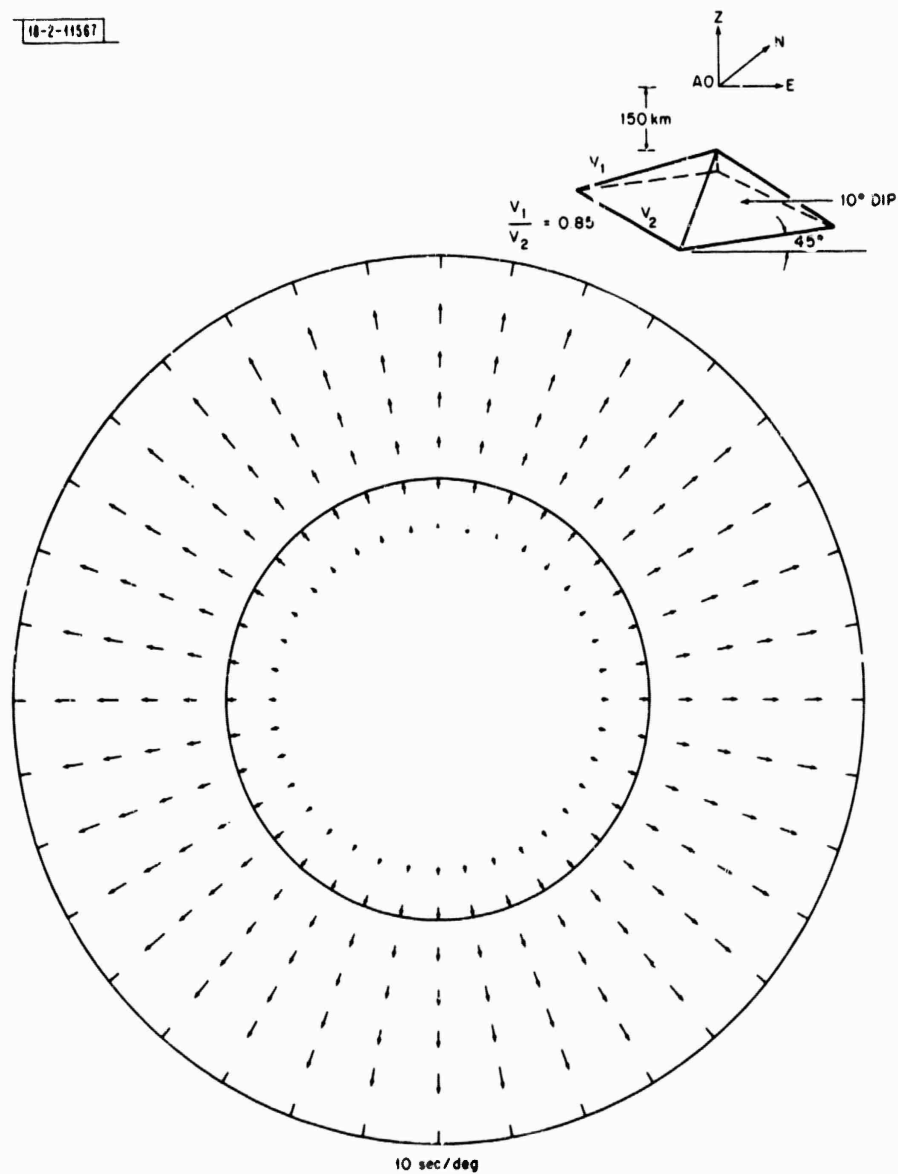


Fig. II-3. Array diagram for pyramidal structure obtained using ray-tracing program.

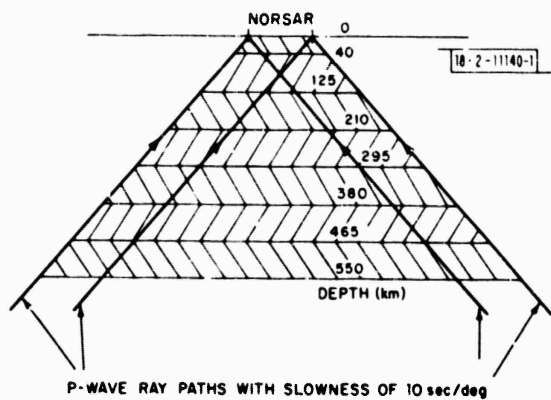


Fig. II-4. Decomposition of region directly under NORSAR.

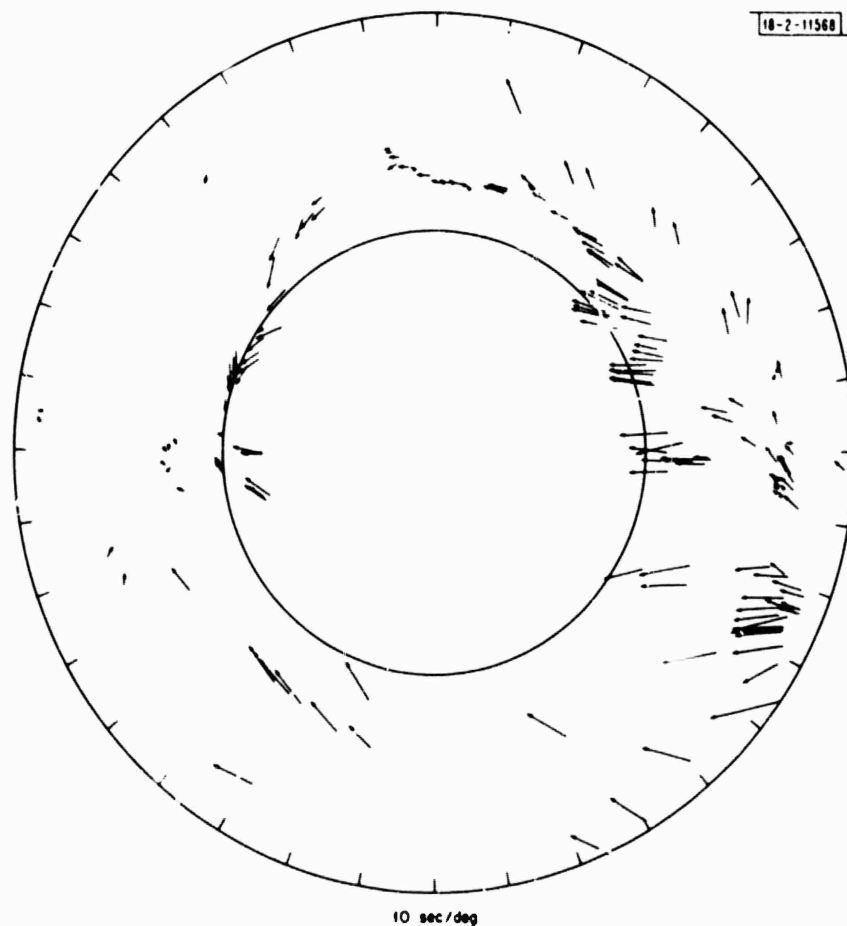


Fig. II-5. Original data used in analysis of array diagram at NORSAR.

18-2-11569

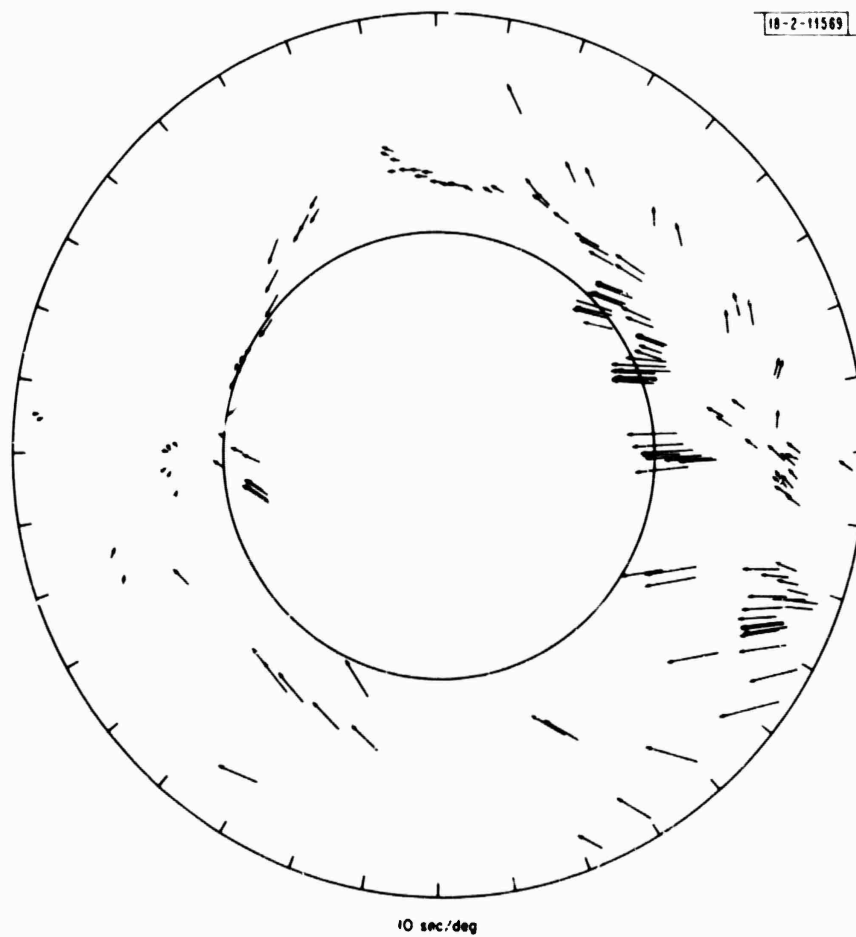


Fig. II-6. Array diagram obtained by adding average and sub-average error vectors at original data points.

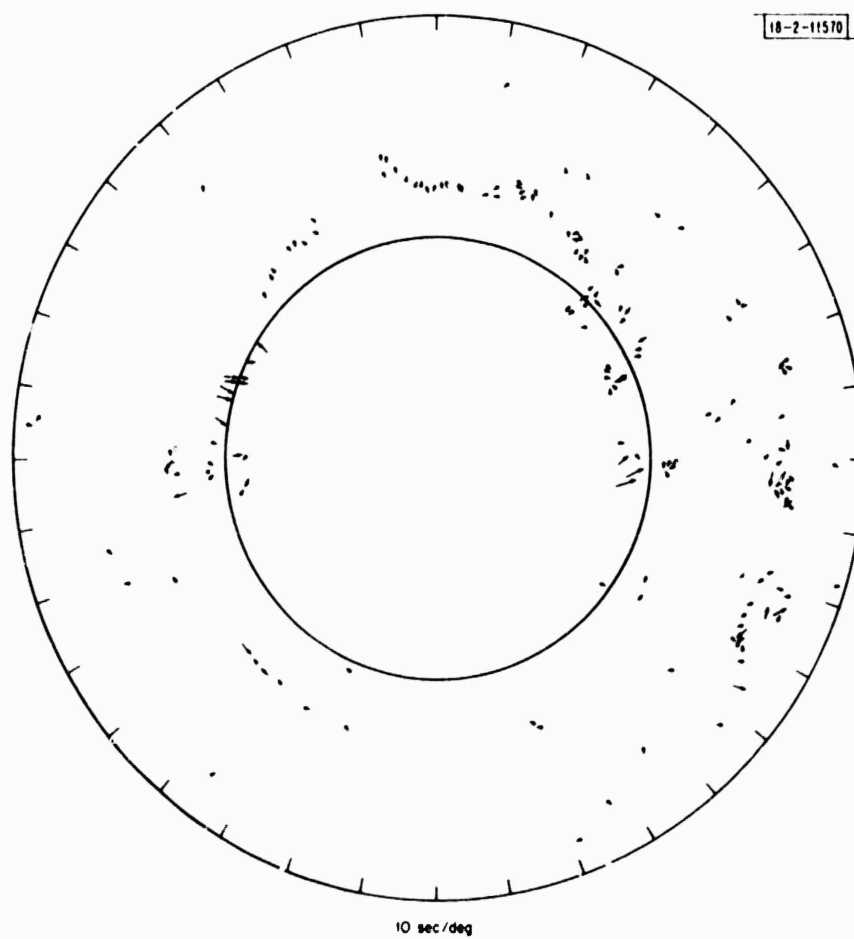


Fig. II-7. Difference between error vectors shown in Figs. II-4 and II-5.

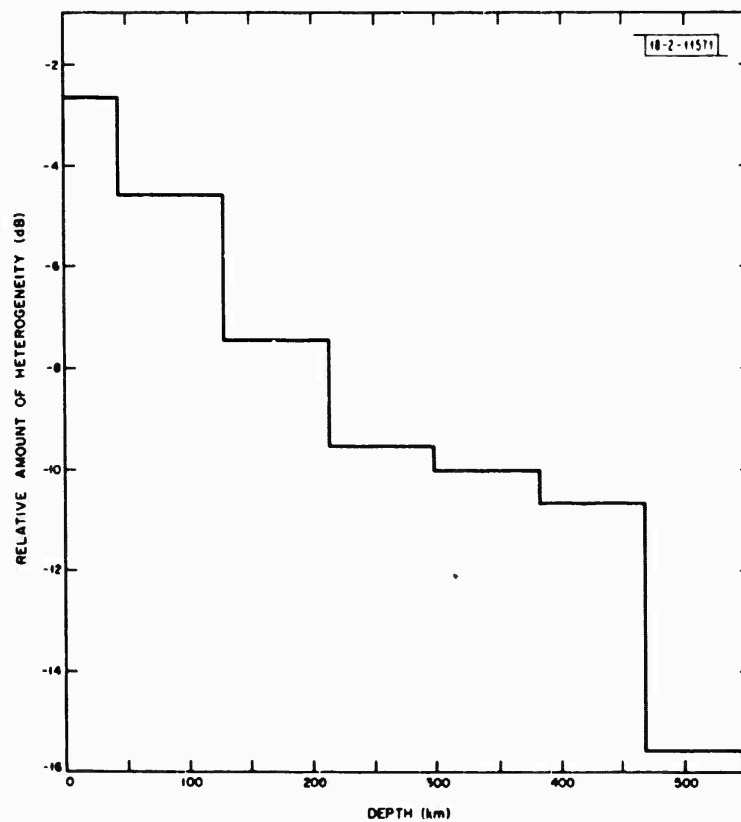
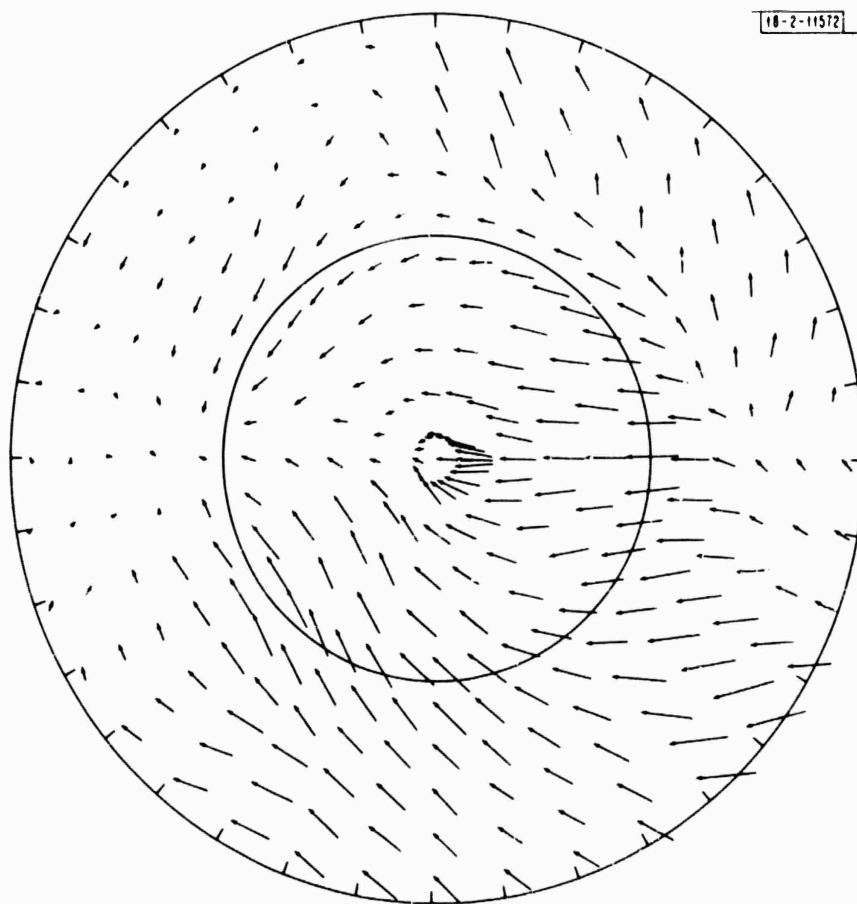


Fig. II-8. Relative amount of heterogeneity vs depth within earth under NORSAR.

18-2-11572



10 sec/deg  
NORSAR

Fig. II-9. Prediction of array diagram at NORSAR based on sum of average and sub-average error vectors on uniform grid of points.

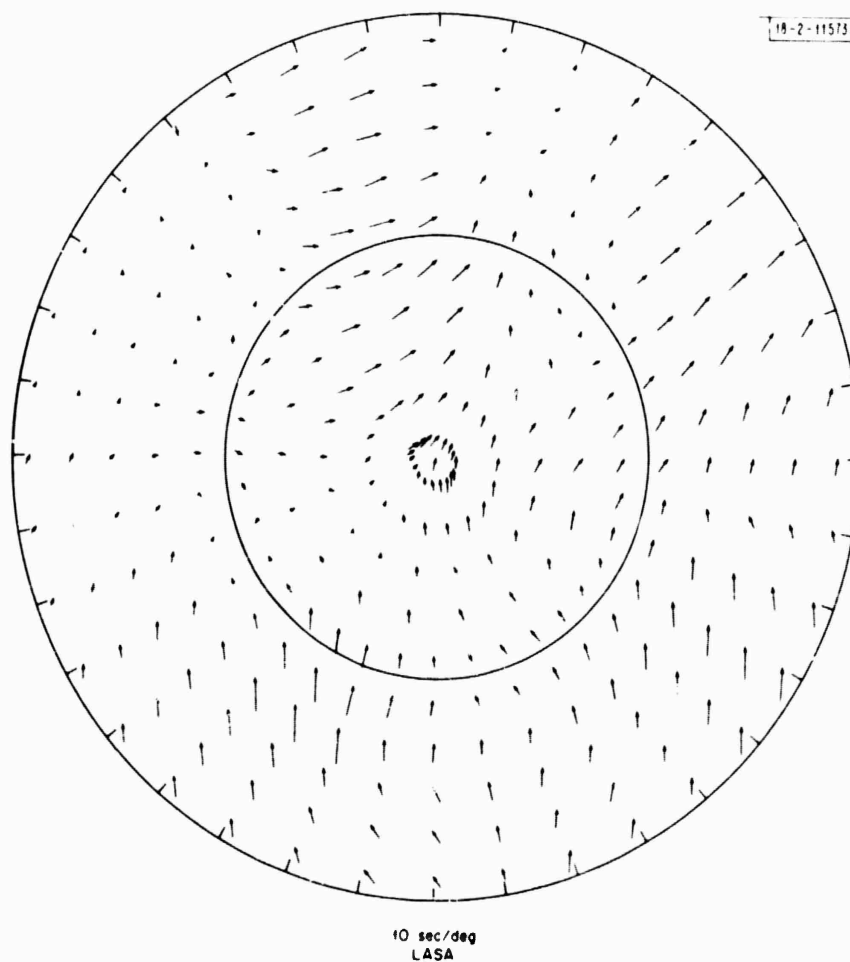


Fig. 11-10. Prediction of array diagram at LASA based on sum of average and sub-average error vectors on uniform grid of points.

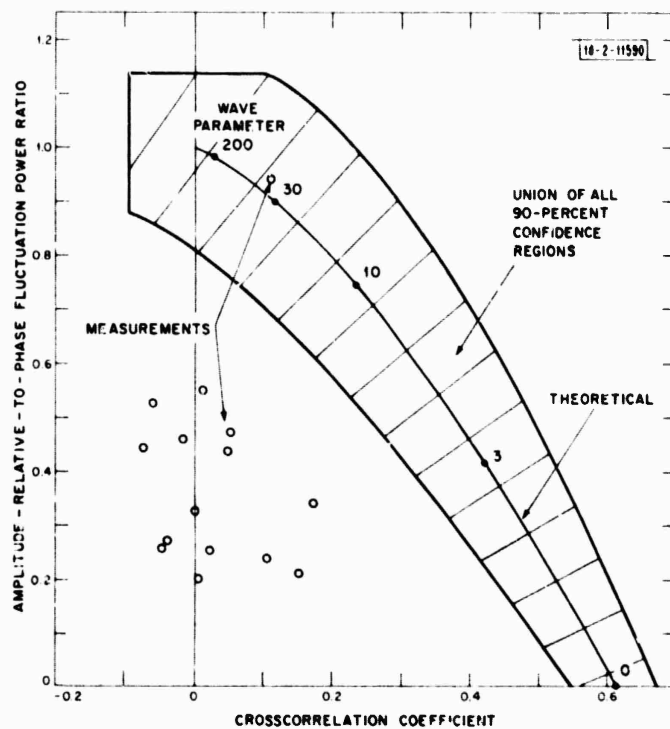


Fig. II-11. Theoretical relationship between amplitude-relative-to-phase fluctuation power ratio and crosscorrelation coefficient between amplitude and phase fluctuation, and the 90-percent confidence limits of measurement.

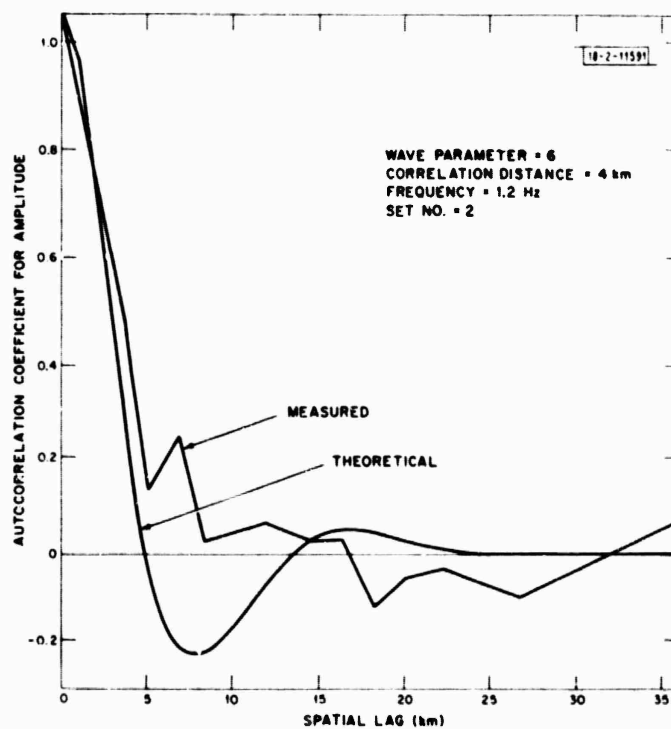


Fig. II-12. Comparison of estimate with theoretical curve for transverse autocorrelation coefficient of amplitude fluctuations.



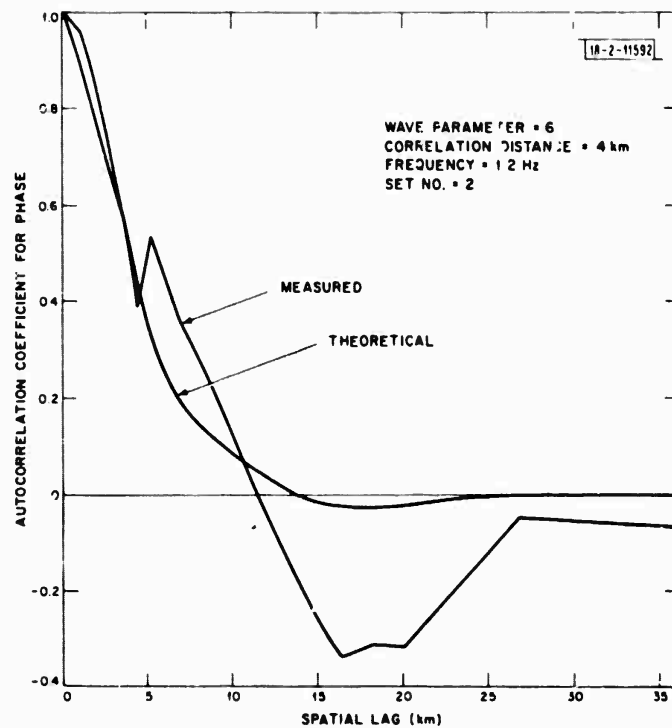


Fig. II-13. Comparison of estimate with theoretical curve for transverse autocorrelation coefficient of phase fluctuations.

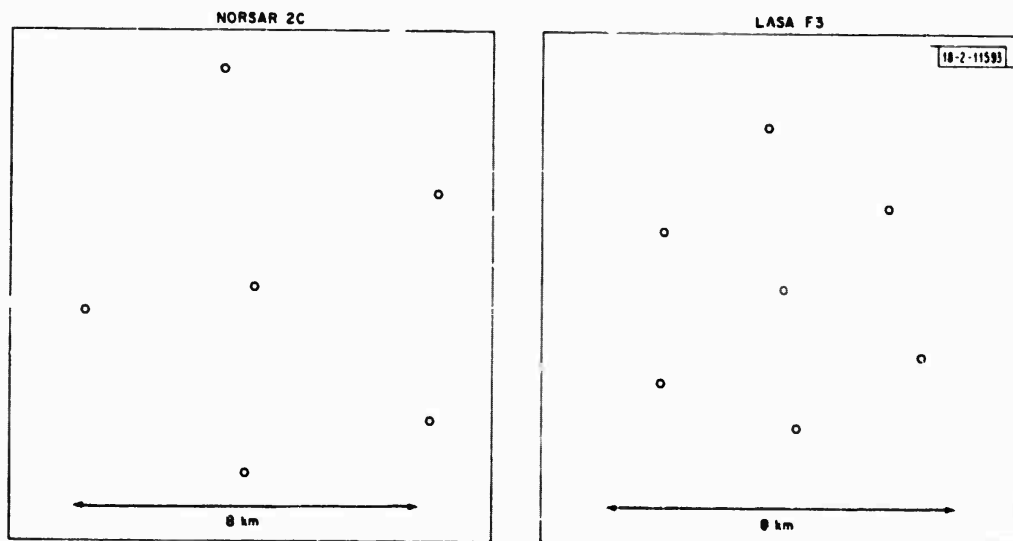


Fig. II-14. Typical subarrays at NORSTAR and LASA. All sensors of 2C at NORSTAR are shown, whereas for F3 at LASA only outer ring and center sensor are shown.

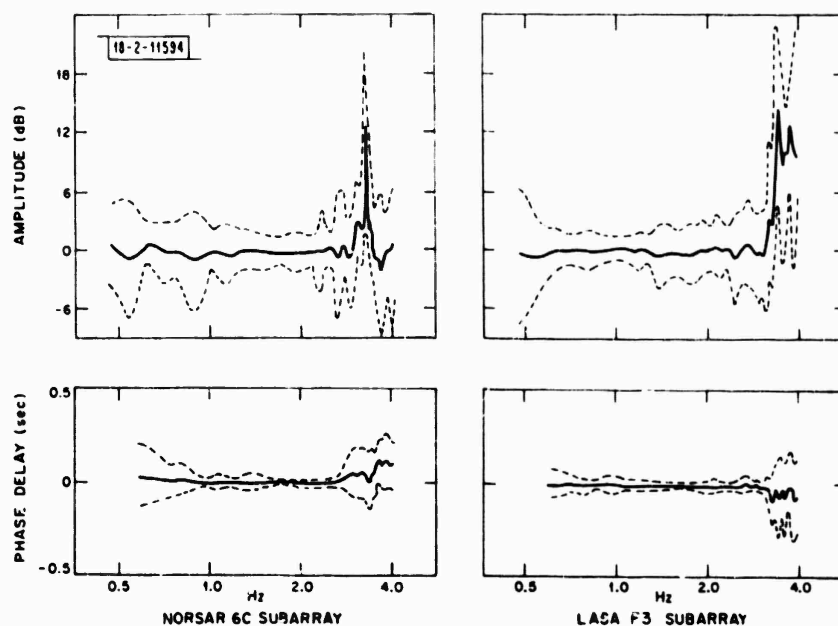


Fig. II-15. Amplitude and phase delay statistics of spectral ratio of single sensor to subarray beam using presumed explosion in Eastern Kazakh, 6 June 1971. Solid lines indicate mean amplitude and phase delay, and dashed lines indicate scatter within a standard deviation of mean. Subarrays 6C at NORSTAR and F3 at LASA are shown.

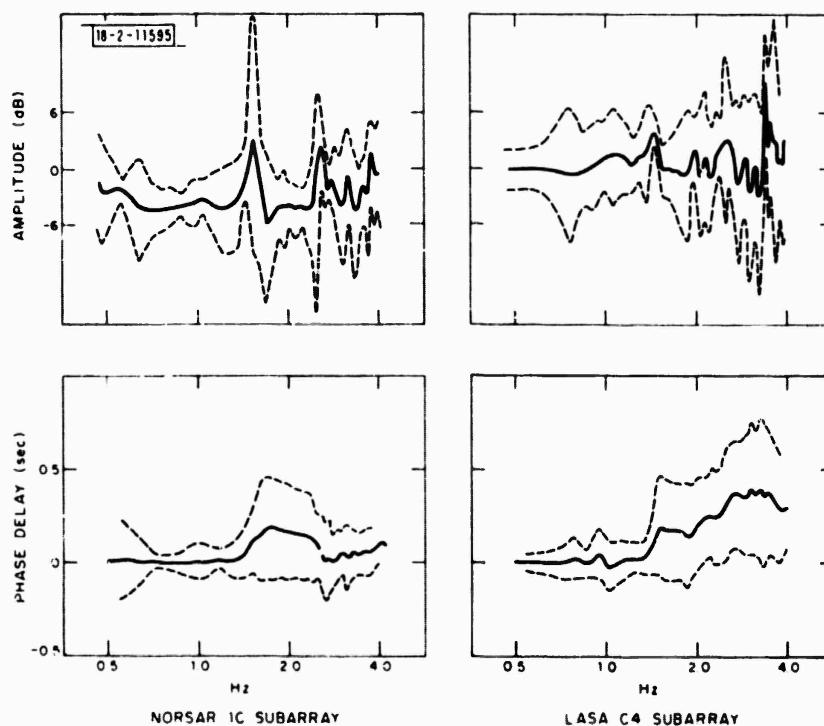


Fig. II-16. Amplitude and phase delay statistics as described for Fig. II-15. In this case, subarrays 1C at NORSTAR and C4 at LASA are shown.

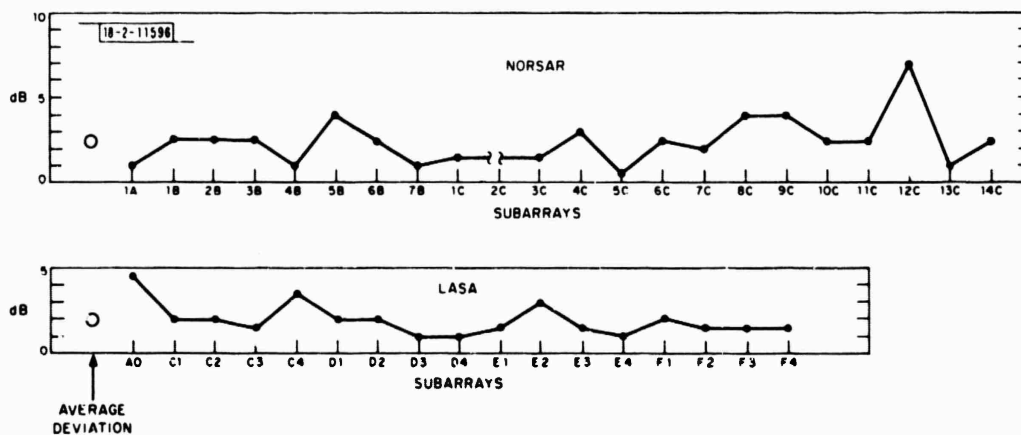


Fig. II-17. Standard deviations at 1 Hz of spectral ratio of single sensors to subarray beams at LASA and NORSAR subarrays. Data used are a presumed explosion in Eastern Kazakh, 6 June 1971.

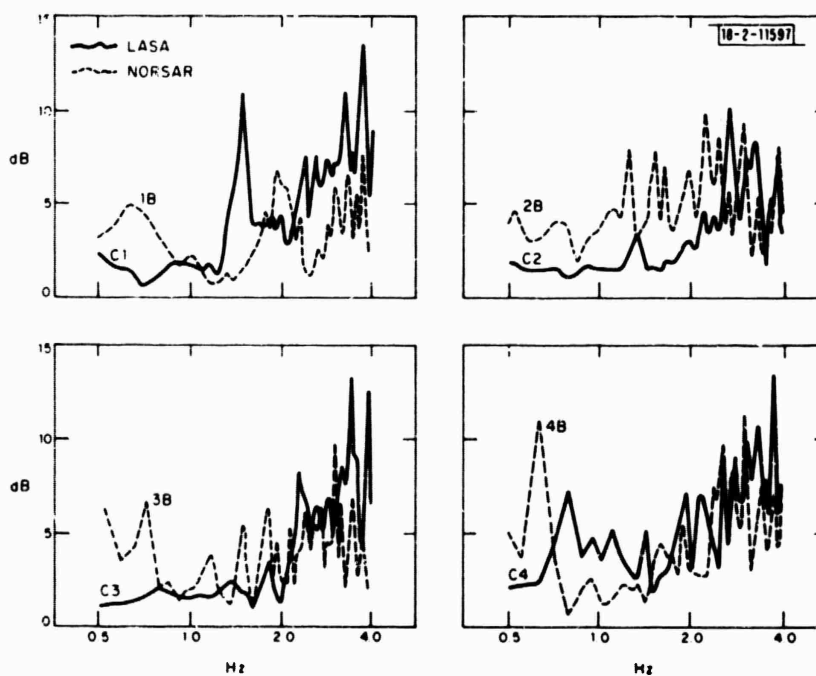


Fig. II-18. Standard deviations of spectral ratios of single sensors to subarray beams. Four typical subarrays at LASA and NORSAR are shown.

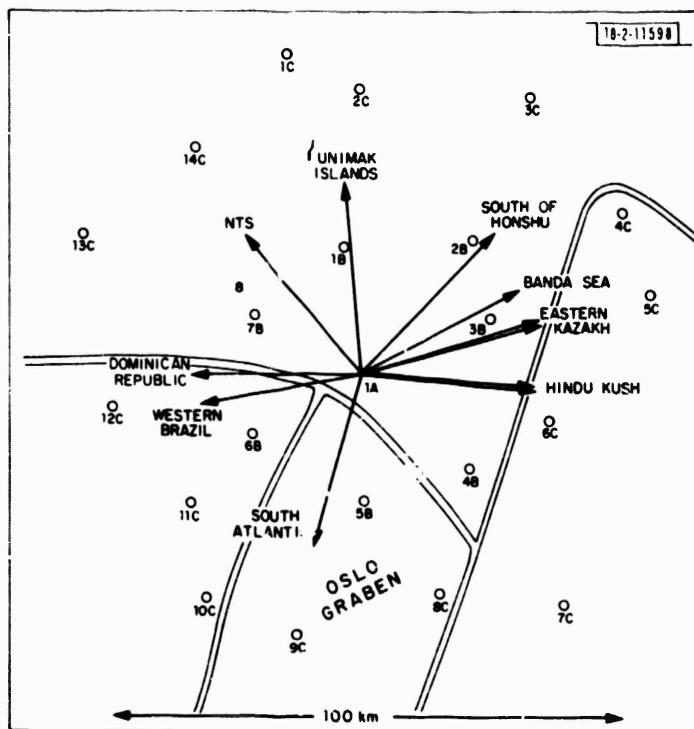


Fig. II-19. Back azimuths from NORBAR to eleven events used in this amplitude study.



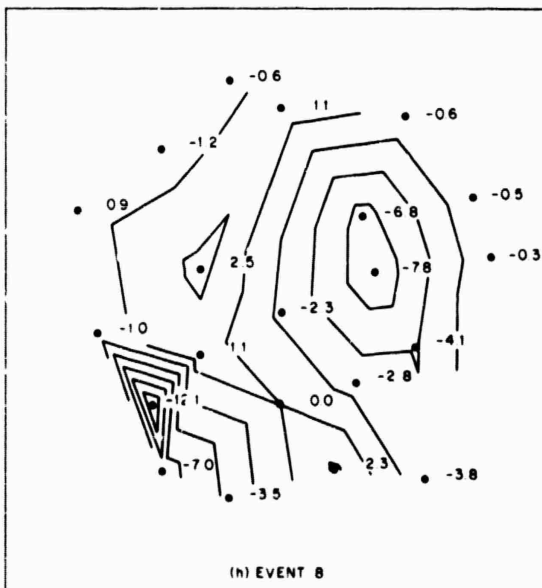
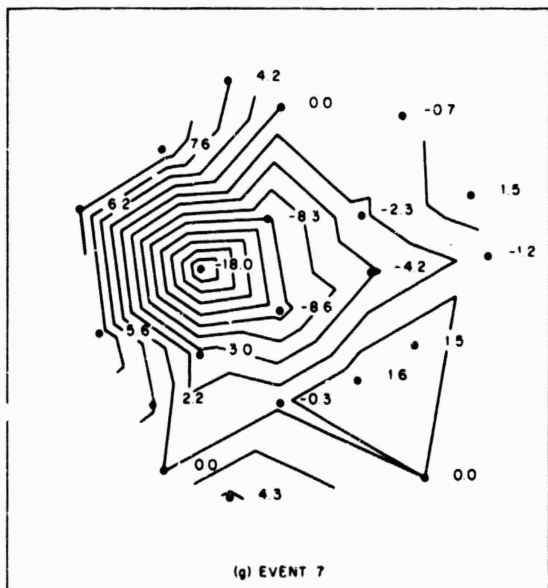
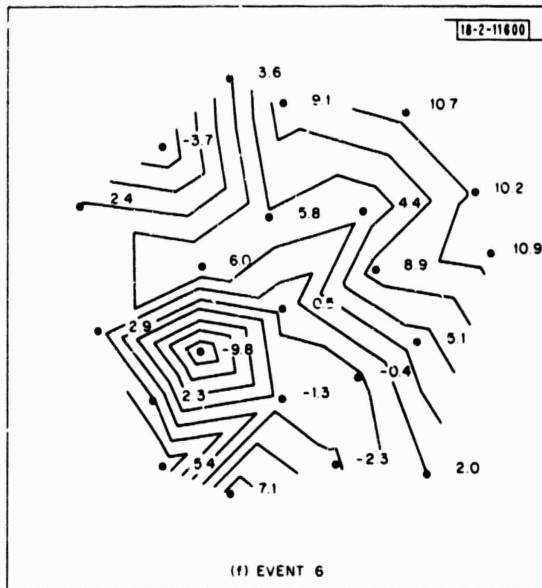
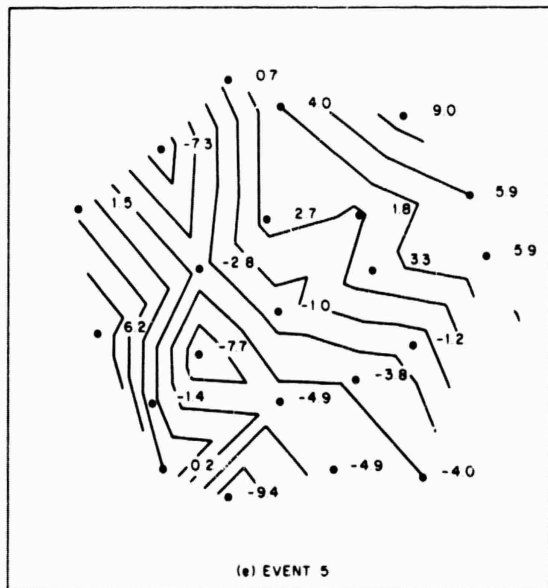


Fig. II-20(a-k). Continued.

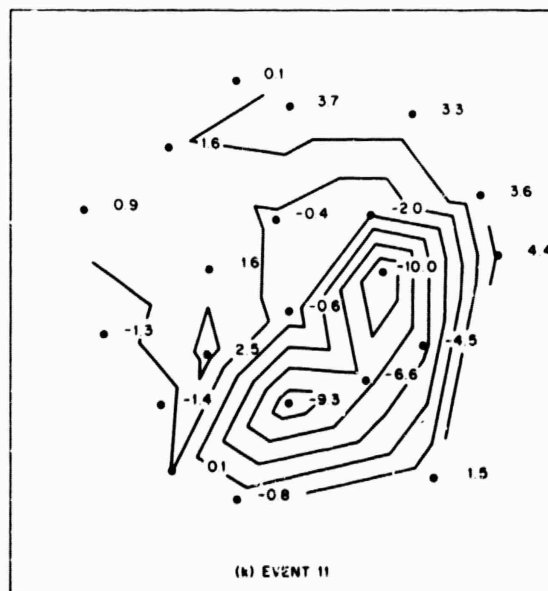
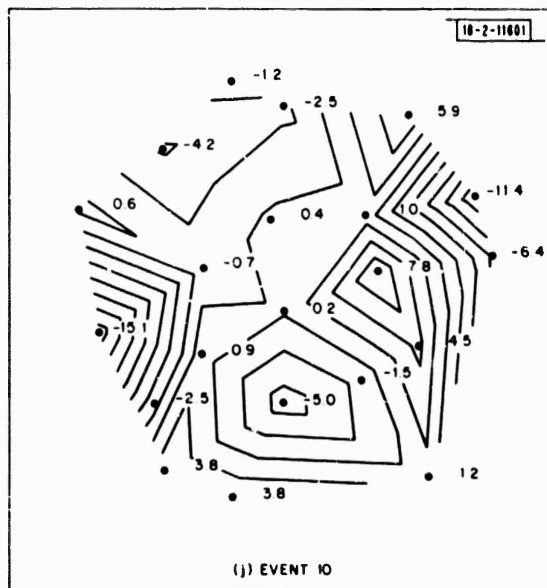
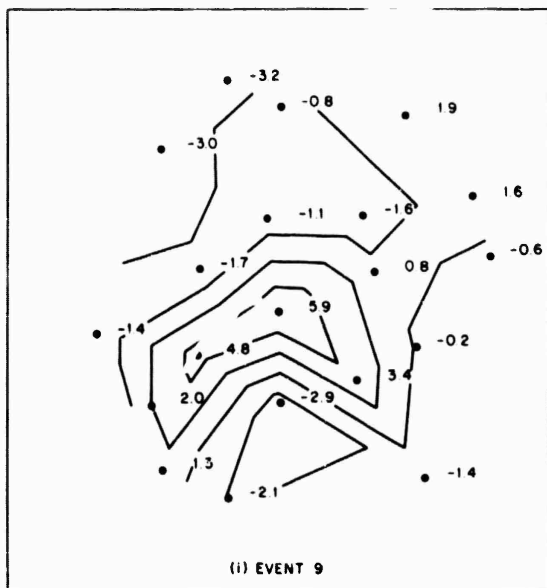


Fig. 11-20(a-k). Continued.

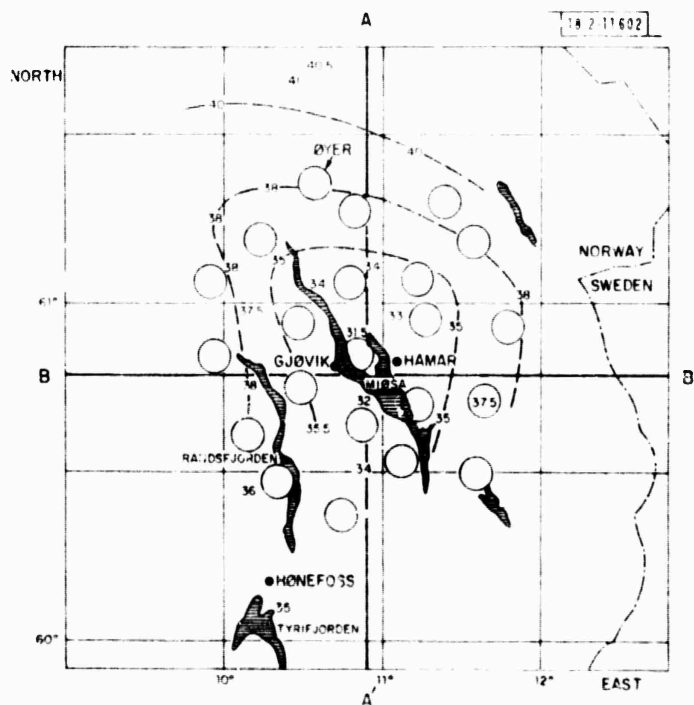


Fig. II-21. Depth to Mohorovicic discontinuity beneath NORSAR after Kanestrom.<sup>14</sup>

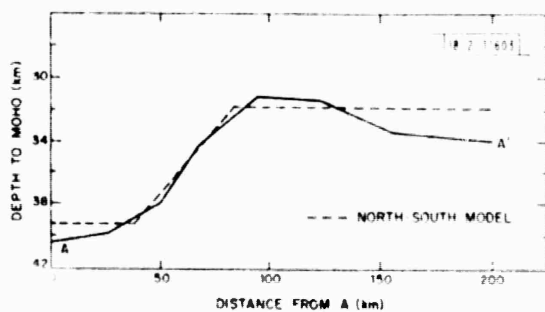


Fig. II-22. Cross section along A-A' and approximating step model.



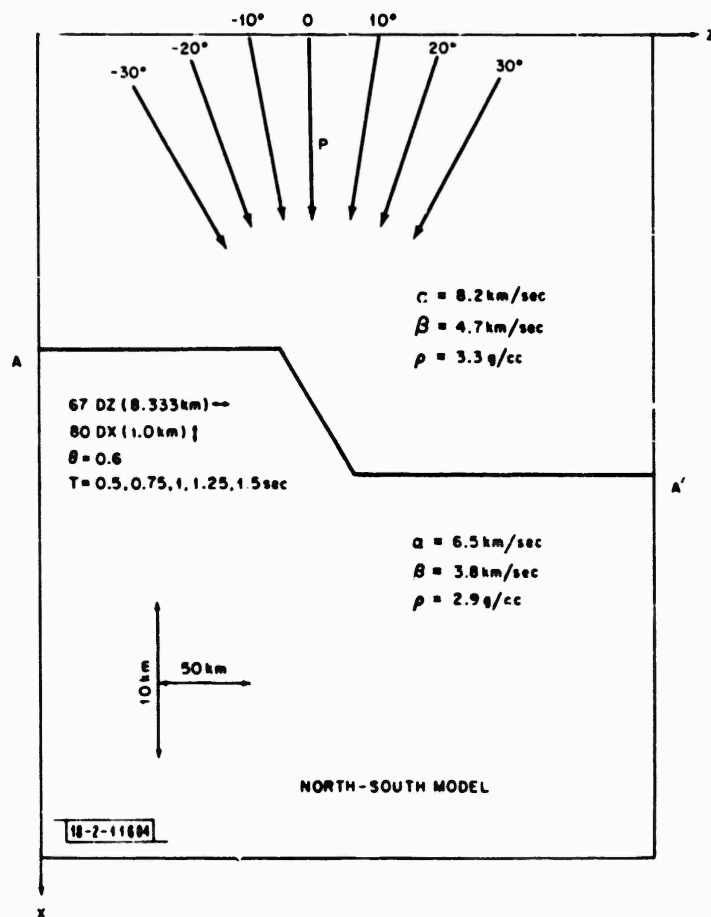


Fig. II-23. Velocities and initial conditions for which step-model solutions were generated.

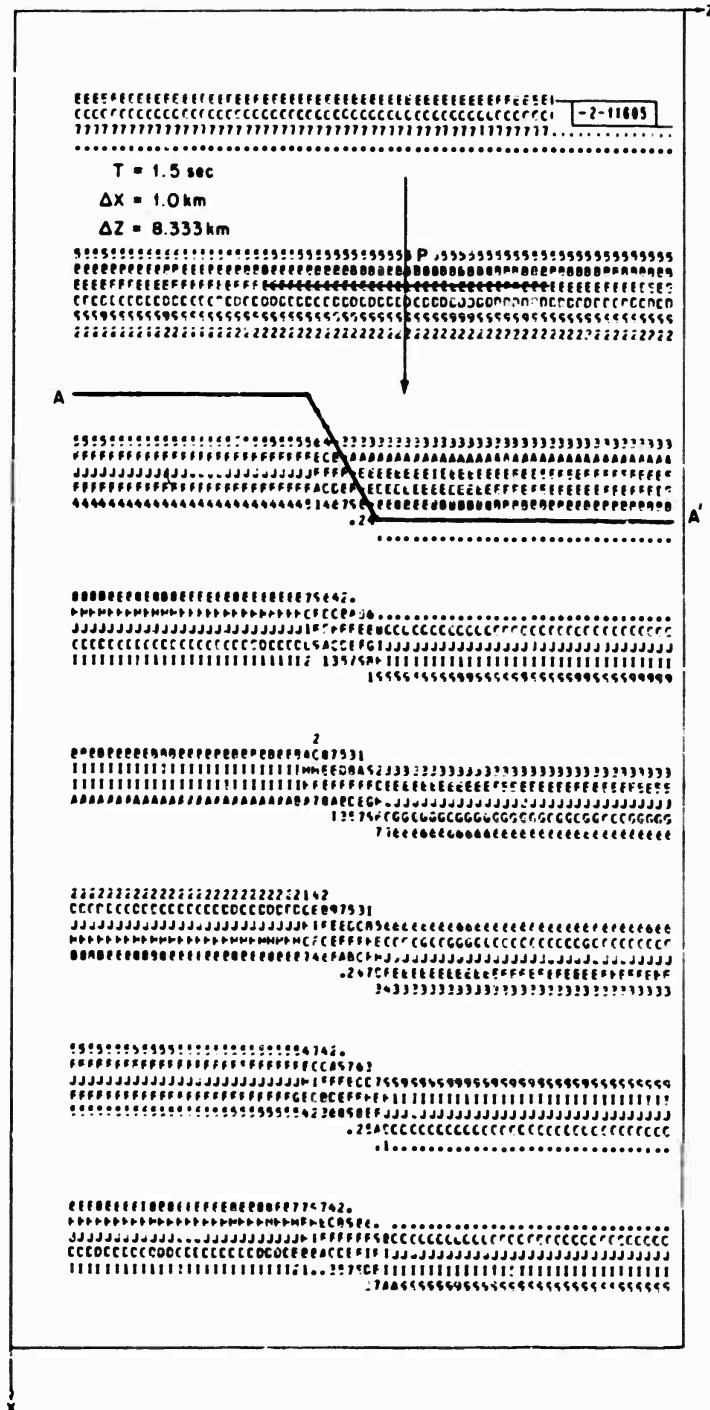


Fig. II-24. Equal-amplitude plot of solution for 1.5-sec period plane P-wave normally incident on North-South model.

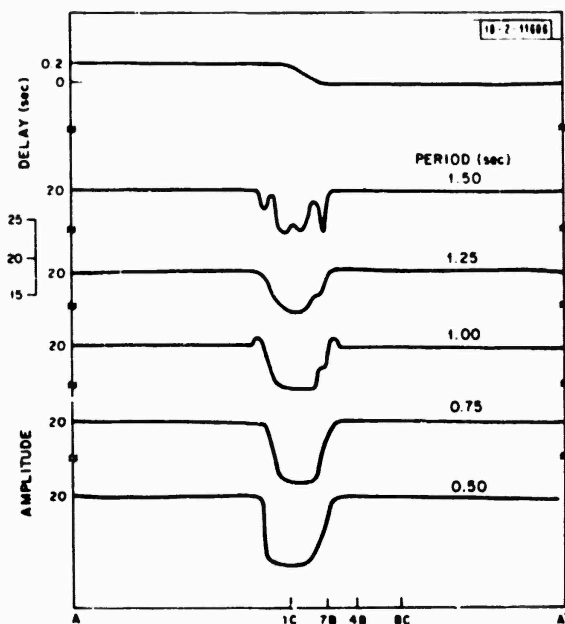


Fig. II-25. Amplitude and time-delay anomalies for step model for normal incidence at different periods.

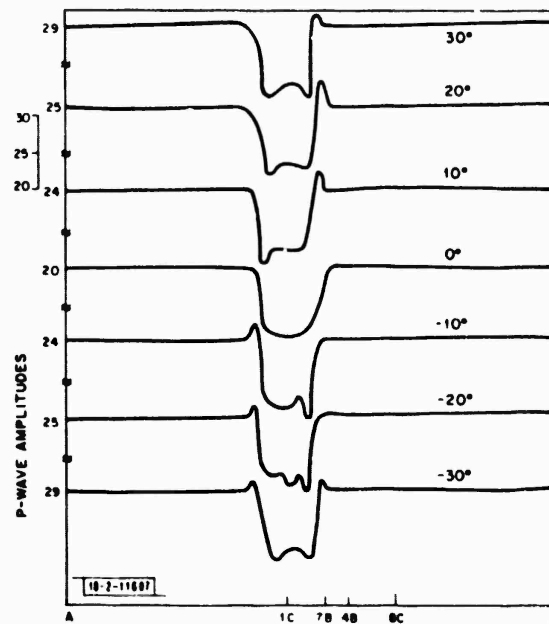


Fig. II-26. Amplitude anomalies for step model for 0.5-sec period P-waves at various angles of incidence.

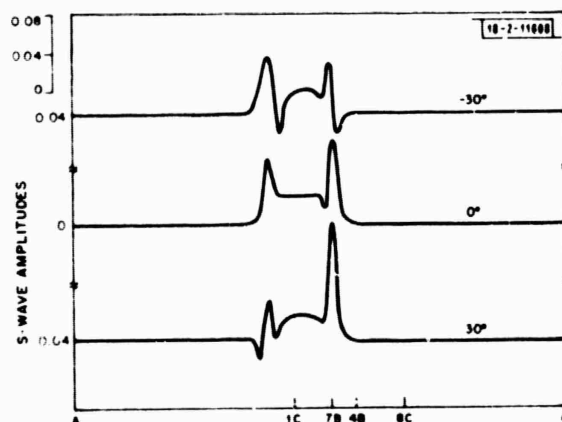


Fig. II-27. S-wave amplitudes for North-South model for P-waves incident at 0° and ±30°.

Fig. II-28. Cross section along B-B' and approximating anticline model.

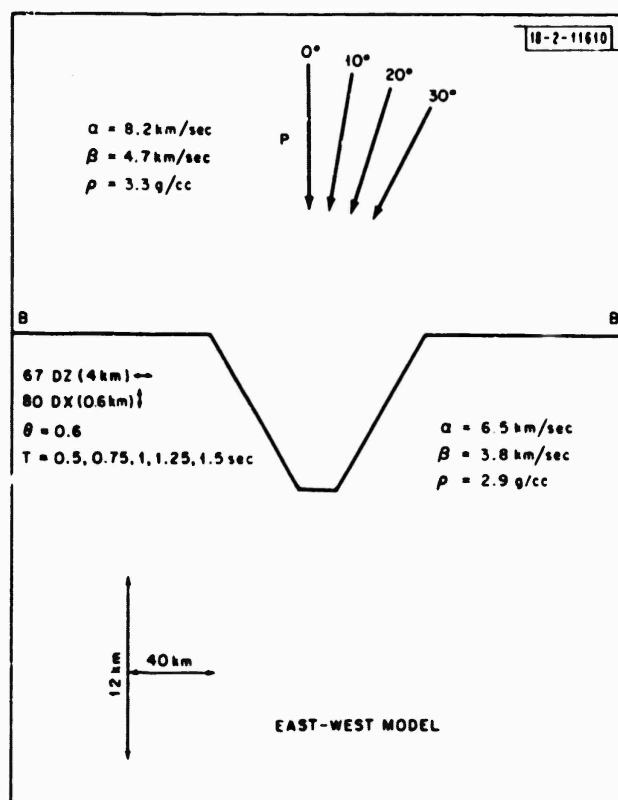
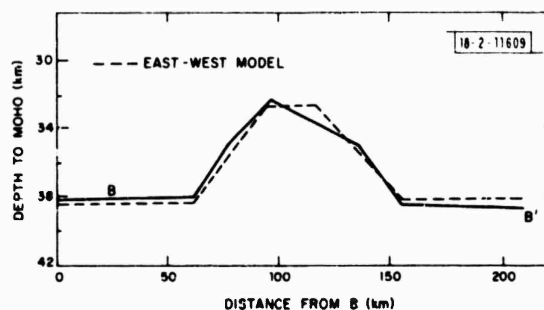


Fig. II-29. Velocities and initial conditions for which anticline model solutions were generated.

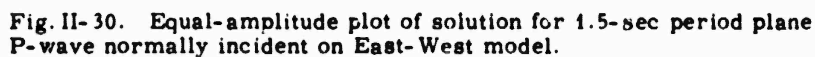


Fig. II-31. Amplitude and time-delay anomalies for anticline model for normally incident P-waves at various periods.

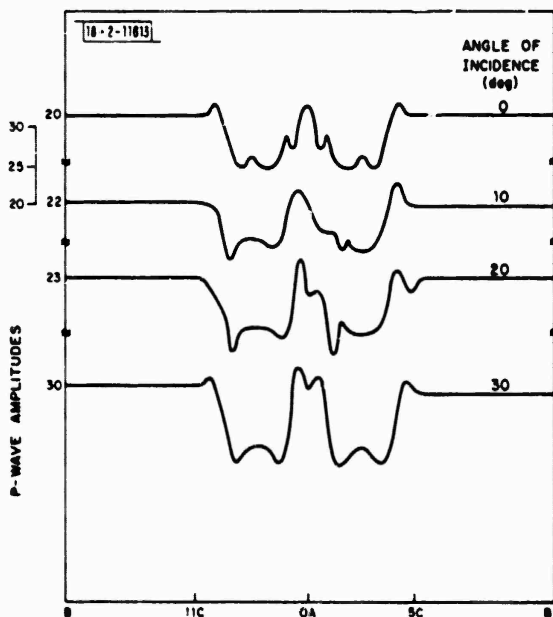
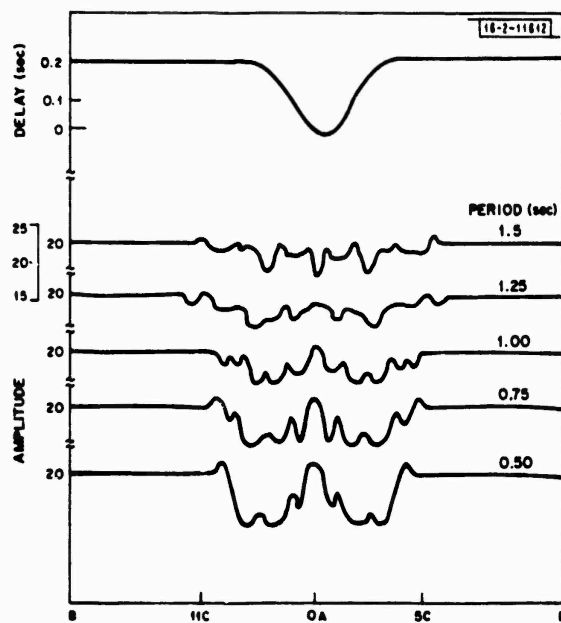


Fig. II-32. Amplitude anomalies for East-West model for 0.5-sec period P-waves at various angles of incidence.

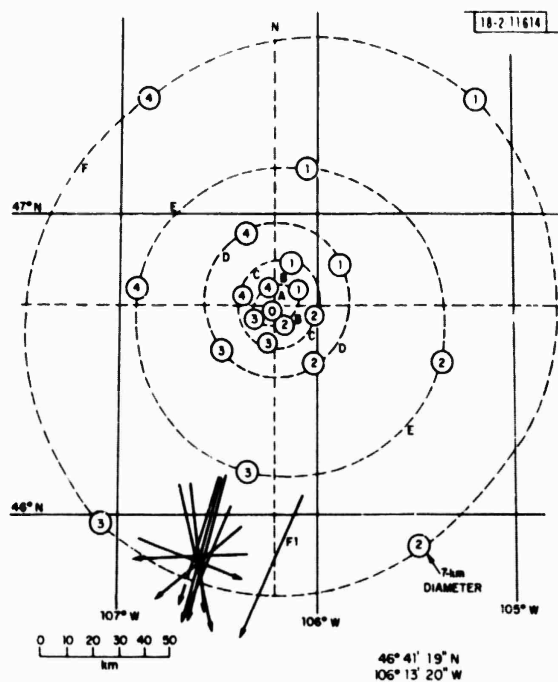


Fig. II- 33. Azimuths of first arrivals at E- and F-ring LASA subarrays for event in Table II-2.

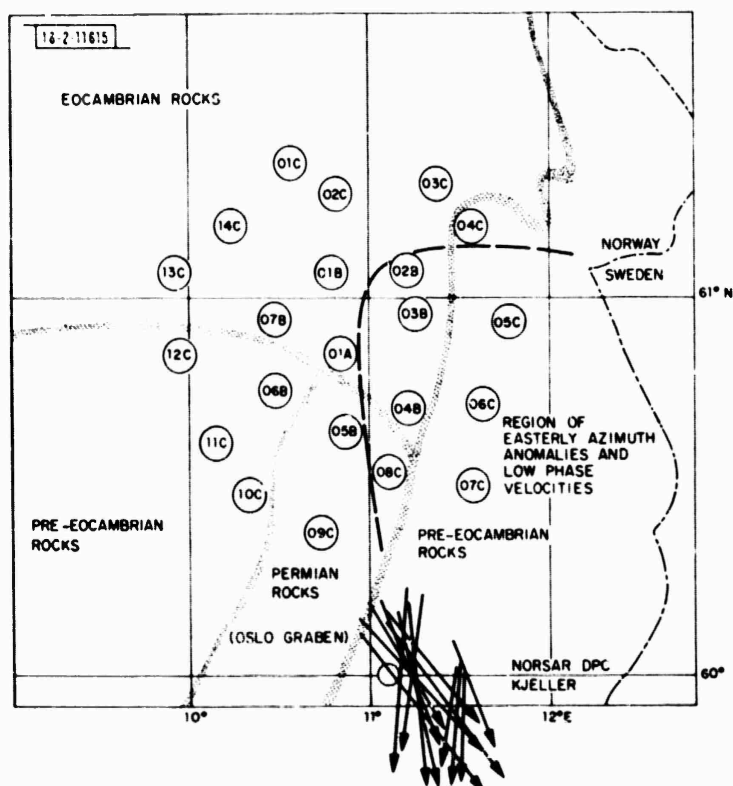


Fig. II- 34. Azimuths of first arrivals at C-ring NORSAR subarrays for event in Table II- 4.

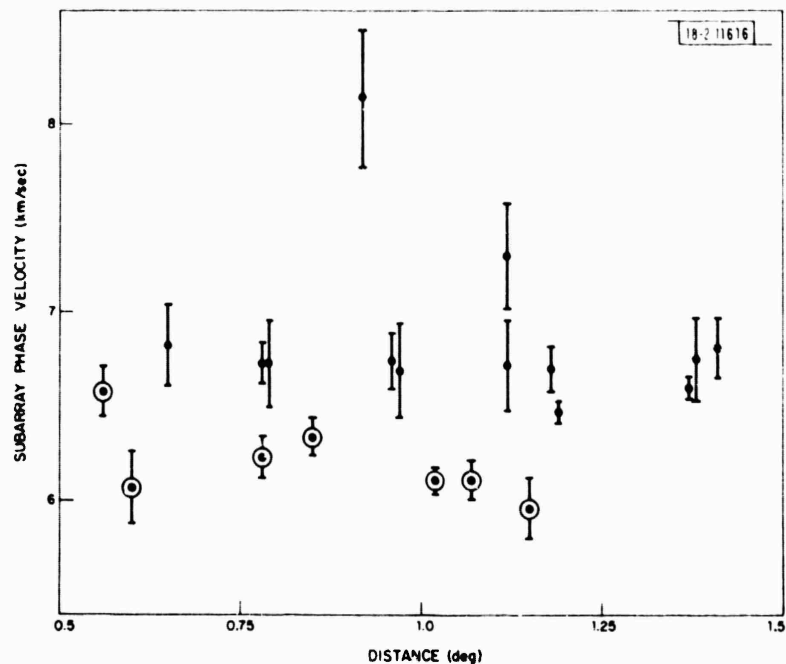


Fig. II-35. Subarray phase velocity with error bars of  $\pm\Delta C$  at NORSAR for event in Table II-4.

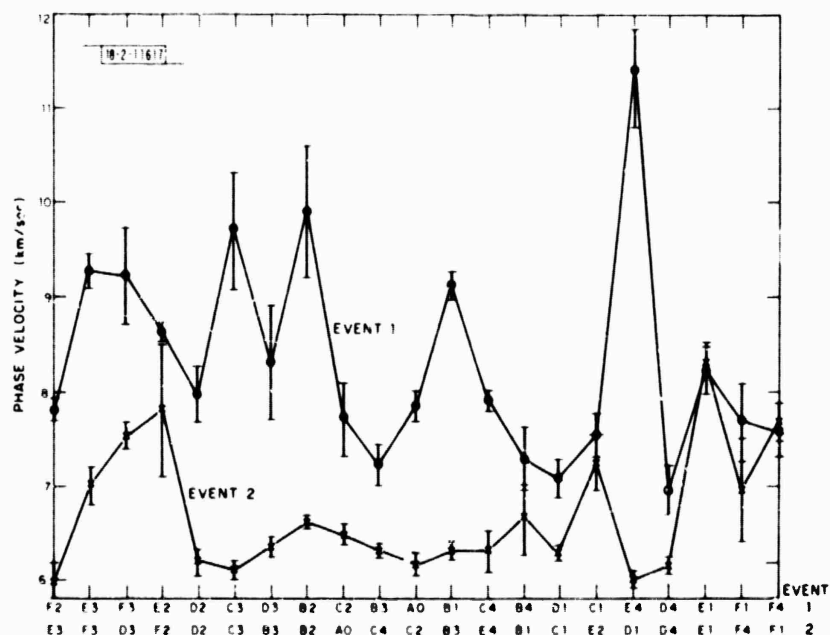


Fig. II-36. Subarray phase velocity with error bars of  $\pm\Delta C$  at LASA for events in Tables II-2 and II-3.



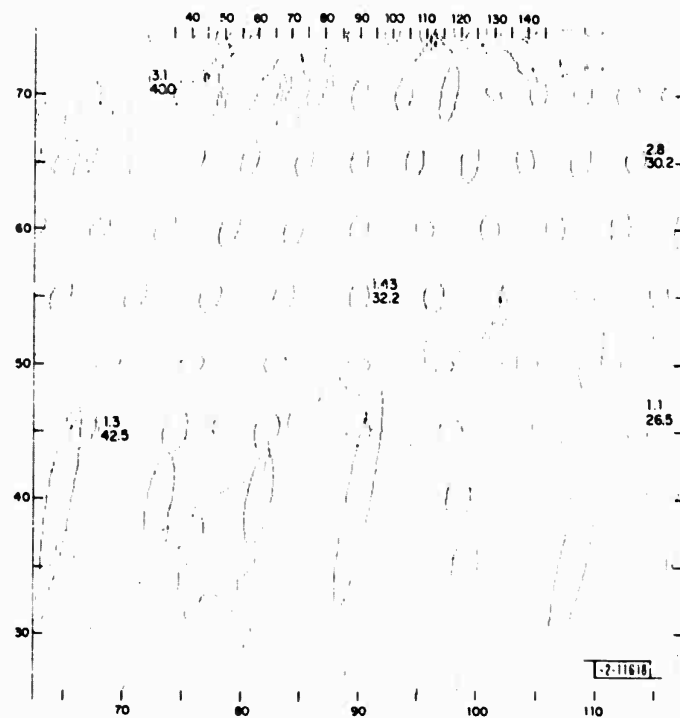


Fig. II-37. Theoretical 50-percent confidence ellipses for LASA, based on assumed resolution of 0.05 sec/deg. Numbers are, respectively, aspect ratios and areas (thousands of km<sup>2</sup>) of ellipses.

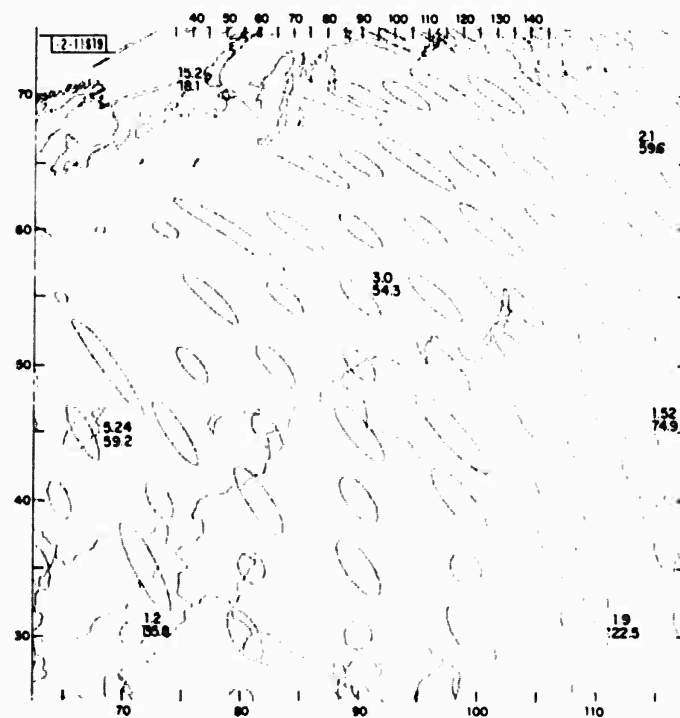


Fig. II-38. Theoretical 50-percent confidence ellipses of NORSAR, based on an assumed resolution of 0.1 sec/deg.

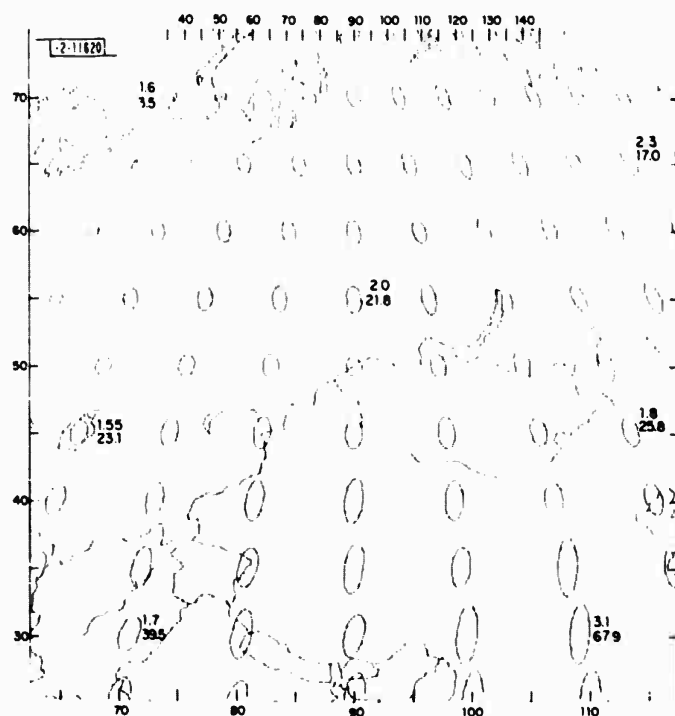


Fig. II-39. Same as Figs. II-37 and II-38, for LASA and NORSAR used together, with travel-time curve accurate to 1.5 sec.

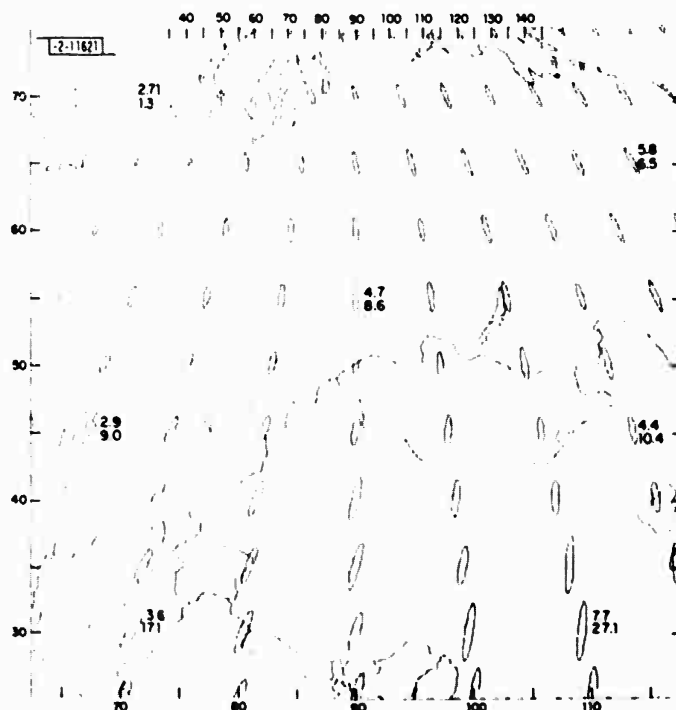


Fig. II-40. Same as Fig. II-39, with travel-time curve accurate to 0.5 sec.

### III. SEISMIC DISCRIMINATION

#### A. DETECTION OF INTERFERING RAYLEIGH WAVES AT NORSAR

It is well known that a powerful technique for discriminating between natural events and underground nuclear explosions is the  $M_s$ - $m_b$  method, based on the relationship between the surface-wave ( $M_s$ ) and the body-wave ( $m_b$ ) magnitude. Considerable effort has been expended on the problem of magnitude definitions, and especially on the definition of  $M_s$  yielding the best possible separation between earthquakes and underground explosions on an  $M_s$ - $m_b$  diagram, cf. Ref. 1. However, with the present deployment of seismic observatories and arrays, the main limitation of the method is quite often that no Rayleigh waves can be found for an event which is detected and located on the basis of short-period P-wave recordings. One of the reasons for this lack of a detection of surface waves is that their energy level may be below that of the ambient background microseismic noise. In this case the  $M_s$ - $m_b$  discriminant may still be employed, above a certain body-wave magnitude level, provided that discrimination can be based on negative evidence.

However, quite often there is a serious detection problem caused by the long persistence of Rayleigh-wave coda of other events, as pointed out by Capon and Evernden.<sup>2</sup> This situation is complicated by the fact that rapid lateral variations in phase velocity frequently cause severe multipath propagation problems, as pointed out by Capon.<sup>3</sup> The purpose of the present study was to investigate the amount and the characteristics of such multipath propagation for Rayleigh waves recorded at NORSAR, and to consider the problem of detecting one Rayleigh wave in the presence of the coda of another Rayleigh wave. The long-period (L.P) array at NORSAR consists of a three-component set of seismometers, located within each of the 22 subarrays, with peak response at about 25 sec. The aperture of NORSAR is approximately 110 km.

The main analysis technique used in this work was the high-resolution (HR) frequency-wavenumber spectrum analysis method described in detail by Capon.<sup>4</sup> The technique, which essentially reveals information about the distribution of power as a function of frequency and wavenumber, has been applied to successive nonoverlapping 200-sec intervals, at periods of 40 and 20 sec, starting at the onset time of the 40-sec-period Rayleigh-wave group. The analysis of such short time intervals would normally entail a serious windowing effect, causing energy from frequency bands other than those under analysis to affect the results, cf. Capon.<sup>3</sup> In order to avoid this, a prefiltering operation has been applied to the data before the HR analysis. The filter used in the 40-sec period analysis was a fifth-order Chebyshev low-pass filter with 3-dB response at 35 sec, while for the 20-sec analysis a third-order Butterworth bandpass filter was employed with 3-dB responses at 25 and 16.7 sec. Both filters are rolling off very sharply, thus virtually eliminating all problems connected with frequency windowing.

The HR method was applied to prefiltered data from the L.P vertical array at NORSAR for 15 events, each with  $m_b \geq 5.2$ , located at various azimuths and distances from NORSAR. There were no events occurring close in time to the chosen events, according to the USCGS monthly summary reports and the NORSAR bulletin.

The method proposed by Capon and Evernden<sup>2</sup> for the detection of interfering Rayleigh waves at LASA has been considered also for NORSAR. This method entails the application of the HR method to the prefiltered data from the L.P vertical array at LASA, to determine the angle of arrival of the fundamental-mode Rayleigh wave at the appropriate arrival time. If this angle and the arrival time are reasonably close to the expected values, then a detection is

said to occur. In order to evaluate the effectiveness of this detection method, it is necessary to measure the rate of decay of the Rayleigh-wave coda power level at NORSAR. These results are given in Figs. III-1(a) and III-2(a) for the 20- and 40-sec-period groups, respectively. The data in these figures were used to determine the minimum, average, and maximum detection thresholds for the detection method as a function of the arrival time of the surface waves of the sought event, and the results are given in Figs. III-1(b) and III-2(b) for the 20- and 40-sec-period groups, respectively. In obtaining these figures, detection thresholds of -12 and -6 dB below the coda power level were used, respectively, as determined experimentally for the 20- and 40-sec-period group Rayleigh waves at NORSAR.

It is seen from Figs. III-1(a) and III-2(a) that after about 7 minutes, the 40-sec-period group power has dropped about 8 dB more than that for the 20-sec period. These results should normally mean that by analyzing at a 40-sec rather than at a 20-sec period, the detection of the Rayleigh waves would not be obscured as often by an interfering event, provided there is equal signal energy at these two periods. Another argument that also favors the 40-sec-period group is the observation that there is more severe multipath propagation at 20 sec. On the other side, however, is the fact that the HR method performs better at 20 sec, due to the improved array response at this period. In addition the signal-to-interference ratio may actually be better at 20 sec, if there is enough signal energy to compensate for the increased amount of interfering event energy at this period, relative to 40 sec. A general conclusion as to which frequency to use therefore cannot be reached, and the detection at these two periods should be considered simultaneously.

The HR analysis of the 15 events provides information concerning the azimuthal deviation from the great circle path for all time frames in which the phase velocity measured can be reasonably associated with fundamental-mode Rayleigh waves. This acceptable range of phase velocities was 3.4-4.0 and 3.5-4.2 km/sec for 20- and 40-sec-period Rayleigh waves, respectively. These data concerning angles of arrival and group delays can be used to infer the actual propagation paths for the multipath propagation of Rayleigh waves, cf. Capon.<sup>3</sup> The results for the propagation paths, at both 20- and 40-sec periods, for the 7 December 1971 Bouvet Islands and 18 December 1972 Zambia events are shown in Figs. III-3(a) and (b) and III-4(a) and (b), respectively. These data seem to agree with the corresponding results for LASA given by Capon,<sup>3</sup> since it appears that in many cases the multipath propagation can be associated with refractions and reflections at continental margins, as well as scattering from small-scale tectonic regions of the earth.

It is now shown how the proposed detection method has been used at NORSAR to detect interfering Rayleigh waves. A number of independent sources reported that an atmospheric nuclear explosion occurred at the Lop Nor test site in China on 27 June 1973. This explosion has been identified by the USCGS, on the basis of seismic observations, as the 27 June 1973 Southern Sinkiang event, and has been used as a good example of the performance of the proposed detection method. The reason for this is that the event occurred during the time that an earthquake swarm was taking place in the Kurile Islands, Hokkaido region, and the expected arrival time for the explosion Rayleigh waves coincided exactly with the Rayleigh waves from one of the earthquakes in the swarm, namely the 27 June 1973 Hokkaido, Japan event. In addition, an event with epicentral parameters which were quite close to those for this interfering event, and which occurred about 30 minutes before it, was chosen as an ideal reference, namely the 27 June 1973 Kurile Islands event.

In accordance with the procedure outlined previously, both the 40- and 20-sec-period groups have been analyzed using the HR method, as applied to the prefiltered data. The results for the 40-sec-period group are shown in Fig. III-5(a-d) where the HR spectra from four consecutive 200-sec time intervals are depicted. The HR analysis was started about 3 minutes before the computed arrival time for the 40-sec-period Rayleigh-wave group for the desired event, i.e., the 27 June 1973 Southern Sinkiang event (Chinese Atmospheric Nuclear Explosion). The main 40-sec-period group arrives during the second time frame, depicted in Fig. III-5(b), and is also present in the third time frame, given in Fig. III-5(c), before it fades away. There is no multipath propagation observed in these two time frames, since the angle of arrival coincides almost precisely with the azimuthal direction toward the desired event. It can be concluded, therefore, that the 40-sec-period Rayleigh-wave group of the desired event has been detected, since it has been shown to arrive at NORSAR at the appropriate time and with the expected angle of arrival.

The situation for the 20-sec-period group is much more complicated. The results of the HR analysis for the reference event, and for the desired plus interfering events, are shown in Figs. III-6(a-d) and III-7(a-d), respectively, and the two figures should be studied simultaneously. The HR analyses given in Figs. III-6 and III-7 are started at the expected onset times of the 20-sec-period group of the reference and interfering events, respectively. In Figs. III-6(a) and III-7(a), the angle of arrival agrees well with the azimuth of both the reference and interfering events, namely about  $33^\circ$ . The second frame, given in Figs. III-6(b) and III-7(b), shows that the angle of arrival decreases to about  $18^\circ$  for both events, possibly indicating a reflection somewhere in northern Siberia, and the surface waves for the explosion are not seen as yet. In Fig. III-6(c) there is an additional multipath arrival (at about  $45^\circ$ ) for the reference event, while in Fig. III-7(c) the main energy now arrives at an azimuth corresponding to the direction toward Lop Nor. Since this time agrees well with the expected arrival time for the 20-sec-period Rayleigh-wave group of the desired event, the detection of the surface waves for this event has been firmly established. The results in Fig. III-7(d) indicate some energy which is probably due to the desired event, while the data in Fig. III-6(d) show only some weak multipath component.

In this case, the detection of the Rayleigh wave of the desired event in the coda of an interfering event has been accomplished at both 20 and 40 sec. However, it is clear that the detection at a 40-sec period, at least in this example, was much clearer than that at a 20-sec period.

J. Capon  
H. Bungum

## B. PRECURSORS TO pP FROM DEEP SOUTH AMERICAN EARTHQUAKES

Occasionally, when processing the early short-period arrivals from deep South American earthquakes, automatic detection schemes used by the large arrays do not correctly identify the pP depth phase. These schemes interpret an intermediate phase between P and pP as pP, and identify the true pP as a second event from the same region. If these intermediate phases are of a deterministic origin, there are two plausible explanations for that origin. Either they are the P-waves from small earthquakes which follow the larger deep events, or they are reflections off some boundary between the focus of a single earthquake and the surface of the earth above the focus. We tend to reject the suggestion that these phases are due to reflections from contrasts beneath the recording station since, in that case, these phases would be generally observed independent of the geographic region or depth of the source. We shall attempt to

interpret these intermediate phases between  $P$  and  $pP$  as reflections from a physical contrast above the deep sources and, following Whitcomb and Anderson,<sup>5</sup> introduce the nomenclature  $pdP$  where  $d$  is the depth beneath the surface of that contrast.

Figure III-8(a) shows the short-period subarray sums of the three outer rings of LASA and the initial arrivals from an earthquake located 537 km beneath northern Argentina. As indicated on the figure, there is a relatively small yet clear and coherent arrival across the entire array about midway between  $P$  and  $pP$ . Figure III-8(b) is similar to III-8(a), showing array traces for an earthquake about 800 km south of that in III-8(a) at a depth of about 580 km. Here, although the phase midway between  $P$  and  $pP$  exists, it is not as clear as the previous example. However, there is a larger, intermediate secondary arrival about 30 sec before  $pP$  in this case. In order to verify the existence of these phases, we have searched the short-period vertical seismograms of the World Wide Standard Seismographic Network (WWSSN) of the two events in Figs. III-8(a) and (b) and four additional deep earthquakes ( $H > 500$  km) under northwestern Argentina. Although these intermediate phases cannot be read from single station seismograms as confidently as they can from array data, we have attempted to time an arrival within 30 sec before  $pP$  and the largest arrival between  $P$  and  $pP$ , yet not part of the  $P$  coda. Care was taken to exclude  $PcP$  from the study.

The results of these readings are shown in Fig. III-9 where the time differences  $pP-pdP$  of the largest phase (open circles) and phases within 30 sec of  $pP$  (black dots) are plotted vs epicentral distance. The solid lines show how these time differences should vary with distance given horizontal reflectors at various depths  $d$  above the source. From Fig. III-9, the strongest  $pdP$  phase would appear to come from a boundary between 200 and 300 km, say 250 km. The solid dots scatter about the 100-km depth line (they were picked to do so) and do not show evidence of any well-defined horizontal reflector at that depth. The location of the earthquakes used extends south along longitude  $63^\circ W$  from  $22^\circ S$  to  $28^\circ S$  and is associated with a rather complicated tectonic system which is probably not well-represented by plane, horizontal boundaries. These qualifications may account for some of the scatter observed in Fig. III-9.

There is one interesting correlation that can be drawn between the phase  $p250P$  and the regional seismicity pattern. In Fig. III-10, we have projected all the earthquakes of  $m_b > 5.0$  that occurred from 1967 to 1970 between  $20^\circ S$  and  $30^\circ S$  and  $62^\circ W$  and  $74^\circ W$  onto a plane of constant latitude. This cross section shows the well-known west-east dip of Andean seismicity and the gap in this activity between 300- and 500-km depth. It is well-established that this general seismicity pattern is associated with the plunging of the oceanic Nazca plate beneath the South American continent. Isacks and Molnar<sup>6</sup> have discussed seismicity gaps as seen in Fig. III-10 in terms of physical gaps in the descending lithosphere, and as representing stress changes in the slab from extension to compression as a function of depth. The data of Figs. III-8 and III-9 indicate that a reflecting boundary may exist under western South America at a depth that coincides with the beginning of the large gap in a rather narrow seismicity zone. Since this boundary must be rather widespread in order to reflect waves from earthquakes 800 km apart, its existence might indicate that cause of the strikingly discontinuous seismicity zone is not of the descending plate itself but of the mantle into which it intrudes.

J. R. Filson  
M. T. Lin

### C. COMPARISON OF pP-P DELAY TIMES FROM SURFACE-ZERO AND TELESEISMIC RECORDS OF NUCLEAR EXPLOSIONS

Many attempts<sup>7-11</sup> have been made to estimate the pP-P delay times for nuclear explosions using teleseismic short-period seismograms, and from these delay times to estimate depth of burial. One technique is to look for repeating nulls in the spectrum of the P-wave train and interpret them as a destructive interference between P and pP phases.<sup>7,8</sup> Another method is to deconvolve the combined effect of seismometer and earth attenuation from the seismogram in the time domain, and obtain the pP-P delays by inspection of the deconvolved records.<sup>9,10</sup> Recently, homomorphic deconvolution has been utilized to extract pP, P, and P<sub>s</sub> (spall) arrival times and amplitudes for the explosions.<sup>11</sup>

Due to unknown complexities of both the source environment and transmission path from explosion to receiver, there has always been a possibility that the analyses have not really extracted pP information, but rather some other seismic phenomenon. In fact, many earthquakes show interference effects in the first second or two of the P-wave train which cannot be due to a pP phase yet are very similar to those seen on explosion seismograms.

A crucial set of data for settling this question has been tabulated by D. L. Springer.<sup>12</sup> He has listed the pP-P and P<sub>s</sub>-P delay times for thirty-seven U.S. nuclear explosions obtained from accelerograms recorded on the surface over the explosions. One-way transit times for the explosion to the free surface were essentially doubled and corrected for passage through the fractured overburden section to obtain pP-P times expected at teleseismic distances. Springer tabulates nine of the explosions which have associated pP-P delay times determined from teleseismic seismograms by the methods described above. These data are plotted in Fig. III-11. Also included is an additional set of seven pP-P delay times obtained from digital data at NORSAR by this author.<sup>10</sup> The origin times, depths, epicentral coordinates, and available yield information for these explosions are given by Springer and Kinnaman.<sup>13</sup>

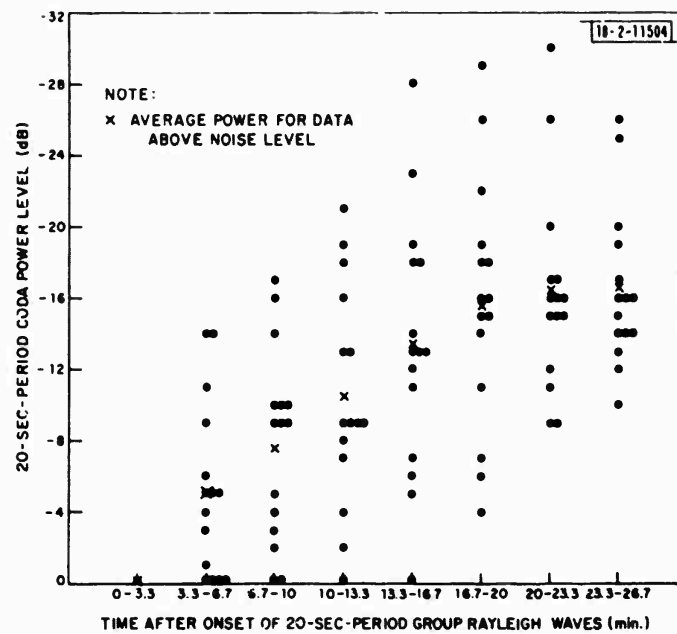
In Fig. III-11, the teleseismic pP-P delay times for six explosions were obtained by more than one worker using different data. Delay times for the same explosion are connected by vertical lines except for the two points for BOXCAR which are bracketed. With the exception of PILE DRIVER, most explosions in Fig. III-11 show good agreement between the surface-zero delay times and the teleseismic delay times, independent of the type of analysis used on the teleseismic data. Generally, the teleseismic delays are slightly larger than the surface-zero delay times. This may be due to the lack of resolution in time of the teleseismic data, or perhaps underestimating the decrease in P-wave velocity of the fractured overburden section.

C. W. Frasier

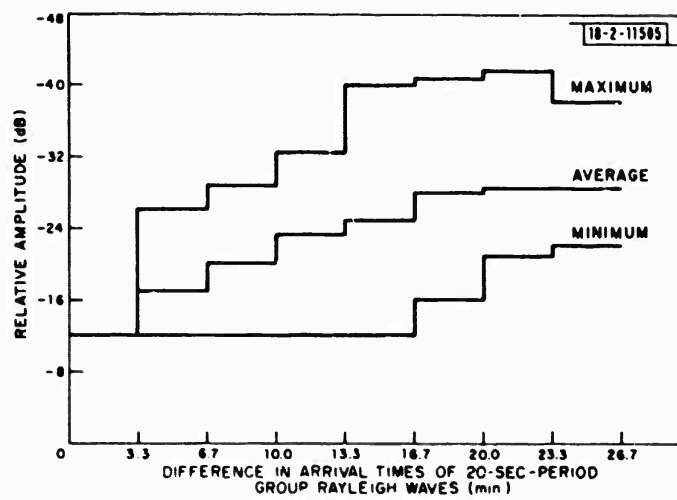
## REFERENCES

1. P. D. Marshall and P. W. Basham, "Discrimination Between Earthquakes and Underground Explosions Employing an Improved  $M_s$  Scale," *Geophys. J. R. Astr. Soc.* 28, 431-458 (1972).
2. J. Capon and J. F. Evernden, "Detection of Interfering Rayleigh Waves at LASA," *Bull. Seismol. Soc. Am.* 61, 807-849 (1971), DDC AD-734105.
3. J. Capon, "Analysis of Rayleigh-Wave Multipath Propagation at LASA," *Bull. Seismol. Soc. Am.* 60, 1701-1731 (1970), DDC AD-716084.
4. J. Capon, "High-Resolution Frequency-Wavenumber Spectrum Analysis," *Proc. IEEE* 57, 1408-1418 (1969), DDC AD-696880.
5. J. H. Whitcomb and D. L. Anderson, "Reflection of P'P' Seismic Waves from Discontinuities in the Mantle," *J. Geophys. Res.* 75, 5713-5727 (1970).
6. B. Isacks and P. Molnar, "Distribution of Stresses in the Descending Lithosphere from a Global Survey of Focal-Mechanism Solutions of Mantle Earthquakes," *Rev. Geophys. Space Phys.* 9, 103-172 (1971).
7. T. J. Cohen, "Determination of Source Depth by Spectral, Pseudo-Autocovariance and Cepstral Analysis," SOL Report 229, Teledyne, Inc., Alexandria, Virginia (1969).
8. O. Kuhanek, "P Wave Amplitude Spectra of Nevada Underground Nuclear Explosions," *Pure Appl. Geophys.* 88, 121-136 (1971).
9. P. D. Marshall, "Some Seismic Results from a World Wide Sample of Large Underground Explosions," AWRE Report 049/72, United Kingdom Atomic Energy Authority (1972).
10. C. W. Frasier, "Observations of pP in the Short Period Phases of NTS Explosions Recorded at Norway," *Geophys. J. R. Astr. Soc.* 31, 99-110 (1972).
11. W. H. Bakun and L. R. Johnson, "The Deconvolution of Teleseismic P-Waves from Explosions MILROW and CANNIKIN," *Geophys. J. R. Astr. Soc.* (in press).
12. D. L. Springer, "Secondary Sources of Seismic Waves from Underground Nuclear Explosions (submitted to *Bull. Seismol. Soc. Am.*).
13. D. L. Springer and R. L. Kinnaman, "Seismic Source Summary for U.S. Underground Nuclear Explosions, 1961-1970," *Bull. Seismol. Soc. Am.* 61, 1073-1098 (1971).



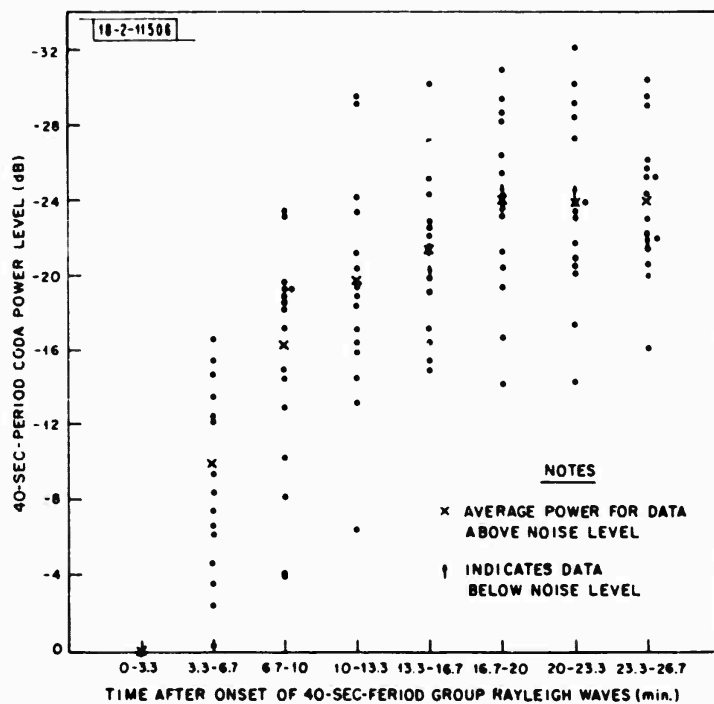


(a)

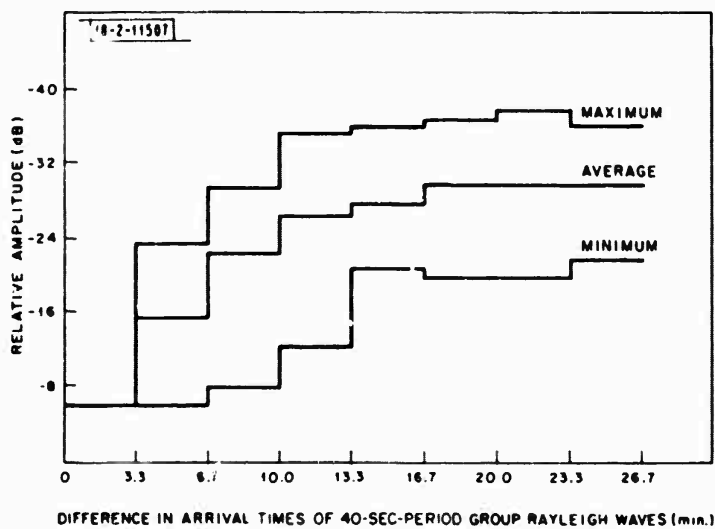


(b)

Fig. III-1(a-b). Rate of decay of coda power level and performance characteristic of proposed detection method at 20-sec period.



(a)



(b)

Fig. III-2(a-b). Rate of decay of coda power level and performance characteristic of proposed detection method at 40-sec period.

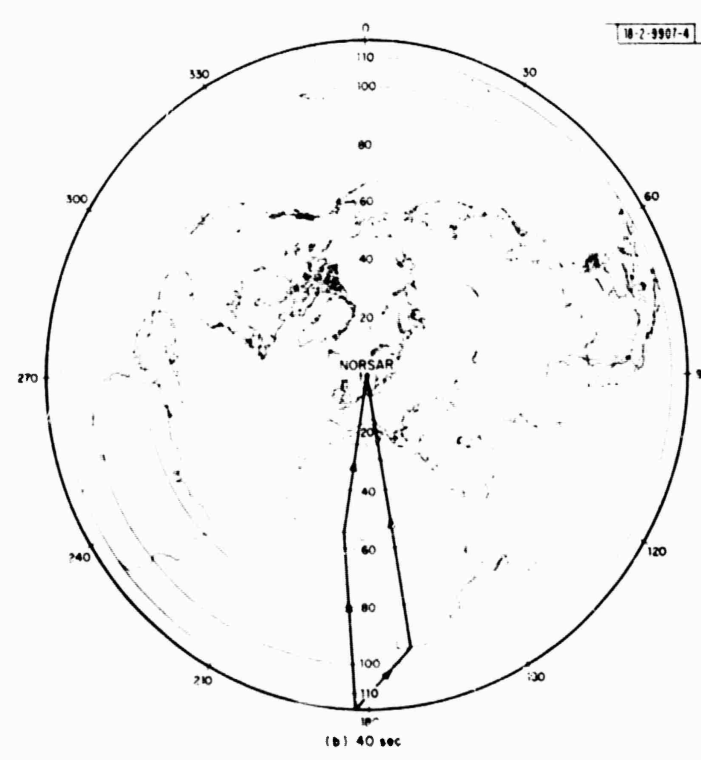
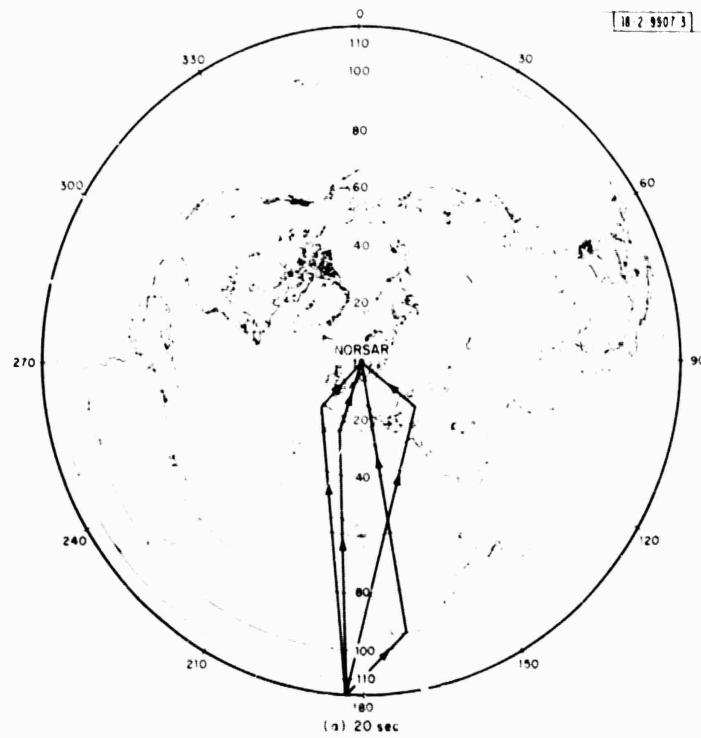


Fig. III-3(a-b). Propagation paths for 20- and 40-sec-period Rayleigh-wave groups for 7 December 1971 Bouvet Islands event.

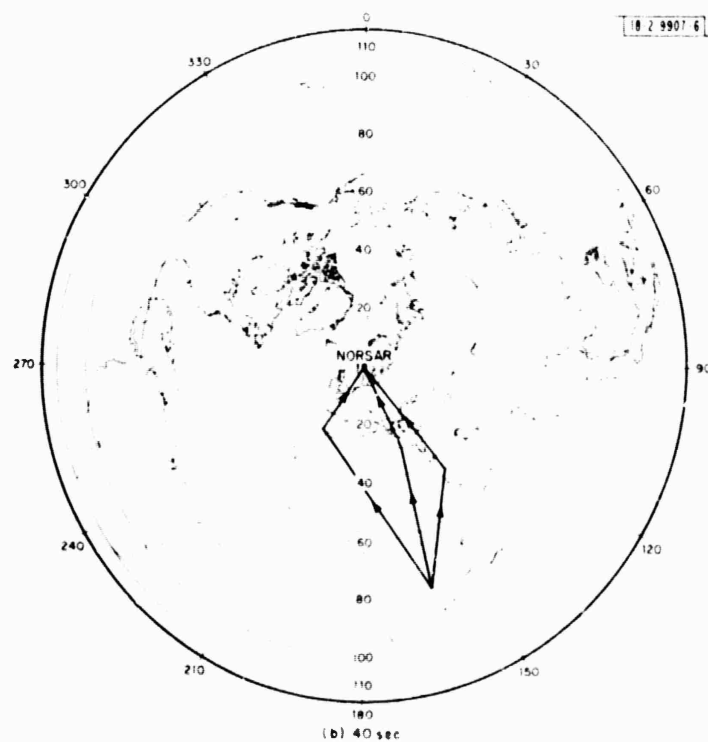
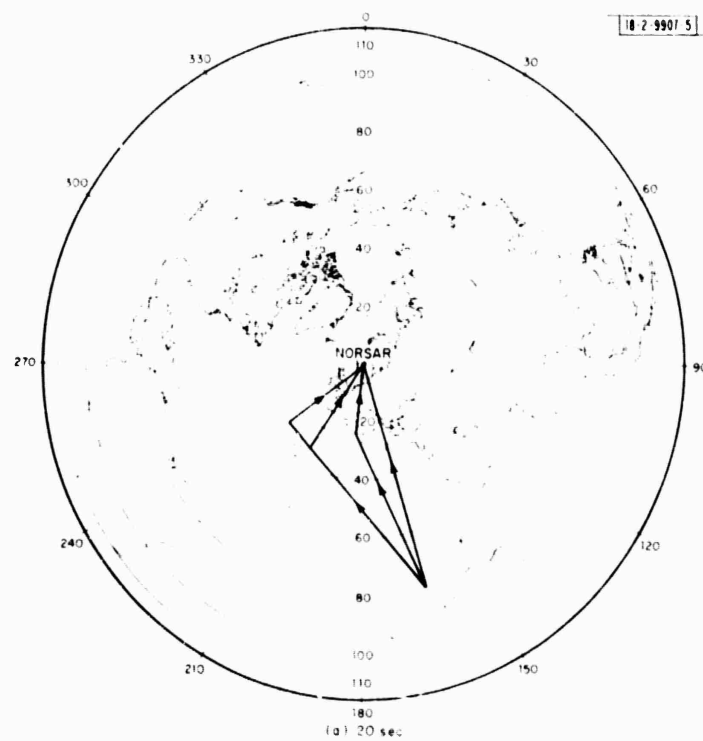


Fig. III-4(a-b). Propagation paths for 20- and 40-sec-period Rayleigh-wave groups for 18 December 1972 Zambia event.

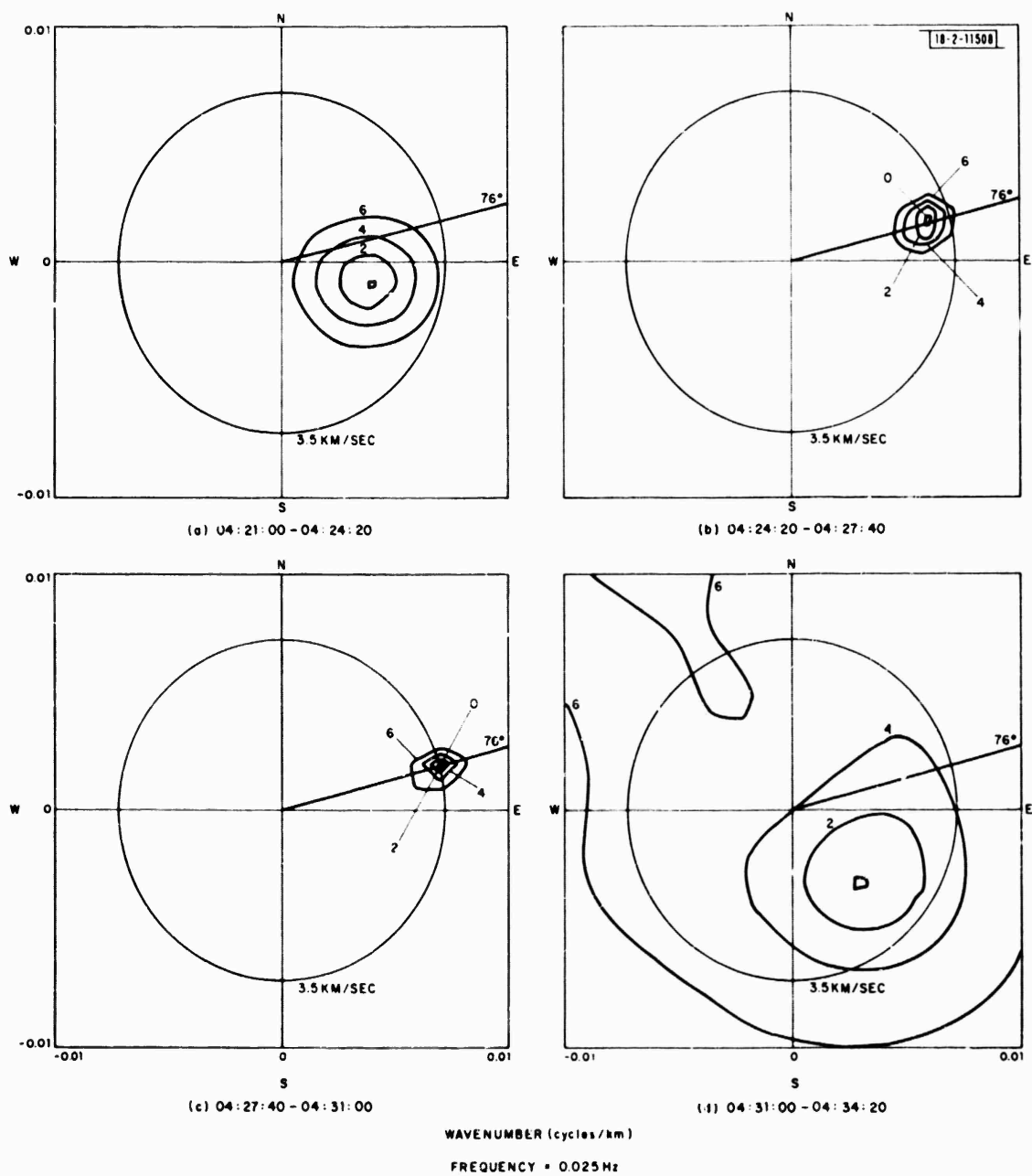


Fig. III-5(a-d). High-resolution frequency-wavenumber spectra, at 40-sec period, for prefiltered waveforms of 27 June 1973 Southern Sinkiang and Hokkaido, Japan events.

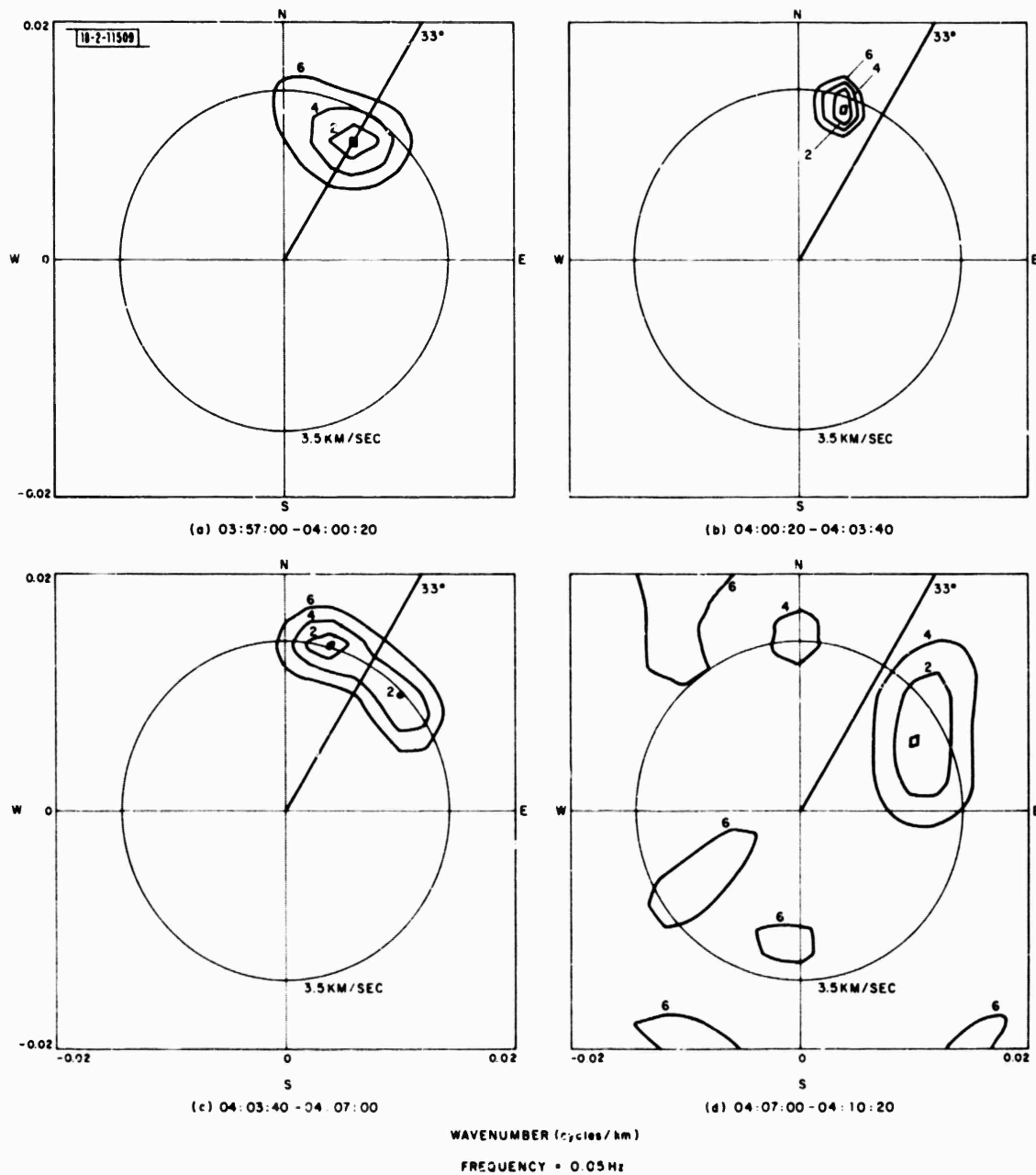


Fig. III-6(a-d). High-resolution frequency-wavenumber spectra, at 20-sec period, for prefiltered waveforms of 27 June 1973 Kurile Islands event.

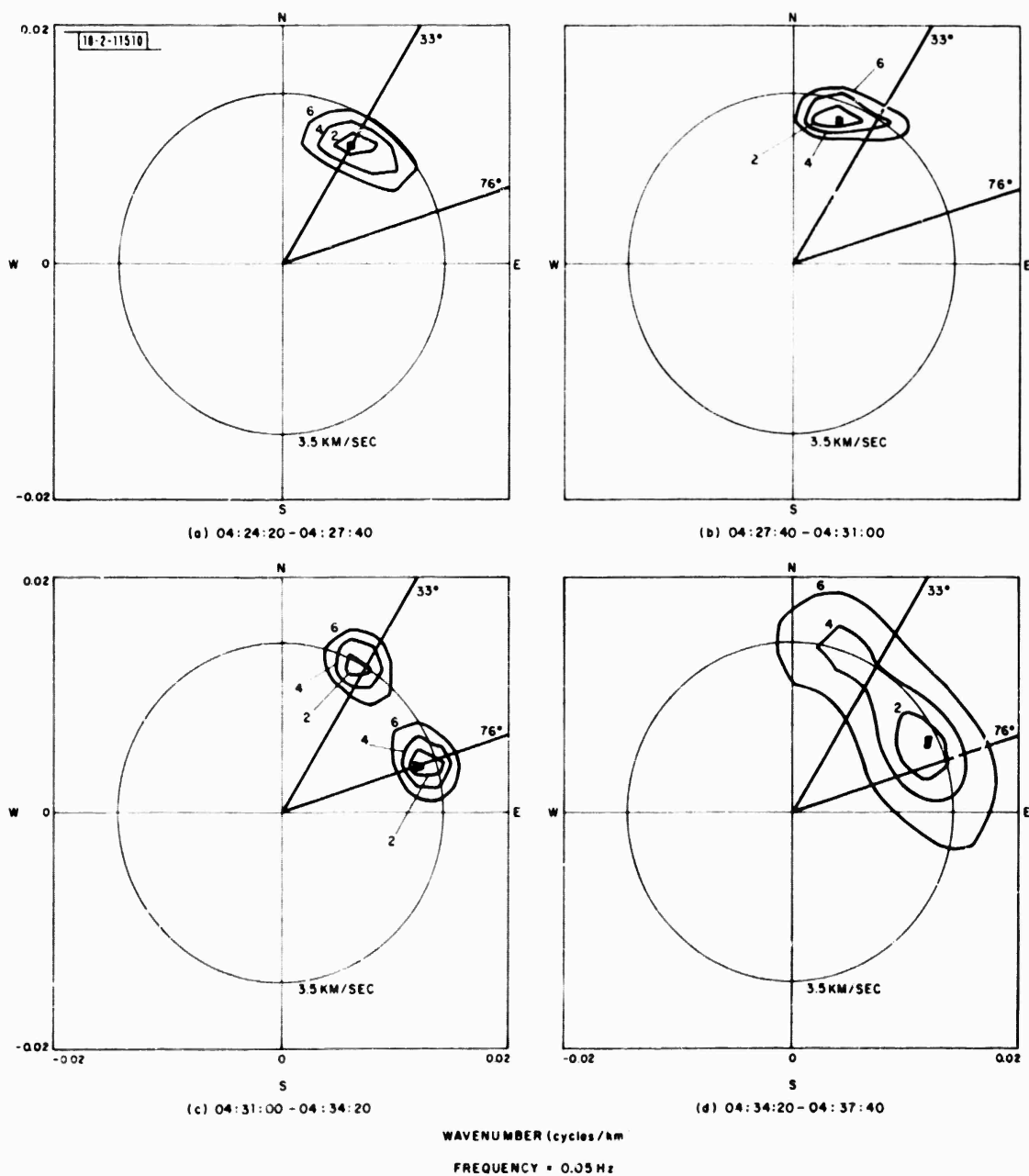


Fig. III-7(a-d). High-resolution frequency-wavenumber spectra, at 20-sec period, for prefiltered waveforms of 27 June 1973 Southern Sinkiang and Hokkaido, Japan events.

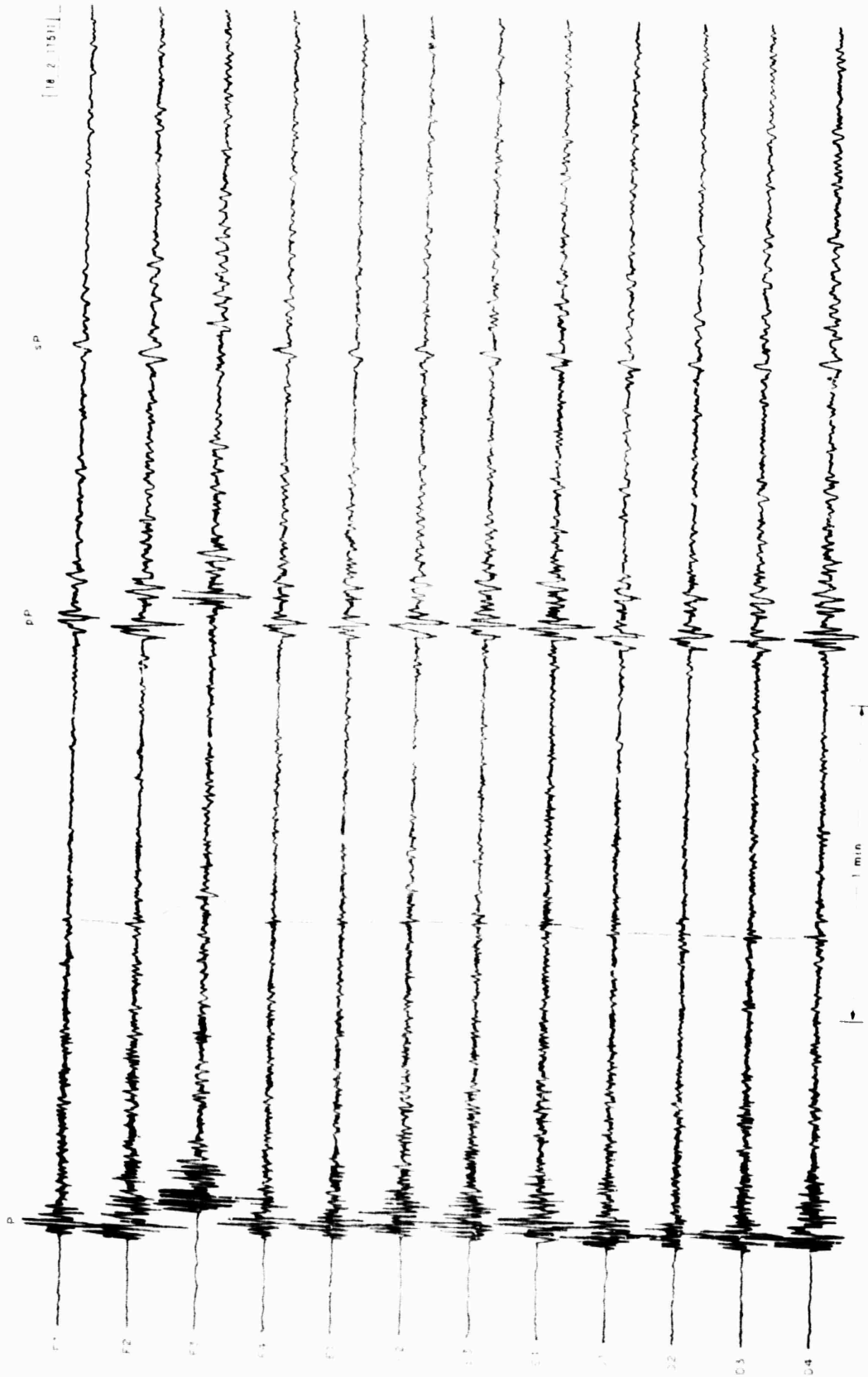


Fig. III-8(a). Short-period, subarray sums from D, E, and F rings of LASA showing initial arrivals from earthquake occurring on 23 August 1968 at 22h 36m 51s, 537 km deep beneath 22.0°S and 63.5°W.



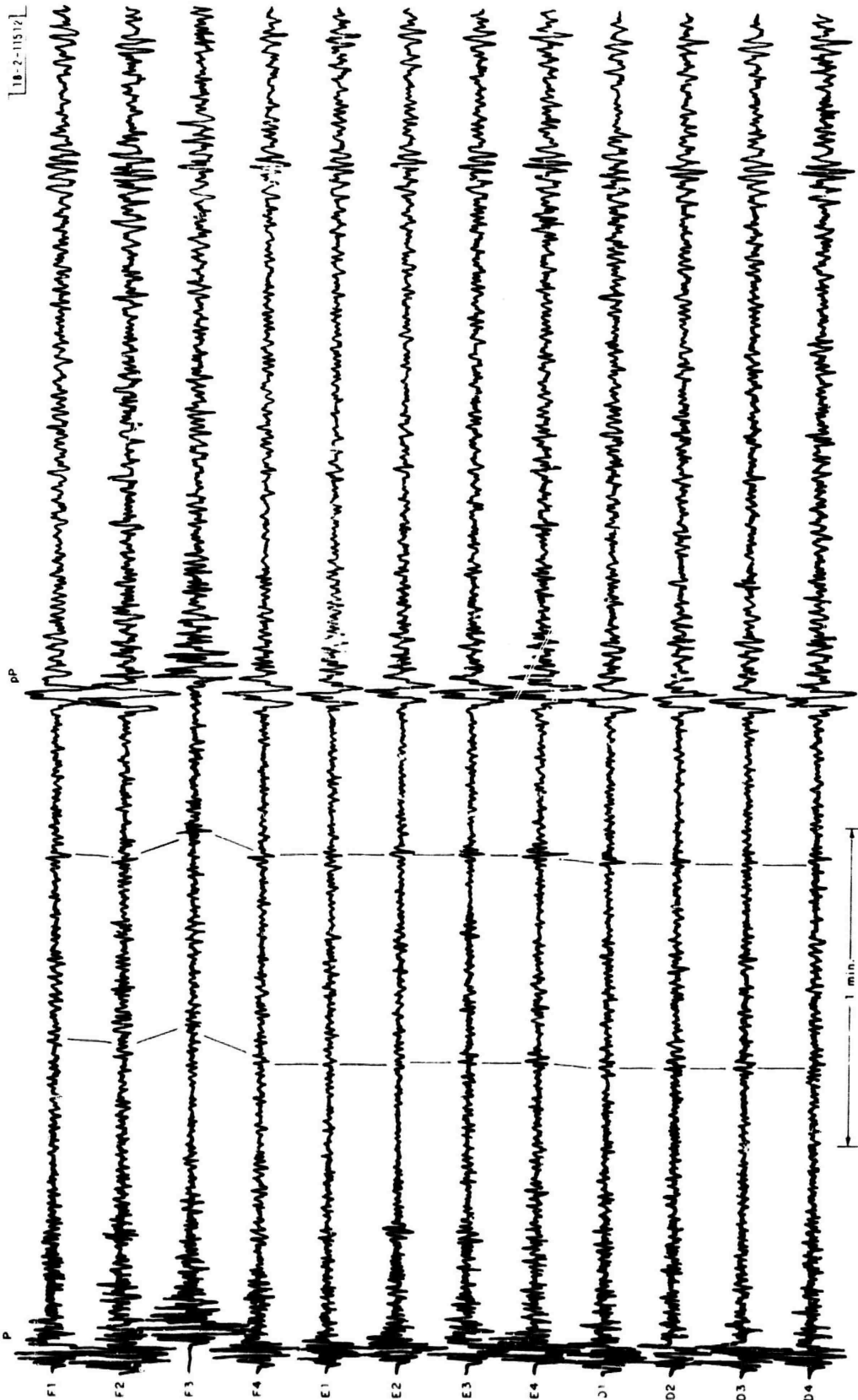


Fig. III-8(b). Similar data as in Fig. III-8(a) from earthquake occurring on 9 September 1967 at 10h 18m 14s, 578 km deep beneath 27.7°S and 63.1°W.

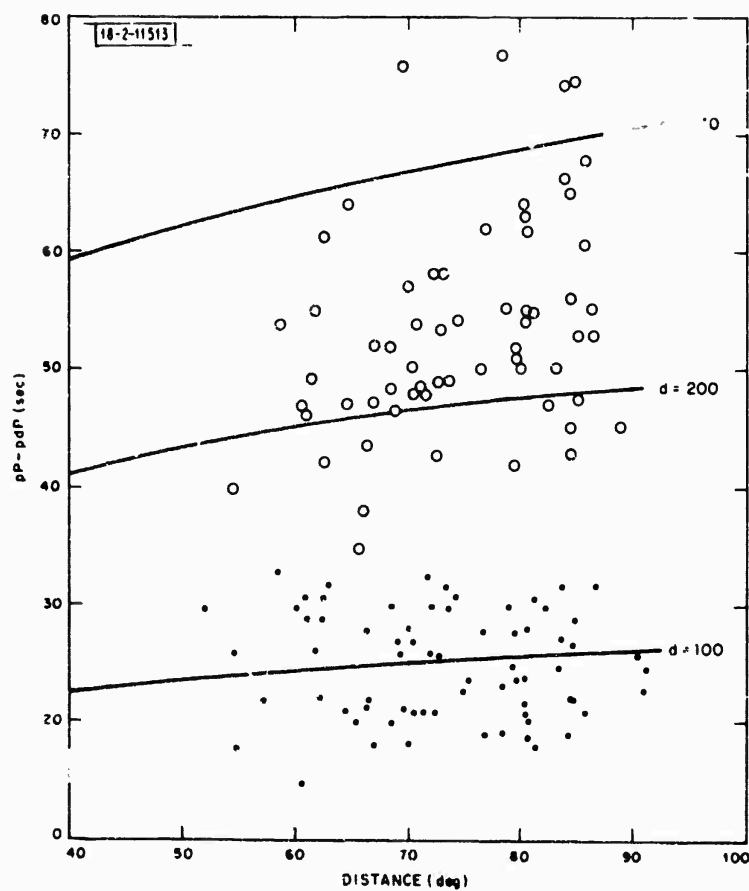


Fig. III-9. Time differences  $pP - pdP$  as picked on WWSSN records from six South American earthquakes.

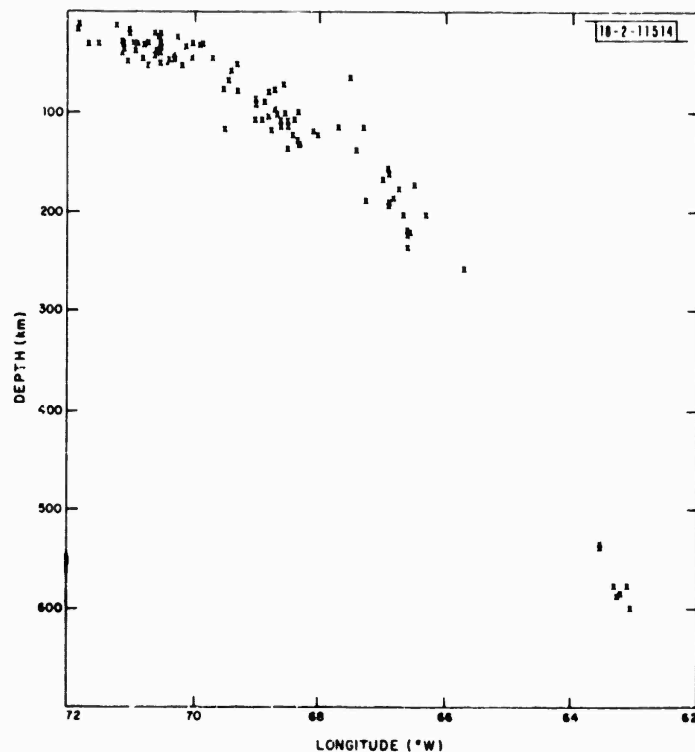
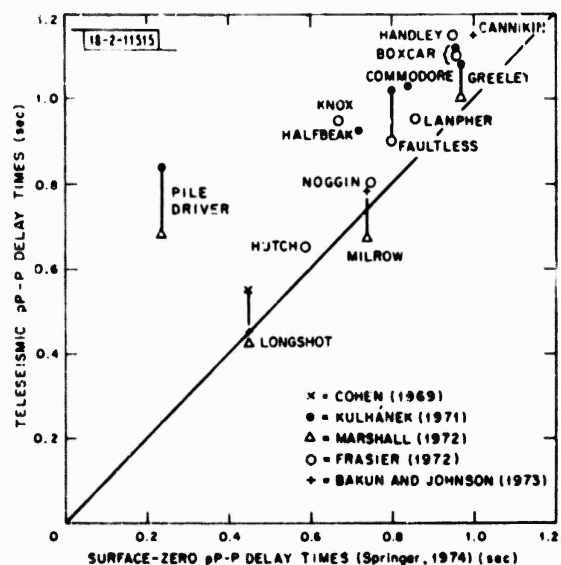


Fig. III-10. Cross section of seismicity ( $m_b > 5.0$ ) between  $20^\circ\text{S}$  and  $30^\circ\text{S}$  from Preliminary Determination of Epicenter lists for years 1967-1970. Hypocenters are projected onto a plane of constant latitude.

Fig. III-11. Teleseismic pP-P delay times vs surface-zero delay times for nuclear explosions given by Springer (1973).<sup>12</sup> Each vertical line connects teleseismic delays obtained from different data for same explosion.



#### IV. GENERAL SEISMOLOGY

##### A. DIGITAL EVENT DETECTOR IN REAL TIME

A single-channel event detector which operates in real time has been programmed for a PDP-7 computer. The purpose of this program is to detect events that an analyst would reasonably pick, given a single channel of data. A direct application would be the automatic detection of events at an unmanned seismological observatory.

A brief description of the detection scheme and some examples with test data are presented here. Basically, the detection scheme compares the spectral energy in a short window with the energy in a long window preceding the short window in time. When the spectral ratio of short-to-long-window energies is greater than an arbitrary value, a detection is declared. This is similar to the detection scheme used by SAAC in that short and long data windows are used.<sup>1,2</sup>

Let the seismic trace be given by the time series  $x_t$ . Define a moving periodogram  $X_t(\omega)$  at time  $t$  given by

$$X_t(\omega) = \sum_{\tau=0}^{m-1} x_{t-\tau} e^{j\omega\tau\Delta t} \quad (\text{IV-1})$$

where

$\Delta t$  = data sampling increment (in seconds)

$\omega$  = frequency (in radians/second).

A simple iteration can be derived from Eq. (IV-1) to calculate the periodogram at time  $t+1$ , namely,

$$X_{t+1}(\omega) = x_{t+1} + X_t(\omega) e^{j\omega\Delta t} - x_{t-m+1} e^{j\omega m\Delta t} \quad (\text{IV-2})$$

From these spectra, we define short- and long-term average powers respectively by

$$\begin{aligned} S_t(\omega) &= \frac{1}{s} \sum_{\tau=0}^s |X_{t-\tau}(\omega)|^2 \\ I_t(\omega) &= \frac{1}{l} \sum_{\tau=m}^{m+l} |X_{t-\tau}(\omega)|^2 \end{aligned} \quad (\text{IV-3})$$

where  $l > s$ .  $S_t(\omega)$  and  $I_t(\omega)$  are averages of energies in overlapping windows of data. The windows used in each average are indicated by solid lines in Fig. IV-1. As an event occurs, the short-term average power increases before the long-term average is affected. This suggests a comparison between short- and long-term averages as a detection criterion. We therefore calculate the average ratio of short- to long-term average for  $n$  specified frequencies

$$R_t = \frac{1}{n} \sum_{i=1}^n \frac{S_t(\omega_i)}{I_t(\omega_i)} \quad (\text{IV-4})$$

A detection is then declared at time  $t$  if  $R_t$  is greater than a threshold parameter  $\Gamma$ . If a detection occurs, the long-term average is fixed at its current level, and the short-term average

is continuously updated. As the event coda diminishes,  $R_L$  will eventually fall below  $T$  and the detector will turn off. If no subsequent detections occur within  $i$  iterations past the last detection, then the long-term average will be immediately updated and Eq. (IV-3) will again be valid. We refer to  $i$  as the update lag.

Experiments were run with this scheme in order to determine reasonable values of window length, averaging lengths and frequencies appropriate for real data from NORSAR. In order to detect events with the variety of periods observed at NORSAR, four frequencies were chosen: 1.0, 1.5, 2.0, and 2.5 Hz. These frequencies are used in the calculation of  $R_L$  in Eq. (IV-4). In the examples presented here, the detection parameters are  $\Delta t = 0.1$  sec,  $m = 30$ ,  $s = 30$ , and  $l = 300$ . Thus, the window length for each periodogram is 3 sec, and the short- and long-term averaging intervals are 3 and 30 sec, respectively. The update lag  $i$  equals 100, corresponding to a lag of 10 sec after the previous detection before the long-term average is updated.

To determine the threshold parameter  $T$ , the detection was run on five single channels of noise at NORSAR from 13:02:00 to 13:09:00 GMT on 23 February 1972. Values of  $T = 5.0, 2.5, 2.0$ , and  $1.5$  were used, for all five channels. The false-alarm rate was calculated as the ratio of time the detector was on to the total time processed. The combined results of all five channels are shown in Fig. IV-2 for the four values of  $T$ . The false-alarm rate for  $T = 2.0$  is only 1.1 percent but the curve is rapidly increasing at that value. To be more conservative, the value  $T = 2.5$  was chosen for the test cases described below. The false-alarm rate for this  $T$  is 0.4 percent, which is quite acceptable.

In order to test this detection scheme, beams of selected events recorded at NORSAR were added to the five noise channels described above. For each event, six scaled beams were added to the noise channels a minute apart. Each beam was reduced by a factor-of-2 in amplitude relative to the beam a minute earlier, so that a series of decreasing beams was put on each noisy channel.

Two examples are shown in Figs. IV-3 and IV-4. In Fig. IV-3, the event is a shallow earthquake from Szechwan Province which occurred on 16 August 1971. In Fig. IV-4, the added event is a high-frequency presumed explosion on 6 June 1971 from Eastern Kazakh. The magnitudes shown in each figure are the result of scaling the event beams down by factors-of-2.

The event detector was run on the five channels shown for each event using the threshold parameter  $T = 2.5$ . The results are shown in Fig. IV-5. We see that for each event the magnitude 4.6 beams were detected on all five channels, and two of the magnitude 4.3 beams of the presumed explosions were detected.

Figure IV-6 shows the output of the event detector for one channel of earthquake data. Beneath the earthquake channel is the detection channel which is either on or off. The third channel shows the instantaneous value of the logarithm of  $R_L$  from Eq. (IV-4). When  $R_L$  rises above the threshold value  $T = 2.5$ , a detection occurs and stays on until  $R_L$  falls below  $T$ .

A moderate-sized population of events is being studied to refine the parameters of this detection scheme.

C. W. Frasier

## B. TRAVEL-TIME ANOMALIES FOR THE GLOBAL STATION NETWORK

Among the products of the deep-focus travel-time study described in Sec. C below and in previous SATS<sup>3</sup> are considerably improved estimates of the travel-time anomalies caused by variations in crust and upper-mantle structure beneath seismic stations. Figures IV-7 and IV-8 show the geographical distribution of these station anomalies in North America and Asia.

One of the main conclusions we have reached is that previous studies using shallow events have been contaminated seriously by errors introduced by complex structures near the sources. This is shown, for example, by a comparison of the standard deviations of the data obtained in the different studies. In the largest previous study (Herrin, et al.<sup>4</sup>), the standard deviation was 1.00 sec, whereas we obtained a value of 0.65 sec. This is in spite of the fact that Herrin, et al allowed their station corrections to vary azimuthally while we did not. Indeed, this fact casts doubt on the validity of the azimuthal station terms derived in previous studies. This doubt is heightened by a comparison of such terms determined independently by Herrin and Taggart,<sup>5</sup> and Lilwall and Douglas.<sup>6</sup> In both studies, the form of the anomaly was taken to be

$$\delta t = A + B \sin(\xi + \Theta) \quad (\text{IV-5})$$

where  $\xi$  is the azimuth from the station to the event, and A, B, and  $\Theta$  are constants. The difference of two terms of this form is another function of the same form, and this fact can be used to examine the differences between the two sets of values. For the 147 stations common to both studies, the root-mean-square magnitudes (B) were 0.64 sec for Herrin and Taggart and 0.62 sec for Lilwall and Douglas. The difference term, however, has an rms value of 0.68 sec! This lack of correlation does not mean that azimuthal anomalies do not exist, but it does mean that at least most of those previously determined are probably not significant. The more nearly error-free deep-focus data can resolve azimuthal station effects is being studied.

B. R. Julian.  
M. Sengupta

### C. P AND S VELOCITY STRUCTURE OF THE LOWER MANTLE

Investigations of the travel times of P-waves from deep-focus earthquakes and lateral heterogeneity of the compressional velocity distribution in the lower mantle have been reported in previous SATS.<sup>3</sup> These studies have now been extended to shear waves from twelve deep-focus and two intermediate-depth shocks, for which arrival time data have been read from 70-mm film chips of WWSSN stations. The earthquakes were relocated using depth information from the phases pP or sP and the revised P travel-time curve and station anomalies. The travel-time curve determined for S-waves is shown in Fig. IV-9 in the form of reduced travel times (averaged in 2° cells) and their standard errors. The solid line represents the predicted times for a model fitted to these data. Note that our shear-wave travel-time data show evidence of sharp bends in the travel-time curve at distances of 48°, 60°, and 71° which agree closely with the locations of similar features found by Johnson<sup>7</sup> from P-wave  $dT/d\Delta$  data. However, since our P-wave travel-time data (which are more accurate) do not show these features, we suspect that they are fortuitous results of errors. We also found that station anomalies for S-waves are strongly correlated with those for P-waves, and are about four times as large, indicating that they are due primarily to variations in rigidity in the upper mantle. Finally, in Figs. IV-10 and IV-11 we show the regional anomalies in P and S travel times for the distance range 80° to 90°. Note the consistency between P and S anomalies as well as the fact that the S anomalies are about 4 to 6 times larger than the P's. Also, a striking feature in this figure is the strong gradient of the velocity anomaly (especially for shear waves) in the neighborhood of the Hawaiian Islands for the depth range of 2400 to 2800 km.

This work is presently being extended to include amplitudes.

M. Sengupta  
B. R. Julian

TABLE IV-1						
PALEOMAGNETIC POLES FOR RUSSIAN, SIBERIAN, AND EAST CHINA PLATES†						
Age	Russian			Siberian		East China
Quaternary	82.4°N	146.1°W		-		-
	9	36.2	9.4			
Tertiary	-			-		75.5°N 38.6°E
						4 630.9 2.8
Cretaceous	62.0°N	179.4°W		75.9°N	165.3°E	63.0°N 145.6°E
	15	27.3	10.3	10	35.7	9.4
						5 35.1 10.9
Jurassic	67.0°N	122.6°E		53.6°N	153.7°E	53.1°N 151.3°E
	4	92.3	7.3	4	11.0	22.0
						4 67.9 8.5
Triassic	54.6°N	153.3°E		41.5°N	141.4°E	-
	5	100.6	6.4	10	17.4	13.6
Permian	45.1°N	167.4°E		18.2°N	143.0°E	16.5°N 153.2°W
	22	115.7	4.6	9	11.9	16.9
						3 19.5 19.6
Carboniferous	42.9°N	170.6°E		31.7°N	145.4°E	-
	33	16.8	12.8	25	14.0	14.2
Devonian	42.4°N	163.9°E		31.0°N	154.3°E	-
	6	80.6	6.8	31	33.5	8.9
Precambrian	-			18.0°N	112.7°E	39.8°N 95.9°E
				7	30.4	10.8
						4 206.8 4.9
† Beneath each pole position are given the number of data points used, an estimate of the Fisher precision parameters, and the radius in degrees of the 95-percent confidence limit of the given pole, respectively.						

#### D. THE PALEOMAGNETISM AND TECTONICS OF ASIA

In an earlier SATS (31 December 1972, p. 59), we presented evidence on the tectonics of Asia from a study of fault plane solutions. In that study, no clear, well-defined tectonic model arose although several, non-unique interpretations in the context of plate tectonics might be suggested by the data. Further study of fault plane solutions and seismicity patterns of central and eastern Asia has tempted us to suggest a tentative plate model for the region. The boundaries of these units - the Russian, Siberian, West China, East China, and Indian Plates - are shown in Fig. IV-12. Since paleomagnetic data should show evidence of these crustal units moving independently in the geologic past, we have made a study of their paleomagnetic pole position using published data.

The individual poles were taken from the following authors: Khranov and Sholpo<sup>8</sup>; McElhinny<sup>9</sup>; Irving<sup>10</sup>; Creer<sup>11</sup>; Wang, et al.<sup>12</sup>; Lee, et al.<sup>13</sup>; and Liu and Feng.<sup>14</sup> Data from rocks that were from regions on or very close to previously postulated plate boundaries were not considered in the analysis. Data for which the cleaning procedures were not known or were inadequate were also not used; therefore, considerable data from the Russian publications had to be rejected. In general, only those samples that were thermally or magnetically cleaned were considered. The cleaning methods used for the Chinese data were unknown, yet the data were used firstly because of the paucity of that data and secondly because the data from widely separated regions showed consistency. If there were at least three poles for a given age on a given plate, the mean pole and precision and confidence statistics were calculated. Poles which varied by more than twice the standard deviation from the mean pole were then deleted and the mean pole was recalculated from the remaining data. Typically, not more than three or four for each plate for each age had to be rejected under this procedure.

The results of the study are shown in Table IV-1 where the mean poles are tabulated for the Russian, Siberian, and East China plates for various ages. Paleomagnetic data for the Indian plate are scant, and we found none for the West China plate. From Table IV-1, relative motion between two plates would be recognized by a difference in mean pole position at the same age. It is clear from Table IV-1 that there has been little or no relative motion between the Russian and Siberian plates since Devonian time. Although the Ural mountains have been suggested as vestiges of a collision between the Russian and Siberian plates, these two units have apparently acted as one since Devonian time. The Permian pole of the East China plate differs from the Siberian and Russian poles; however, the former is based on only three samples. Since Jurassic time, the East China plate seems to have experienced little relative motion with respect to both the Siberian and Russian plates.

Much of the seismicity of central Asia exists within or near the borders of the West China plate. It is under compression on the southwest in the Himalayan fold system and under tension in the northeast in the Baikal Rift Zone. Additionally, from the analysis above, it is bounded on two of its three sides by stable blocks which have not moved relative to each other since at least the Jurassic. If the West China plate does exist as a separate tectonic unit, it would seem to be, at present, rotating clockwise about a pole somewhere near the southern tip of Lake Baikal.

S. Das  
J. R. Filson



## REFERENCES

1. "Seismic Array Design Handbook," Federal Systems Division, International Business Machines (August 1972).
2. J. R. Filson, "On Estimating the Effect of Asian Earthquake Coda on the Explosion Detection Capability of LASA," Technical Note 1973-29, Lincoln Laboratory, M.I.T. (13 July 1973), DDC AD-767878.
3. Seismic Discrimination SATS, Lincoln Laboratory, M.I.T. (30 June 1972), DDC AD-748364, and (31 December 1972), DDC AD-757560.
4. E. Herrin, W. Tucker, J. Taggart, D. W. Gordan and J. L. Lobdell, "Estimation of Surface Focus P Travel Times," Bull. Seismol. Soc. Am. 58, 1273-1291 (1968).
5. E. Herrin and J. Taggart, "Regional Variations in P Travel Times," Bull. Seismol. Soc. Am. 58, 1325-1337 (1968).
6. R. C. Lilwall and A. Douglas, "Estimation of P Wave Travel Times Using Joint Epicenter Method," Geophys. J. R. Astr. Soc. 19, 165-181 (1970).
7. L. R. Johnson, "Array Measurements of P Velocities in the Lower Mantle," Bull. Seismol. Soc. Am. 59, 973-1008 (1969).
8. A. N. Khramov and L. Y. Sholpo, "Synoptic Tables of USSR Paleomagnetic Data." Translated by E. R. Hope, Defense Research Board, Canada, T510R (1970).
9. M. W. McElhinny and E. Irving, "Paleomagnetic Directions and Pole Positions, Parts III - XIII," Geophys. J. R. Astr. Soc. (1961-1973).
10. E. Irving, Paleomagnetism and Its Application to Geological and Geophysical Problems (Wiley, New York, 1964).
11. K. M. Creer, "A Review of Paleomagnetism," Earth Sci. Revs. 6, 369-466 (1970).
12. T. Wang, C. Teng, C. Lee and S. Yeh, "The Original Results of the Position of Paleopoles by Studying the NRM of Chinese Rocks," Acta. Geophysica Sinica 9(2), 125-137 (1960).
13. C. Lee, H. Lee, H. Liu, C. Liu and S. Yeh, "Preliminary Study of the Paleomagnetism of Some Mesozoic and Cenozoic Red-Beds of South China," Acta. Geologica Sinica 43(3), 241-246 (1963).
14. C. Liu and H. Feng, "Alternating Field Demagnetization Study on Lower Sinian Sandstones in Hsiung District Anhwei Province," Acta. Geophysica Sinica 14(3), 173-180 (1965).

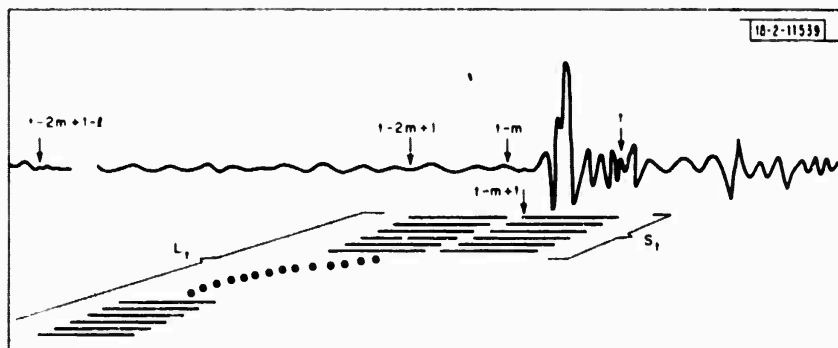


Fig. IV-1. Schematic of seismic data used in detection process. Solid lines indicate overlapping windows from which each periodogram is computed. Windows indicated by  $S_t$  and  $L_t$  are used in computing short- and long-term spectral averages described in text.

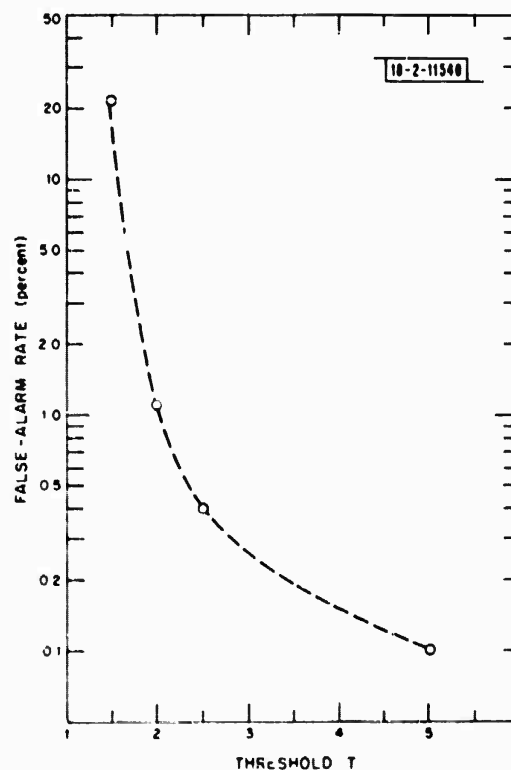


Fig. IV-2. False-alarm rate is percentage of time processed as a function of detection threshold  $T$ .  $T = 2.5$  was chosen to process test data.

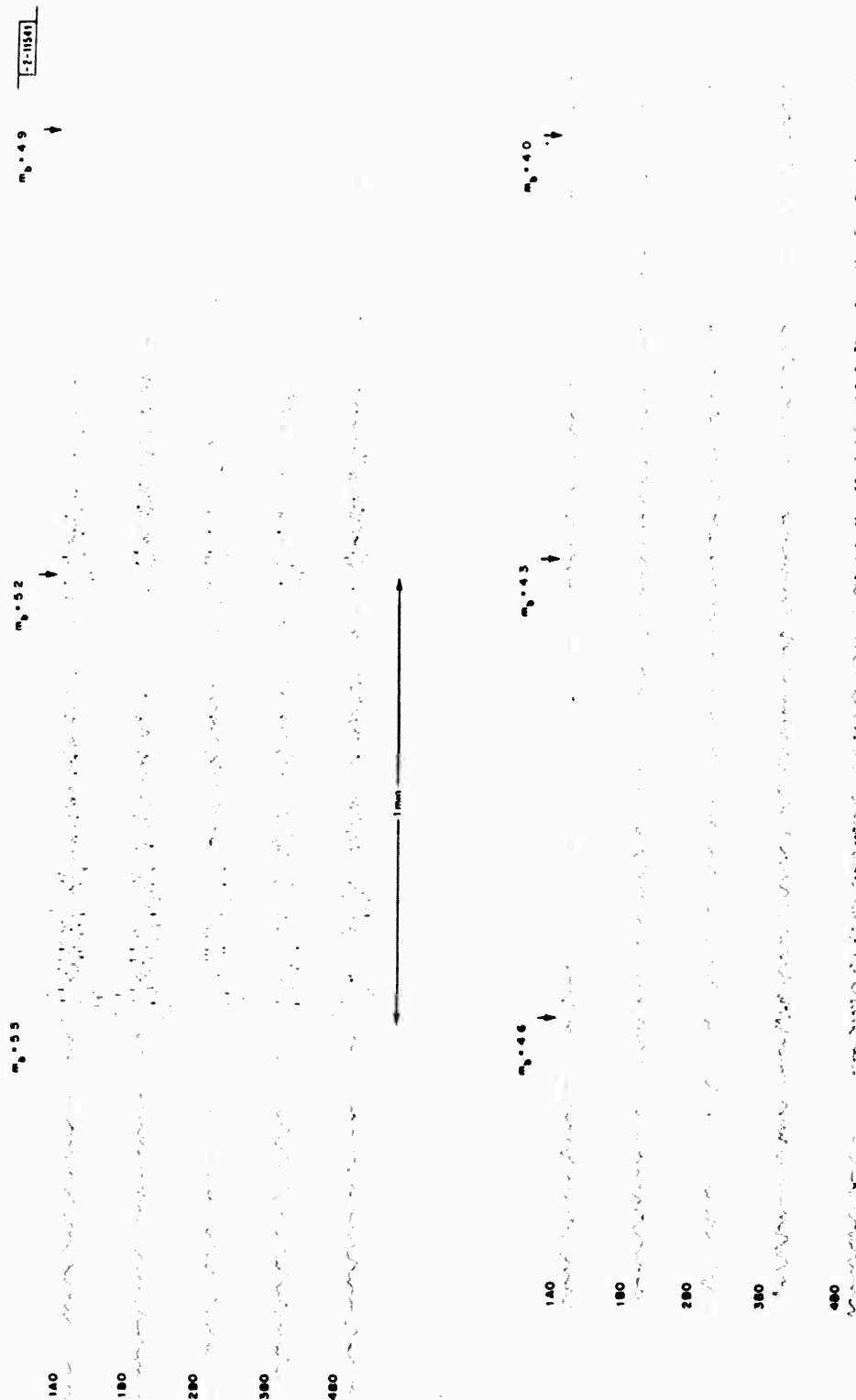


Fig. IV-3. Test array of five noise channels at NORSAR on 23 February 1974, starting at 13:02:00 GMT. Added to each channel is beam of an earthquake from Szechwan Province at 1-minute intervals, each beam amplitude scaled down by a factor-of-2 from previous beam. Effective magnitudes of scaled beams are indicated.

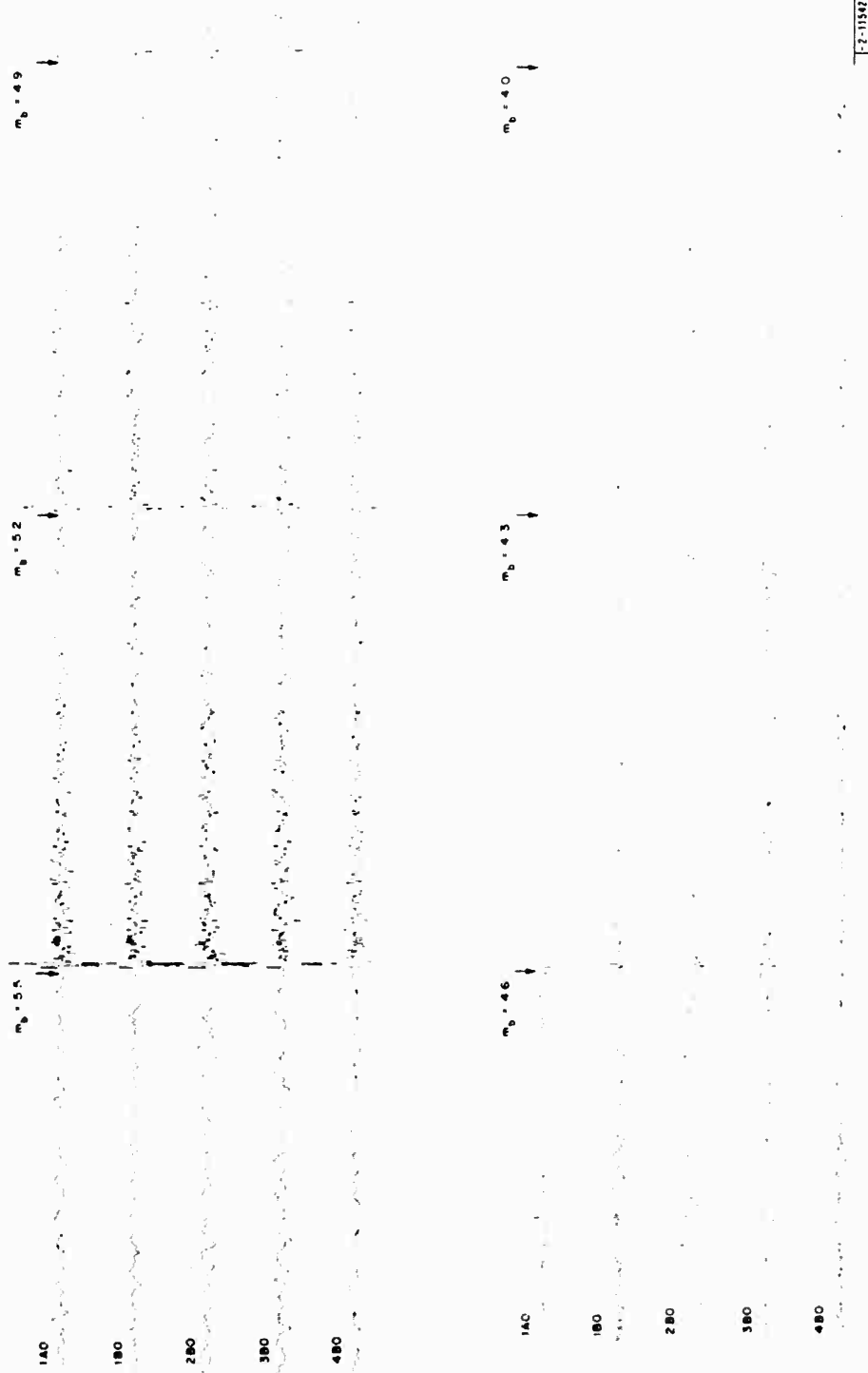


Fig. IV-4. Test array using same noise channels as in Fig. IV-3. Added to each channel is beam of presumed explosion in Eastern Kazakh, scaled down by a factor-of-2 every minute. Effective magnitudes of scaled beams are shown.

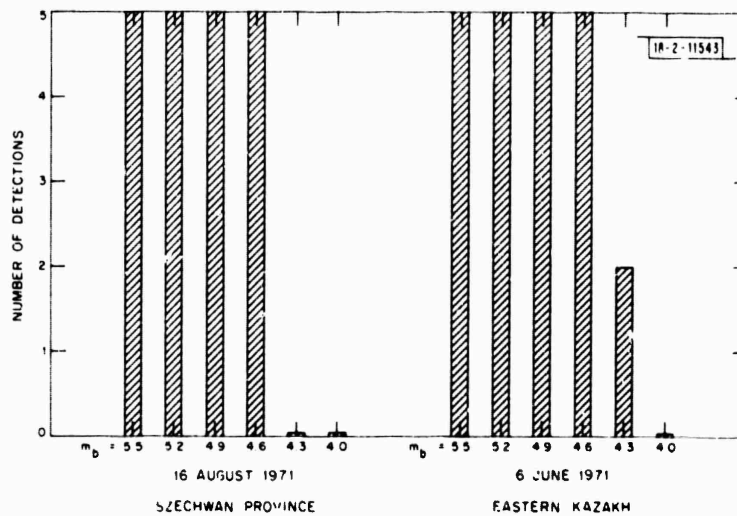


Fig. IV-5. Results of processing test data of Figs. IV-3 and IV-4 with event detector. Five detections for a given  $m_b$  indicate that beam was detected on all channels.



Fig. IV-6. Detection output for one channel of earthquake beams. Top trace is data; bottom trace is logarithmic plot of  $R_t$ ; middle trace is detector which is 0 if  $R_t < 2.5$ , and 1 when  $R_t > T$ .

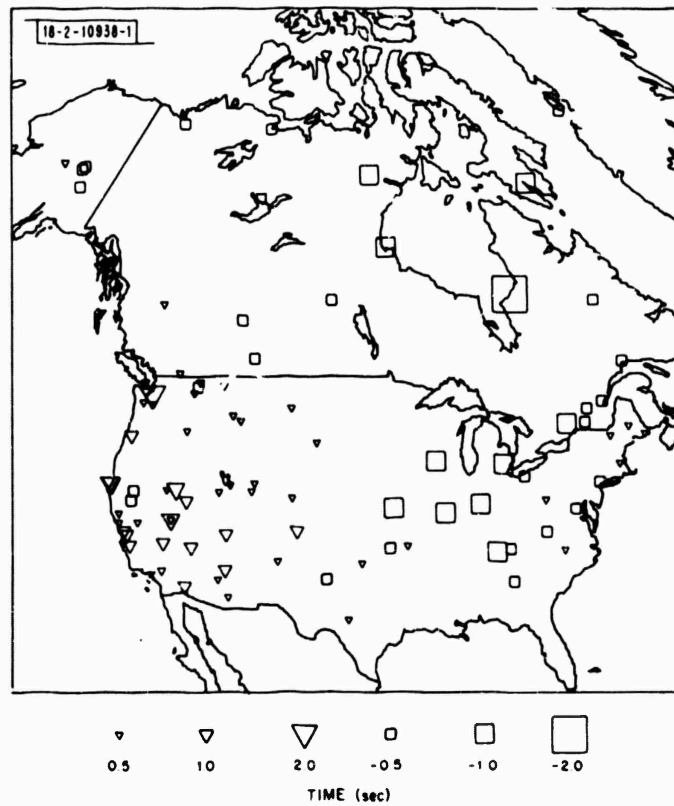


Fig. IV-7. P-wave station anomalies in North America.

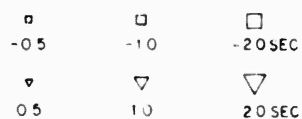
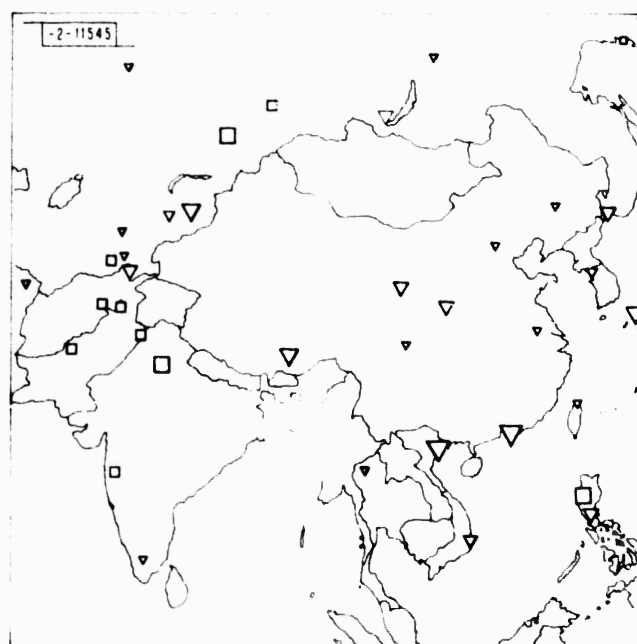


Fig. IV-8. P-wave station anomalies in South Asia.



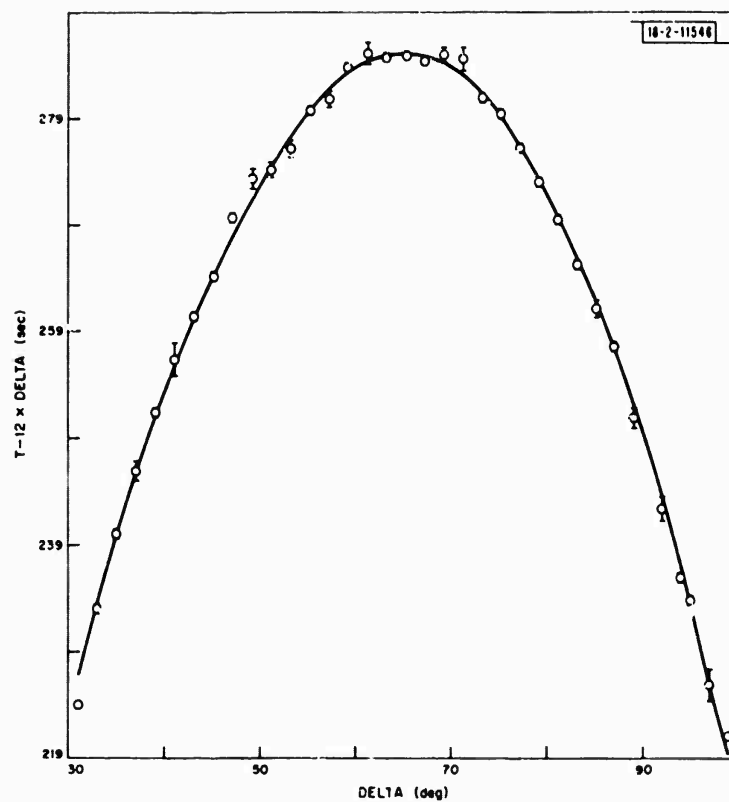


Fig. IV-9. Reduced travel times (averaged in 2' cells) of S-waves and their standard errors. Solid line represents predicted times or model fitted to these data.



Fig. IV-10. Regional anomalies in P-wave travel times for distance range of  $80^{\circ}$  to  $90^{\circ}$ . Symbols are plotted at midpoint of great circle path. Crosses represent late arrivals, and squares indicate early arrivals. Straight lines are in direction of source to station azimuth, their length being proportional to travel-time anomalies. Smallest length in this figure represents an absolute value of 0.5 sec, and largest is an absolute value of 3 sec.

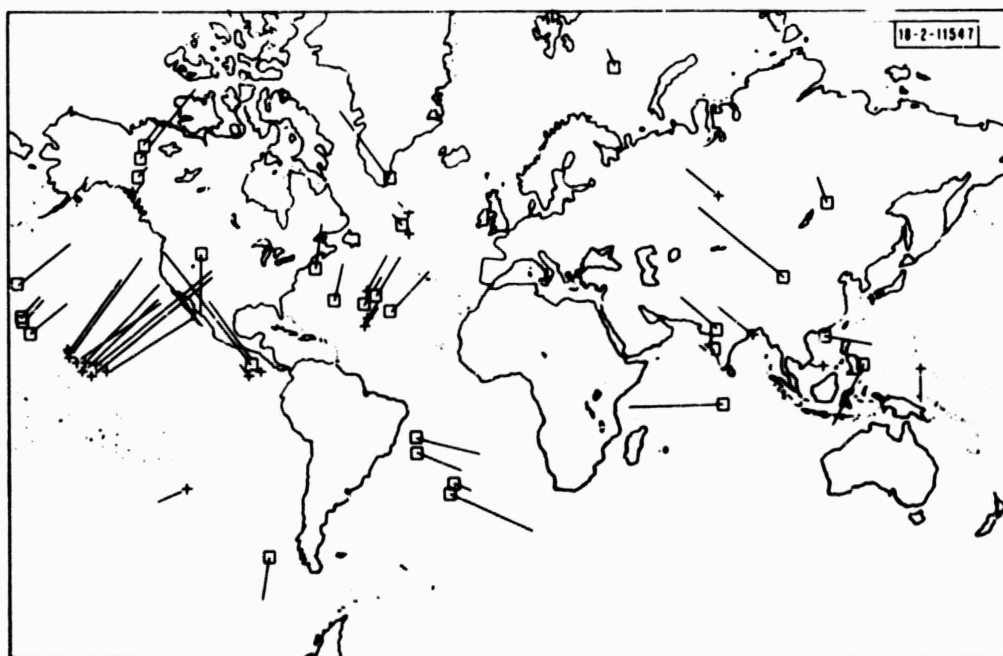


Fig. IV-11. Regional anomalies for S-waves. Symbols same as in Fig. IV-10.

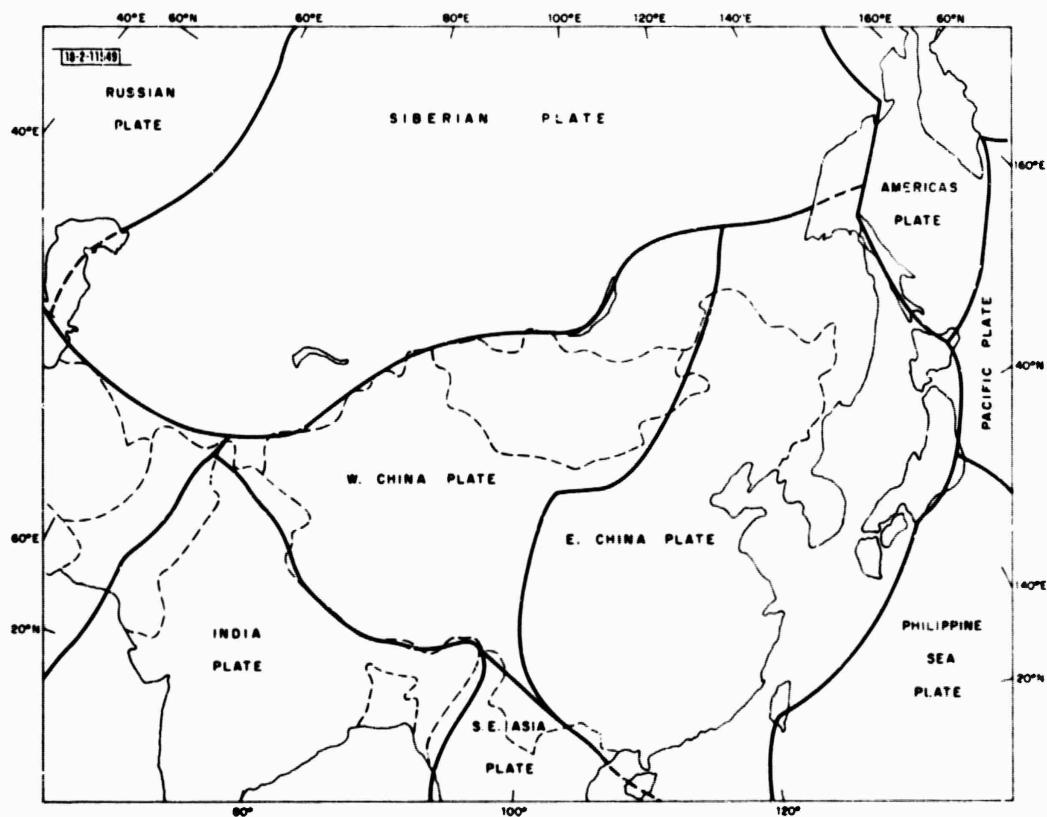


Fig. IV-12. Hypothetical plate model of Asia.

## V. COMPUTER FACILITIES

### A. ARPA NETWORK COMPUTER FACILITY DEVELOPMENT

The ARPA Nuclear Monitoring Research Office has initiated a research and development program to make use of satellite communications, the ARPA Network, computer netting, and mass store technology to achieve their seismic detection and discrimination research objectives. Lincoln Laboratory has undertaken to develop and implement special hardware and software facilities which will allow us to participate fully in the program and to exploit the full potential of computer netting and remote data bases for seismic research.

A survey of our needs and technological alternatives indicated that the first step should include:

- (1) A small host computer connected to the ARPA Network and having:
  - (a) A collection of basic peripherals: card reader, printer, plotter, magnetic tape drive, secondary storage, etc.
  - (b) A number of basic terminals such as teletypes.
  - (c) A number of "intelligent" terminals, suitable for interactive graphics and typically containing a programmable minicomputer.
  - (d) A software system providing:

Standard terminal access to network resources.

An extended file transfer capability (among and between the local peripherals, including the basic and "intelligent" terminals, and remote machines) for high-speed transfer of data and programs.

Remote Job Entry capability.

Full support for "intelligent" terminals.

- (2) The re-establishment of general Network capability on the main Lincoln Laboratory computer when the new ILM 370/168 is installed in January 1974.
- (3) The creation of special data access and manipulation software to enable the seismic researcher and his program to handle data anywhere in the system including the Datacomputer.

A substantial beginning has been made toward these goals. The host computer, a Digital Equipment Corporation PDP-11/40, has been installed with a card reader, an electrostatic printer/plotter, one magnetic-tape drive, a 1.2-megaword disk, and two terminals (an LA30 and a GT-40). The LA30 is a representative basic terminal, capable of operating at 30 characters per second. The GT-40 is a prototype "intelligent" terminal. It contains a PDP-11/05 processor and, in our configuration, includes a minidisk, CRT display with light-pen and analog-to-digital conversion capability.

A wide-band phone line has been installed between the host machine and the CCA Terminal-IMP. The Terminal-IMP-to-phone-line hardware is installed; telephone-line-to-host interface hardware is on order.

There is a contract with the University of Illinois' Advanced Computation Center for a customized version of their ANTS Mark II system. This will provide all the software facilities cited

in (d) above. Lincoln Laboratory has been working closely with the University of Illinois to insure adequate support for the "intelligent" terminals and a sufficiently powerful and flexible file system.

The Computer Systems Group at Lincoln Laboratory has undertaken the task of supplying Network software for the main Lincoln machine (the 370/168). Initially, they will support the Net at the NCP and Telnet levels. This will give a network user with a basic terminal the same power and facilities available to the regular VM (time-sharing) user.

Our task will comprise designing and implementing the special software required: the Data-computer access mechanisms; the file transmission over the Net from the 370; etc. To make this task easier, extensive explorations of SUE – a higher level, systems implementation language suitable for the 370 and for the DEC machines (the 11/40 and the GT-40) – are under way. In addition, bootstrapping systems have been installed on the two DEC machines: DOS (Disk Operating System) on the 11/40, and CAPS (CAssette Programming System) on the GT-40.

Y. Peduel  
R. T. Lacoss  
J. R. Walton

## B. PDP-7 COMPUTER SYSTEM

The two PDP-7 systems continue to be heavily used by Lincoln Laboratory staff. An appreciable portion of the remaining time is used by visiting seismologists, by graduate students, and for ISM production runs.

The system has become fairly stable, and it was decided that a complete revision of system documentation was in order. The new Software Handbook will consist of twelve chapters in two volumes. Of these, nine chapters have been written and published:

- I. System Introduction
- II. Basic System Utilities
- III. Editor
- V. Assembler
- VIII. Data Analysis Console
- IX. Data Analysis and Display System
- X. Program Library
- XI. Subroutine Library
- XII. Preliminary Index

Yet to be published are:

- IV. Fortran
- VI. I/O Devices
- VII. Data Formats

L. J. Turek  
M. F. O'Brien